UCONN LIBRARY

University of Connecticut
OpenCommons@UConn

Doctoral Dissertations

University of Connecticut Graduate School

9-8-2016

Mesoporous Manganese Oxide Materials for Aerobic Oxidation Reactions

Sourav Biswas
sourav108chem@gmail.com

Follow this and additional works at: https://opencommons.uconn.edu/dissertations

Recommended Citation
Biswas, Sourav, "Mesoporous Manganese Oxide Materials for Aerobic Oxidation Reactions" (2016). *Doctoral Dissertations*. 1202.
https://opencommons.uconn.edu/dissertations/1202

Mesoporous Manganese Oxide Materials for Aerobic Oxidation Reactions

Sourav Biswas, Ph.D.

University of Connecticut, 2016

The thesis presented here is focused on fabricating thermally stable and tunable mesoporous manganese oxide materials for catalytic aerobic oxidation reactions. From the viewpoint of green chemistry, the design of novel methodologies for oxidation, preferably under aerobic atmospheric condition, without any additives is highly desirable. Being motivated by advances in catalytic materials as fundamental pillars of 'green chemistry', my research is devoted to designing of useful materials in oxidative catalysis that may serve the purpose of sustainable energy sources in harmony with the environment and nature. The five chapters provided here will discuss the importance of catalytic oxidation reactions, synthesis, and characterization of the mesoporous manganese oxide materials and their applications in a series of simple to complex oxidation reactions. We demonstrate the activity enhancement of mesoporous manganese oxide materials by introducing alkali metal ions in a simple alcohol oxidation reaction. The major achievement of this work is inventing a cesium ion promoted mesoporous manganese oxide, which was found to be active in a multitude of aerobic oxidation reactions. In terms of catalytic oxidation reactions, oxidation of alcohol to aldehydes, amines to imines, a versatile one –pot tandem oxidation processes and oxidative coupling of alkynes have been discussed. Moreover, mechanistic aspects of catalytic oxidation are studied in details, especially the role of the surface oxygen species,

oxygen vacancies and related oxygen transportation of the metal oxides. The catalytic oxidation protocols discussed here have several advantages over the existing systems in addressing the goals of green chemistry. First, the heterogeneous nature of the catalyst provides ease of separation of product. Next, excellent reusability of the catalyst (as high as 8 cycles) and formation of water as the only by-product (in most of the cases) reduces toxic waste production. Finally, absence of additives and use of air as the terminal oxidant exemplify the greener, more efficient and less expensive nature of these processes.

Mesoporous Manganese Oxide Materials for Aerobic Oxidation Reactions

Sourav Biswas

B.Sc., Jadavpur University, Kolkata, India. 2008

M.Sc., Indian Institute of Technology, Madras, India. 2011

A Dissertation

Submitted in Partial Fulfillment of the

Requirement for the Degree of

Doctor of Philosophy

at the

University of Connecticut

2016

Copyright by

Sourav Biswas, 2016. All rights reserved.

2016

APPROVAL PAGE

Doctor of Philosophy Dissertation

Mesoporous Manganese Oxide Materials for Aerobic Oxidation Reactions

Presented by
Sourav Biswas

Major Advisor _____
Steven L. Suib

Associate Advisor _____
Amy R. Howell

Associate Advisor _____
Alfredo Angeles-Boza

Associate Advisor _____
Ramamurthy Ramprasad

Associate Advisor _____
Fatma Selampinar

University of Connecticut
2016

Dedicated to my parents, my brother and my beloved wife

Acknowledgements

I would like to express my sincere gratitude to my major advisor, Dr. Steven L. Suib, for his guidance and constant support throughout my graduate career. The opportunity to work on a wide range of projects and interaction with diverse group of people in his research group allowed me not only to broaden my knowledge of chemistry but also made me a well-rounded person. The most important things I learned from him are the dedication and enthusiasm to work, which will stay with me in the rest of my life.

I would like to thank my associate advisors Dr. Amy R. Howell, Dr. Alfredo Angeles-Boza, Dr. Ramamurthy Ramprasad and Dr. Fatma Selampinar for their support and guidance.

I would also like to express my thanks and gratitude to Dr. Partha Nandi, Mrs. Bonnie Segundo Suib, Dr. Angelo R. Rossi, and Dr. Frank Galasso for their guidance, support and encouragement. I am very thankful to my colleagues and group members Dr. Chung-Hao Kuo, Sheng-Yu Chen, Curtis Guild, Biswanath Dutta, David Kriz, Ehsan Moharreri, Islam Mosa, Anton Gudz, Dr. Abdelhamid El-Sawy, Dr. Lakshitha Pahlagedara, MD Shakil, Saiful Seraji, Wenqiao Song, Junkai He, Wei Zhong, Niluka Wasalathanthri, Chandima Weerakkody, Carlos Mendoza, Hannah Trip, David Giori, Tehereh Jafari, Harshul Khanna and especially Dr. Altug S. Poyraz.

I am grateful to the Department of Chemistry and Institute of Materials Science, University of Connecticut and their employees for their support during my graduate studies. Special thanks to Dr. You-Jun Fu, Dr. Heng Zhang, Dr. Bill Willis, Dr. William A. Hines, Osker Dabahsu, Charlene Fuller, and Ashley Orcutt for their assistance.

I acknowledge the financial support of the United States Department of Energy, Office of Basic Energy Sciences, and the Department of Chemistry, the Institute of Materials Science, the

Center for Environmental Sciences and Engineering, and the Graduate School of the University of Connecticut.

I also want to thank my mom, dad and my brother for their sacrifice and continuous support. Without the help of them, I cannot have such a life here. Lastly I would like to express my heartiest gratitude to my wife Mrs. Kankana Mullick. She has played a pivotal role in my life and without her support and unconditional love I would not be the person I am today.

Table of Contents

Chapter 1. Introduction

1.1 Overview of Catalytic Oxidation 1

1.2 Heterogeneous Catalysts 2

1.3 Mesoporous Materials.....2

1.4 UCT Materials.....4

1.5 Manganese Oxides 6

1.6 References 8

Chapter 2. Ion Induced Promotion of Activity Enhancement of Mesoporous Manganese Oxides for Aerobic Oxidation Reactions

2.1 Abstract 11

2.2 Background and Significance 11

2.3 Experimental Section 13

2.3.1 Synthesis of UCT-1 13

2.3.2 Synthesis of UCT-18 14

2.3.3 Catalyst Characterization 14

2.3.4 Catalytic Activity Measurement 16

2.4 Structural Characterization 17

2.5 Catalytic Reactions 25

2.5.1 Catalyst Screening 25

2.5.2 Oxidation of Alcohols 27

2.5.3 The oxidation of 1,3,5-trimethylbenzene (C-H activation).....29

2.6 Discussions 30

2.7 Conclusions 35

2.8 References 37

Chapter 3. Efficient Aerobic Oxidation of Amines to Imines by Cesium Promoted Mesoporous Manganese Oxide

3.1 Abstract 40
3.2 Introduction 40
3.3 Experimental Section 42
3.3.1 Synthesis of Mesoporous Cs/MnO_x 42
3.3.2 Catalyst Characterization 43
3.3.3 Catalytic Activity Measurements 44
3.4 Structural Characterization of Meso Cs/MnO_x 46
3.5 Catalytic Reactions 50
3.5.1 Optimization of Reaction Condition 50
3.5.2 Comparison with Different Catalysts 51
3.5.3 Reusability and Heterogeneity 53
3.5.4 Oxidation of Amines to Imines 54
3.5.5 Oxidative Cross Coupling of Amines.....57
3.5.6 Kinetic and Mechanistic Study.....59
3.6 Discussions 61
3.7 Conclusions 66
3.8 References 66

Chapter 4. Facile Access to Versatile Functional Groups from Alcohol by Single Multifunctional Reusable Catalyst

4.1 Abstract 69
4.2 Background and Significance.....69
4.3 Experimental Section 72
4.3.1 Synthesis of Mesoporous Cs/MnO_x 72
4.3.2 Catalytic Activity Measurements.....73
4.3.2.1 Preparation of imine 73
4.3.2.2 Preparation of benzimidazole 73
4.3.2.3 Preparation of α,β unsaturated ketone.....74
4.3.2.4 Preparation of amide 75

4.3.2.5 Preparation of ester.....75
4.3.2.6 Preparation of lactone.....75
4.3.3 Analysis of Reaction Products 76
4.4 Time-of-Flight Secondary Ion Mass Spectrometry Measurement 76
4.5 Catalytic Reactions 77
4.5.1 One-pot Imine Formation.....77
4.5.2 Benzimidazole Formation.....84
4.5.3 Oxidative Amidation.....85
4.5.4 C-C Bond Formation 87
4.5.5 Oxidative Multiple Esterification 87
4.6 Discussions 91
4.7 Conclusions 93
4.8 References 94

Chapter 5. Mesoporous Copper/Manganese Oxide-Catalyzed Coupling of Alkynes: Evidence for Synergistic Cooperative Catalysis

5.1 Abstract 96
5.2 Background and Significance…….....97
5.3 Experimental Section 100
5.3.1 Synthesis of Mesoporous Cu/MnO_x 100
5.3.2 Catalyst Characterization 100
5.3.3 Homo-coupling of Terminal Alkynes 102
5.3.4 Hetero-coupling of Terminal Alkynes 102
5.3.5 Analysis of Reaction Products of Alkyne Coupling 103
5.4 Structural Characterization of meso Cu/MnO_x 103
5.5 Catalytic Reactions 109
5.5.1 Optimization of Reaction Condition.....109
5.5.2 Oxidative Homo-coupling of Terminal Alkynes.....112
5.5.2.1 Substrate Scope.....112
5.5.2.2 Characterization of Diynes 115
5.5.3 Oxidative Cross Coupling of Alkynes.....117

5.5.4 Reusability and Heterogeneity.....118
5.5.5 Kinetic Studies 119
5.5.6 Role of Manganese Oxide.....121
5.5.7 Role of Lattice Oxygen.....122
5.6 Theoretical Results.....124
5.6.1 Geometries and Transition Metal Coordination 124
5.6.2 Basic Sets and Density Functional 125
5.6.3 Optimized Geometries of Transient Intermediates 125
5.6.4 Cu sites on the meso Cu/MnO_x surface.....126
5.6.5 Mn sites on the meso Cu/MnO_x surface.....127
5.6.6 Molecular Analogues of Reactive Surface Species.....128
5.7 Discussions 130
5.8 Conclusions 136
5.9 References 138

Chapter 6. Future Perspectives…….....141

Appendix ……..143

LIST OF FIGURES

Figure 1.1 Formation mechanism of mesoporous manganese oxide by UCT synthesis procedure. Metal loaded inverse micelles are packed and inorganic components condensed and oxidized. Surfactants are removed by solvent extraction and adsorbed species are eliminated by heat treatment……..5

Figure 2.1 (A) Low angle (0.5° – 8°) PXRD patterns , (B) Wide angle (5° – 75°) PXRD patterns, (C) N_2 sorption isotherms, and (D) BJH desorption pore size distributions of cation promoted mesoporous manganese oxides (UCT-18-X, X= Mg^{2+}, Ca^{2+}, K^+, Na^+, and Cs^+)……19

Figure 2.2 FE-SEM images of (A) UCT-18-Cs, (B) UCT-18-Na, (C) UCT-18-K, (D) UCT-18-Ca, (E) UCT-18-Mg (F) UCT-1 materials and HR-TEM images of UCT-18-Cs material (G, H) at lower magnifications (I) at higher magnification. The measured lattice distances 0.49 and 0.27 nm are indexed to bixbyite Mn_2O_3 (200) and (222) planes……..20

Figure 2.3 CO_2 adsorption isotherms of UCT-1 and UCT-18-X, X= Mg^{2+}, Ca^{2+}, K^+, Na^+, and Cs^+ at 298K……...21

Figure 2.4 Temperature resolved *in situ* PXRD (TR-PXRD) of (A) UCT-18-Cs, and (B) UCT-1. The materials were ramped at 5°C min^{-1} up to 550°C. The diffraction patterns were obtained in the range of 5-75° 2θ at a scanning rate of 2° min^{-1}.....22

Figure 2.5 (a) H_2-TPR and (b) O_2-TPO and (c) O_2-TPD profile of UCT-18-Cs and UCT-1. The measurements were conducted from room temperature to 700°C (10°C/min) under a stream of 10 % H_2/Ar for H_2-TPR, 10 % O_2/Ar for O_2-TPO and pure Ar for O_2-TPD with a flow rate of 50 sccm.....23

Figure 2.6 XPS analysis: (a) deconvoluted O1s spectra of UCT-18-Cs and UCT-1 (inset) and (b) Mn 2p spectra of UCT-1 and UCT-18-Cs materials. The C 1s photoelectron line at 284.6 eV was used as a reference for correction of surface charging……24

Figure 2.7 Oxidation of benzyl alcohol by UCT-18-K with different Mn/K (mol/mol) nominal ratio. Reaction conditions: benzyl alcohol (1.0 mmol), catalyst (50 mg), toluene (15 mL), 85°C, air flow, 2 h……26

Figure 2.8 The oxidation of alcohols by UCT-1 and UCT-18. Reaction Conditions: alcohols (1.0 mmol), toluene (15 mL), catalyst (50 mg), under air flow, 85°C/ 110°C, 2 h/4 h……..27

Figure 3.1 Structural characterization of meso Cs/MnO_x. PXRD patterns (A) Low angle (0.5° - 8°), (B) Wide angle (5°-75°), (C) N_2 sorption isotherm and (D) BJH desorption pore size distribution.....47

Figure 3.2 SEM images of meso Cs/MnO_x at (A) low and (B) higher magnifications……47

Figure 3.3 TEM images of meso Cs/MnO_x at (A) low and (B) higher magnification. The measured lattice distances of 0.27 nm can be indexed to bixbyite Mn_2O_3 (222) planes……48

Figure 3.4 XPS of meso Cs/MnO_x. (A) Deconvoluted O1S spectra. Three different oxygen species were identified: Structural or lattice oxygen (O_s), surface adsorbed oxygen (O_{ads}) and adsorbed water or hydroxyl group (O_{mw}) and (B) Mn 2p spectra. The binding energy values fall in the binding energy of the Mn^{3+} oxidation state……49

Figure 3.5 O_2-TPD of meso Cs/MnO_x. The peak around 570°C can be ascribed as the lattice or structural oxygen desorption from the material……..49

Figure 3.6 (A) Reusability test of the catalyst. Reaction condition: 4-methoxybenzylamine (0.5 mmol), catalyst (15 mg), solvent (5 mL), 110°C, air balloon, 4 h. Turnover number (TON) = [reacted mol amine]/[total mol catalyst]. (B) PXRD of meso Cs/MnOx before and after fourth reuse. The diffraction patterns without noticeable change were observed after fourth reuse……54

Figure 3.7 Time dependent studies of 4-methoxybenzylamine by meso Cs/MnOx : (A) at 80°C and (B) at 110°C. Reaction condition: 4-methoxybenzylamine (0.5 mmol), catalyst (25 mg), solvent (5 mL), O_2 balloon, 3/8 h. The formation of benzaldehyde was clearly observed in both cases……...59

Figure 3.8 (A) Arrhenius plot for the oxidation of amine by meso Cs/MnO_x and (B) Kinetic plot of oxidation of benzylamine and benzylamine-α,α-d_2. The ratio of K_H/K_D = 2.02; which signified the oxidative dehydrogenation of benzylamine was the rate determining step. Reaction condition: amine (0.5 mmol), catalyst (25 mg), solvent (5 mL), 110°C, air balloon, 3 h. A_0: original concentration of substrate. A_t: concentration of substrate at time t. k: rate constant……..60

Figure 3.9 Hammett plot of competitive oxidation of para substituted benzylamine at 15 min of reaction time. Reaction condition: amine (0.5 mmol), catalyst (25 mg), solvent (5 mL), 110°C, air balloon, 15 min. A linear relationship between ln(k_x/k_H) and Brown–Okamoto constant (σ_p^+) for para substituted benzylamines with slope (ρ) of 1.264 were obtained, which indicated the formation of negatively charged intermediate……61

Figure 4.1 TOF-SIMS images of meso Cs/MnO_x in two different regions (scale bar is 10 µm)…76

Figure 4.2 TOF-SIMS depth profiles of meso Cs/MnO_x in two different regions……77

Figure 4.3 Powder X-ray diffraction of meso Cs/MnOx before and after third reuse……..82

Figure 4.4 Conversion of benzyl alcohol over time course with and without n-dodecylamine. Reaction condition: benzyl alcohol (1 mmol), n-dodecylamine (2.0 mmol), meso Cs/MnO_x (50 mg), toluene (5 mL), 110°C, air balloon……83

Figure 4.5. CO_2-TPD study A sharp peak of CO_2 (at 500°C) was observed from the material after the reaction, which can be ascribes as the adsorbed CO_2 coming from the reaction due to decarboxylation. Whereas, the material only showed a small peak due to adsorption of the substrate and no CO_2 was evolved from the bare material itself……..89

Figure 5.1 Structural characterization of meso Cu/MnO_x with different Mn/Cu molar ratio. PXRD patterns (A) Low angle (0.5° -8°), (B) Wide angle (5°-75°), (C) Nitrogen sorption isotherms and (D) BJH adsorption pore size distributions……..…105

Figure 5.2 The FE-SEM images of meso Cu/MnO_x with different Mn/Cu molar ratio (a) 100/1, (b) 50/1 and (c) 10/1…….106

Figure 5.3 (a, b and c) The TEM images and TEM-EDX elemental maps (d) Mn-L, (e) Cu-L and (f) O-L of meso Cu/MnO_x with Mn/Cu molar ratio 10/1……107

Figure 5.4 XPS of meso Cu/MnO_x (10% Cu): (a) Cu 2p (* indicates the shake up satellite peaks), (b) Mn 2p, (c) deconvoluted O 1s and (d) comparison of the O 1s transitions of meso Cu/MnO_x and meso MnO_x. …….108

Figure 5.5 Effect of copper loading in catalytic activity. Reaction condition: phenylacetylene (1.0 mmol), meso Cu/MnO_x (50 mg), toluene (5 mL), 105°C, 3 h, under air balloon. ……109

Figure 5.6 (a) The reusability experiment. Reaction Conditions: phenylacetylene (0.5 mmol), catalyst (6 mol% Cu with respect to phenylacetylene), toluene (5 mL), 105°C, 45 min, air balloon. (b) PXRD before and after 8^{th} reuse. ……..119

Figure 5.7 Kinetic experiment of homo-coupling of phenylacetylene by meso Cu/MnO_x. The reaction exhibited first order kinetics with respect to phenylacetylene concentration. Reaction condition: alkyne (0.5 mmol), meso Cu/MnO_x (6 mol % with respect to phenylacetylene), toluene (5 mL), 105°C, under air balloon. ……...120

Figure 5.8 Kinetic plot of oxidation of phenylacetylene-D and phenylacetylene. The ratio of K_H/K_D = 0.9; which signified the abstraction of alkyne proton was not the rate determining step. Reaction condition: phenylacetylene (0.5 mmol), meso Cu/MnO_x (6 mol % with respect to phenylacetylene), toluene (5 mL), 105°C, air balloon. ……120

Figure 5.9 Comparison of Cu 2p XPS of meso Cu/MnO_x and meso Cu/TiO_2 after the reaction at different atmosphere (air and nitrogen). ……..122

Figure 5.10 Effect of calcination temperature on catalytic activity. Reaction Conditions: Phenylacetylene (0.5 mmol), meso Cu/MnO_x (6 mol%), toluene (5 mL), 105°C, 30 min, air balloon.…….123

Figure 5.11 O_2-TPD of meso Cu/MnO_x at different calcination temperatures. ……124

Figure 5.12 (a) π–$[L_4Cu(II)(H\text{-}C \equiv C\text{-}H)]^{2+}$, and (b) π–$[L_4Cu(II)(C \equiv C\text{-}H)]^{+}$complexes. The stability of the complex (a) relative to the separate components is 6.2 kcal mol^{-1}. The acetylide anion (–C ≡ C-H) in (b) was unstable with respect to a DFT calculation using a 6-31g* basis set,

and prevented the determination of relative stability, but its value is larger than (3a). L stands for H_2O. …….127

Figure 5.13 (a) $[L_nMn(III)(O_2)]^+$, and (b) $[L_nMn(III)(O_2H)]^{2+}$, complexes. The stability of the complex (a) relative to the separate components is 59.4 kcal mol^{-1}. The hydroperoxyl anion (O_2H^-) was unstable with respect to a DFT calculation using a 6-31g* basis set, and prevented the determination of relative stability, but its value is larger than (4a). L stands for H_2O. ……..128

Figure 5.14 Model systems [(a) Mn atom, squeezed between two active Cu atoms, (b) Cu sites are adjacent to each other and (c) O_2 as the bridging ligand between Cu atoms] on the Cu/MnO_x surface capable of oxidative coupling of alkynes. ……129

Figure 5.15 Relative energies for the coupling of two acetylide moieties along the optimization pathway for structure **Figure 5.14b**. Only the acetylide fragments are optimized, with H_2O ligands and metal atoms remaining fixed to simulate the infrastructure of a Cu/MnO_x surface. …….133

LIST OF TABLES

Table 2.1 Structural parameters of UCT-1 and UCT-18……...19

Table 2.2 XPS results of UCT-1 and UCT-18-Cs materials. ……...25

Table 2.3 Aerobic selective oxidation of different alcohols by UCT-1 and UCT-18-Cs…….28

Table 2.4 Aerobic oxidation and cross dehydrogenative coupling of 1,3,5-timethylbenzene…..29

Table 3.1 Optimization of oxidative coupling of 4-methoxy benzyl amine……..51

Table 3.2. The catalytic results using different catalysts……...52

Table 3.3 Oxidation of 1,2,3,4-tetrahydroisoquinoline by meso Cs/MnOx with different Cs loading. ….…….53

Table 3.4 Aerobic oxidation of amines to imines by meso Cs/MnO_x ……..55

Table 3.5 Aerobic oxidative cross coupling of benzylamine with different amines ……58

Table 4.1 Tandem imine formation from alcohol by meso Cs/MnO_x ……79

Table 4.2. Reusability test of the catalyst ……..81

Table 4.3. Percent Conversion of condensation of benzaldehyde and 4-nitroaniline ……...83

Table 4.4 Various tandem reactions from alcohols by meso Cs/MnO_x ……86

Table 4.5. Solvent free aerobic oxidation of 1-octanol by different catalysts ……..88

Table 5.1 Structural parameters of meso Cu/MnO_x ……105

Table 5.2 Comparion of XPS of Mn 2p and O 1s signal ……109

Table 5.3 Optimization of reaction conditions ……111

Table 5.4 Oxidative homo-coupling of phenyl acetylene by different catalysts ……112

Table 5.5 Aerobic oxidative homo-coupling of terminal alkynes ……..114

Table 5.6 Aerobic oxidative cross coupling of terminal alkynes ……118

Table 5.7 XPS data of meso Cu/MnO_x and Cu/TiO_2 before and after reaction ……122

LIST OF SCHEMES

Scheme 2.1 Proposed alcohol oxidation mechanism over UCT-18-Cs 33

Scheme 3.1 Proposed reaction pathways of Mn mediated RCH=NH formation from amine. The forming of negatively charged intermediate due to abstraction of proton by oxidative dehydrogenation is the rate determining step (RDS) ……64

Scheme 3.2 Suggested overall mechanism of oxidation of amines over meso Cs/MnO_x following Mars-Van-Krevelen mechanism ……65

Scheme 4.1 Versatile tandem oxidation process from alcohol by meso Cs/MnO_x ……...72

Scheme 4.2. Possible reaction pathways of imidazole formation over meso Cs/MnO_x …….. 85

Scheme 4.3. Possible reaction pathways of oxidation of phenethyl alcohol by oxidation-decarboxylation-oxygen rebound mechanism over meso Cs/MnO_x. A trace amount of benzaldehyde was detected by GC-MS ……90

Scheme 4.4. Possible manganese oxide assisted oxygen rebound mechanism. No reaction was observed when a radical inhibitor was added, which confirmed the radical intermediate formation by single electron transfer (SET) mechanism ……91

Scheme 4.5. Possible reaction pathways of imine formation over meso Cs/MnO_x …….92

Scheme 5.1 Proposed mechanism of oxidative coupling of alkynes by meso Cu/MnO_x ……134

CHAPTER 1. Introduction

1.1 Overview of Catalytic Oxidation

Catalytic oxidation of natural products is one of the most popular and cheapest techniques for production of fine chemicals from natural substrates. Selective oxidations of organic substrates such as alcohols, amines and hydrocarbons are of interest in the field of synthetic organic chemistry and industrial applications[1,2]. Traditionally, various chemical oxidants, such as peroxides (*tert*-butylhydroperoxide or hydrogen peroxide), metal salts [potassium permanganate ($KMnO_4$), chromium trioxide (CrO_3), sodium dichromate ($Na_2Cr_2O_7$)] and ozone are used for these oxidation reactions[3,4]. However, production of large amount of toxic wastes and necessary but difficult separation steps make these processes environmentally and industrially unfavorable.

From the viewpoint of green chemistry, the design of novel methodologies for oxidation, preferably under aerobic atmospheric conditions, without any additives, is highly desirable. Extensive research has been performed over the past decades to improve the selective oxidation reactions in catalytic, mild and aerobic conditions[5-9]. Although a green oxidant, air is very inert towards organic substrates, especially for the strong C-H bond activation due to the typical ground state of oxygen. The other obstacle associated with aerobic oxidation is the failure of scale up procedures. Therefore, catalytic oxidation with ambient air as the ultimate oxidant represent one of the most demanding challenges in chemical industry.

1.2 Heterogeneous catalysis

Heterogeneous catalysis has widespread applications in chemical and pharmaceutical industries[10]. The key objective of green chemistry is to make a sustainable process by optimizing resources and minimizing waste. Heterogeneous catalysis is an important tool in that case[11]. By definition, heterogeneous catalysts are materials present in different phases (usually solid) than the reactant. Therefore, heterogeneous catalysts are more advantageous over homogeneous systems due to easy separation from the reaction medium. Moreover, the stability of heterogeneous catalysts is quite notable even in extremely harsh condition.

1.3 Mesoporous materials

Porous nanostructured materials have been recognized as popular heterogeneous catalytic systems[12]. They are ideal for providing a high surface area scaffold to which active metals can be grafted. Moreover, their porous network is very effective for shape-selective catalysis. Since the discovery of mesoporous silica and aluminosilicates (M41S family) by Mobil Oil Corporation in 1992, mesoporous materials have attracted a great deal of interest and have been the subject of thousands of research articles, patents and book chapters[13]. According to the IUPAC definition, mesoporous materials are types of porous materials having pore size between 2 to 50 nm. The popularity of mesoporous materials can be attributed to their enhanced physicochemical, catalytic, adsorption and optical properties compared to their nonporous counterparts[14-16]. High surface area, nanocrystalline wall structure, tunable porous networks, and high pore volume are the important factors as the origins of the enhanced properties of mesoporous materials. Numerous synthetic methods have been developed in past decades for the synthesis of mesoporous materials. Popular

mesoporous materials are synthesized by a hard template or a soft template procedure. The flexibility in synthesis conditions allows one to synthesize mesoporous silica materials with tunable pore sizes (2-50 nm), mesostructure (i.e. 2D Hexagonal, FCC, BCC, 3D), and with diverse morphologies (i.e. spheres, rods, ropes, and cubes)[17].

The possibility of control over the porous architecture and morphology depending upon the requirement of a particular reaction is the main important tool for designing mesoporous materials as active heterogeneous catalysts[18]. Catalytic reactions on mesoporous supports involve basic steps like adsorption and diffusion of reactants in solid surfaces following reaction between reactants and desorption of products and regeneration of catalyst. Therefore, materials having high surface area are the best candidates for heterogeneous catalysts. Due to their intrinsic structural features, mesoporous nanostructured materials have been recognized as popular catalytic systems[18,19]. They are ideal for providing a high surface area scaffold to which active metals can be tethered. Further, tunable pore size offers good flexibility for the transportation of organic moieties. Moreover, the hydrophobicity or polarity of the surface can be tuned to influence catalytic reactions. These materials are thermally stable, non-corrosive, non-toxic, air and moisture stable and often highly reusable.

Most of the synthesized mesoporous materials are based on silica, which, in spite of having high surface area and tunable pore diameter, is not active in any catalytic reactions. Moreover, the collapse of porous structure upon heat treatment is well-known for mesoporous silica materials. On the other hand, mesoporous transition metal oxides (MTMO) have shown promise for performing a wide range of catalytic transformations due to co-existing multiple oxidation states[20,21]. The presence of multiple oxidation states

of the MTMOs as a result of vacant d orbitals is very crucial in electron transfer processes during redox catalytic reactions. Transition metal oxides can be further modified by adding several dopants and promoter ions to design a specific catalyst for a specific reaction. However, direct synthesis of MTMOs still remains a challenge[20]. In addition, these mesoporous MTMOs often suffer from low order arrangements and no control over the porous network compared to traditional mesoporous silica. These MTMOs also have very low thermal stability, since the low flexibility of the metal-oxygen bond in crystalline phases is unable to accommodate the structure directing agent (surfactant micelles).

1.4 UCT (University of Connecticut) mesoporous material

In 2013, our research group introduced a thermally stable, crystalline, thermally controlled mesoporous group of materials[22]. The materials were synthesized by a soft templated evaporation induced self-assembly procedure (**Figure 1.1**). Unlike conventional mesoporous material synthesis, an inverse surfactant micelle was used as a soft template. Transition metal and ion precursors loaded inverse micelles packed in a random fashion to build the mesoporous structure. The reaction solvent was an acidic (HNO_3) 1-butanol solution. Evaporation of the solvent (by heat treatment) along with NO_x formation (by thermal decomposition of nitrates) had driven the reaction. The nitrate ions had dual roles. First, the hydrotropic[23] nature of the nitrate ions hydrated the core of the inverse surfactant micelles by penetrating in, which pulled the positively charged manganese oxo-clusters to the core of the inverse micelles by increasing their solubility. Second, the nitrate ions decomposed to form NO_x species, which controlled the pH and the sol gel chemistry of Mn sols. Solvent extraction by ethanol was performed to remove surfactants to form the mesoporous materials. Chemisorbed species (nitrates and carboxylates) were removed by

a heat treatment at 150°C for 12 h, followed by a second heat treatment at 250°C for 3 h. The mesopores are formed by connected inter-particle voids. The mesoporous structure can be easily controlled by further heat treatment.

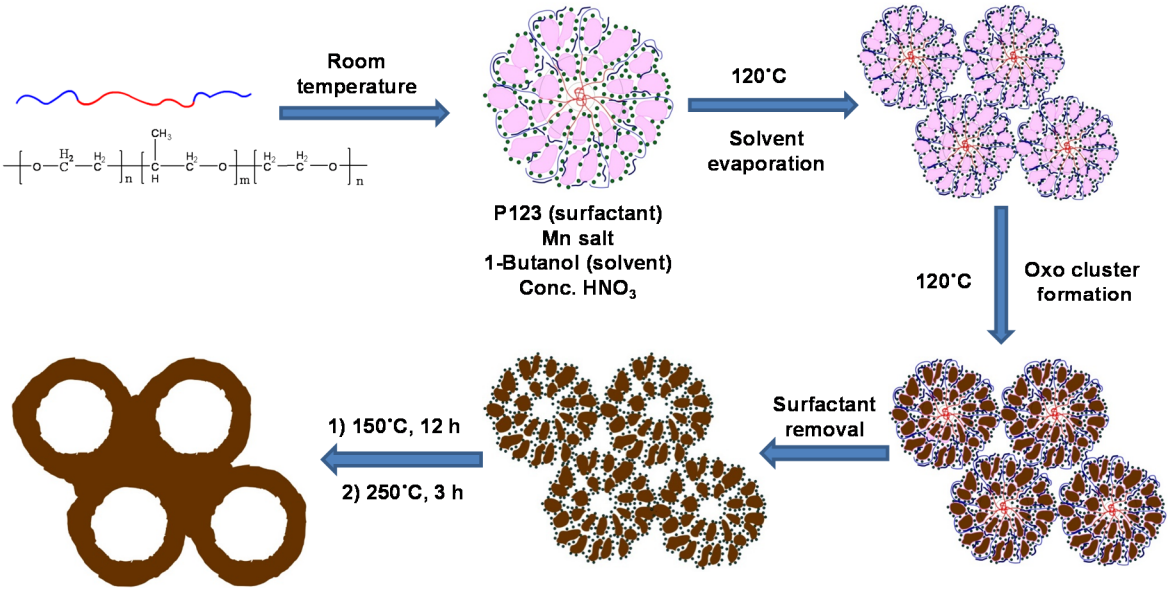

Figure 1.1 Formation mechanism of mesoporous manganese oxide by UCT synthesis procedure. Metal loaded inverse micelles are packed and inorganic components condensed and oxidized. Surfactants are removed by solvent extraction and adsorbed species are eliminated by heat treatment.

The UCT synthetic approach allows one to synthesize different mesoporous oxide materials of transition metals, metalloids, mixed oxides using a single synthetic strategy. Precise control over the pore size, surface area, and crystallinity by simple heat treatment cycles makes these types of materials superior over their nonporous counterparts in different catalytic applications such as oxidation of alcohols, low temperature CO and CH_4 oxidation, and water splitting reactions[24-28]. For example, Cs promoted mesoporous manganese oxide (UCT-18-Cs) exhibited a bifunctional catalytic role (oxidation and then *in situ* esterification)[22]. The inactivated aliphatic alcohol 1-decanol was oxidized to 1-

decanoic acid and then 1-decanoic acid combined with 1-decanol to produce decyl decanoate. Whereas, nonpromoted UCT-1 and other manganese oxide catalysts (K-OMS-2, amorphous manganese oxide, Mn_2O_3) could only perform oxidation of 1-decanol to 1-decanal.

1.5 Manganese oxides in catalytic oxidation

Among the transition metal oxides, manganese oxides deserve special interest in catalytic oxidation reactions. Easily exchangeable multiple oxidation states, high abundancy, thermally stable structural forms (more than 30 crystal structures corresponding to different polymorphs are known to exist), and dioxygen reduction ability are some of the important properties of this material[29]. The tunable redox properties of Mn and mobility of labile lattice oxygen make the manganese oxide materials powerful catalysts in oxidative reactions. Like other transition metals, manganese oxides also can accommodate cations either on the surface as promoter ions [30] or in their structures as charge balancing ions [31] (as in octahedral molecular sieve, $KMn_8O_{16}.nH_2O$ or K-OMS-2, where K^+ can reside in the tunnel for charge balancing).

The diversity of synthesis methods allows preparation of different forms of manganese oxide of varying porosity and crystallinity, such as octahedral molecular sieves (OMS), octahedral layer (OL), amorphous manganese oxide (AMO), birnessite, α-manganese oxide and mesoporous manganese oxide[29]. For example, the two highly active manganese oxide phases in oxidative transformations, are a crystalline octahedral molecular sieve, $KMn_8O_{16}.nH_2O$ or OMS-2, and an amorphous phase. OMS-2 has a 2X2 tunnel structure, which is built by edge and corner sharing [MnO_6] octahedral units leading to different pore sizes[32]. OMS-2 has a mixed valent manganese framework with a higher

amount of Mn^{4+}. K^{+} ions are situated in the tunnel and can be easily exchanged by other inorganic cations. Catalytic activity can be successfully tuned by applying different synthesis procedures to change the porosity and surface area of OMS-2. On the other hand, amorphous manganese oxide (AMO) has a disordered structure with a mixed valence of Mn^{3+} and Mn^{4+}, which consists of random aggregation of nanoparticles with high surface area (184 m^2g^{-1})[33]. AMO has shown high activity in various oxidation reactions including water oxidation and photochemical 2-proponal oxidation. The catalytic activity of AMO can also be related to the cation vacancies in the structure, which can act as the active sites to adsorb amine molecules. These mixed valent porous materials have excellent redox properties that lead to the design of highly efficient manganese based oxidation catalysts. Manganese oxide based materials have been utilized in different types of catalytic oxidation reactions, such as selective oxidation of alcohols to aldehydes[34], hydrocarbons to alcohols and ketones[35], styrenes to styrene oxides[36], alcohols to amides[37-41], amines to imines[42-44], and total oxidation of volatile organic compounds[45], methane[25] and carbon monoxide[46].

1.7 References

(1) ten Brink, G.-J.; Arends, I. W.; Sheldon, R. A. *Science* **2000**, *287*, 1636-1639.

(2) Sheldon, R. *Metal-catalyzed oxidations of organic compounds: mechanistic principles and synthetic methodology including biochemical processes*; Elsevier, 2012.

(3) Muzart, J. *Chem. Rev.* **1992**, *92*, 113-140.

(4) Tong, X.; Xu, J.; Miao, H. *Adv. Synth. Catal.* **2005**, *347*, 1953-1957.

(5) Stahl, S. S. *Science* **2005**, *309*, 1824-1826.

(6) Zhang, P.; Gong, Y.; Li, H.; Chen, Z.; Wang, Y. *Nat. Commun.* **2013**, *4*, 1593.

(7) Hoover, J. M.; Stahl, S. S. *J. Am. Chem. Soc.* **2011**, *133*, 16901-16910.

(8) Wendlandt, A. E.; Suess, A. M.; Stahl, S. S. *Angew. Chem., Int. Ed.* **2011**, *50*, 11062-11087.

(9) Wang, D.; Jaworski, J. N.; Stahl, S. S. *Liquid Phase Aerobic Oxidation Catalysis: Industrial Applications and Academic Perspectives* John Wiley & Sons, **2016**.

(10) Sheldon, R.; Downing, R. *Appl. Catal., A: Gen.* **1999**, *189*, 163-183.

(11) Sheldon, R. A.; Van Bekkum, H. *Fine chemicals through heterogeneous catalysis*; John Wiley & Sons, 2008.

(12) Zaera, F. *Chem. Soc. Rev.* **2013**, *42*, 2746-2762.

(13) Kresge, C.; Leonowicz, M.; Roth, W.; Vartuli, J.; Beck, J. *Nature* **1992**, *359*, 710-712.

(14) Davis, M. E. *Nature* **2002**, *417*, 813-821.

(15) Vallet-Regí, M.; Balas, F.; Arcos, D. *Angew. Chem., Int. Ed.* **2007**, *46*, 7548-7558.

(16) Beck, J. S.; Vartuli, J. C. *Curr. Opin. Solid State Mater. Sci.* **1996**, *1*, 76-87.

(17) Poyraz, A. S.; Meng, Y.; Biswas, S.; Suib, S. L. *Perovskites and Related Mixed Oxides Concepts and Applications*, Wiley-VCH Verlag GmbH & Co. KGaA, Weinheim, Germany. ch31,699-718.

(18) Taguchi, A.; Schüth, F. *Microporous Mesoporous Mater.* **2005**, *77*, 1-45.

(19) Pal, N.; Bhaumik, A. *RSC Adv.* **2015**, *5*, 24363-24391.

(20) Schüth, F. *Chem. Mat.* **2001**, *13*, 3184-3195.

(21) Yu, C.; Tian, B.; Zhao, D. *Curr. Opin. Solid State Mater. Sci.* **2003**, *7*, 191-197.

(22) Poyraz, A. S.; Kuo, C.-H.; Biswas, S.; King'ondu, C. K.; Suib, S. L. *Nat. Commun.* **2013**, *4*, 2952.

(23) Poyraz, A. S.; Dag, O. m. *J. Phys. Chem. C* **2009**, *113*, 18596-18607.

(24) Biswas, S.; Poyraz, A. S.; Meng, Y.; Kuo, C.-H.; Guild, C.; Tripp, H.; Suib, S. L. *Appl. Catal., B: Environ.* **2015**, *165*, 731-741.

(25) Wasalathanthri, N. D.; Poyraz, A. S.; Biswas, S.; Meng, Y.; Kuo, C.-H.; Kriz, D. A.; Suib, S. L. *J. Phys. Chem. C* **2015**, *119*, 1473-1482.

(26) Pahalagedara, L. R.; Poyraz, A. S.; Song, W.; Kuo, C.-H.; Pahalagedara, M. N.; Meng, Y.-T.; Suib, S. L. *Chem. Mat.* **2014**, *26*, 6613-6621.

(27) Song, W.; Poyraz, A. S.; Meng, Y.; Ren, Z.; Chen, S.-Y.; Suib, S. L. *Chem. Mat.* **2014**, *26*, 4629-4639.

(28) Kuo, C.-H.; Mosa, I. M.; Poyraz, A. S.; Biswas, S.; El-Sawy, A. M.; Song, W.; Luo, Z.; Chen, S.-Y.; Rusling, J. F.; He, J.; Suib, S. L. *ACS Catal.* **2015**, *5(3)*, 1693-1699.

(29) Suib, S. L. *Acc. Chem. Res.* **2008**, *41*, 479-487.

(30) Kim, S. C.; Shim, W. G. *Appl. Catal., B: Environ.* **2010**, *98*, 180-185.

(31) Nyutu, E. K.; Chen, C.-H.; Sithambaram, S.; Crisostomo, V. M. B.; Suib, S. L. *J. Phys. Chem. C* **2008**, *112*, 6786-6793.

(32) DeGuzman, R. N.; Shen, Y.-F.; Neth, E. J.; Suib, S. L.; O'Young, C.-L.; Levine, S.; Newsam, J. M. *Chem. Mat.* **1994**, *6*, 815-821.

(33) Cao, H.; Suib, S. L. *J. Am. Chem. Soc.* **1994**, *116*, 5334-5342.

(34) Son, Y. C.; Makwana, V. D.; Howell, A. R.; Suib, S. L. *Angew. Chem.* **2001**, *113*, 4410-4413.

(35) Opembe, N. N.; Son, Y. C.; Sriskandakumar, T.; Suib, S. L. *ChemSusChem* **2008**, *1*, 182-185.

(36) Ghosh, R.; Shen, X.; Villegas, J. C.; Ding, Y.; Malinger, K.; Suib, S. L. *J. Phys. Chem. B* **2006**, *110*, 7592-7599.

(37) Wang, Y.; Kobayashi, H.; Yamaguchi, K.; Mizuno, N. *Chem. Commun.* **2012**, *48*, 2642-2644.

(38) Yamaguchi, K.; Kobayashi, H.; Oishi, T.; Mizuno, N. *Angew. Chem.* **2012**, *124*, 559-562.

(39) Yamaguchi, K.; Kobayashi, H.; Wang, Y.; Oishi, T.; Ogasawara, Y.; Mizuno, N. *Catal. Sci. Technol* **2013**, *3*, 318-327.

(40) Wang, Y.; Yamaguchi, K.; Mizuno, N. *Angew. Chem.* **2012**, *124*, 7362-7365.

(41) Yamaguchi, K.; Wang, Y.; Mizuno, N. *Chem. Lett.* **2012**, *41*, 633-635.

(42) Sithambaram, S.; Kumar, R.; Son, Y.-C.; Suib, S. L. *J. Catal.* **2008**, *253*, 269-277.

(43) Chen, B.; Li, J.; Dai, W.; Wang, L.; Gao, S. *Green Chem.* **2014**, *16*, 3328-3334.

(44) Zhang, Z.; Wang, F.; Wang, M.; Xu, S.; Chen, H.; Zhang, C.; Xu, J. *Green Chem.* **2014**, *16*, 2523-2527.

(45) Genuino, H. C.; Dharmarathna, S.; Njagi, E. C.; Mei, M. C.; Suib, S. L. *J. Phys. Chem. C* **2012**, *116*, 12066-12078.

(46) Xia, G.; Yin, Y.; Willis, W.; Wang, J.; Suib, S. *J. Catal.* **1999**, *185*, 91-105.

CHAPTER 2. Ion Induced Promotion of Activity Enhancement of Mesoporous Manganese Oxides for Aerobic Oxidation Reactions

2.1 Abstract

Inverse micelle templated mesoporous manganese oxide (University of Connecticut mesoporous material, UCT-1) and five cation promoted mesoporous manganese oxides (UCT-18-X, X = Mg^{2+}, Ca^{2+}, K^{+}, Na^{+} and Cs^{+}) having trace amounts of alkali metal ions as promoters with tunable porosity and crystallinity were synthesized. The materials were tested for selective aerobic alcohol oxidation, and the catalytic activity followed the order of UCT-1 <UCT-18-Mg <UCT-18-Ca <UCT-18-K <UCT-18-Na <UCT-18-Cs. The catalytic activity was correlated with the increase in basicity of the materials, which in turn was a consequence of the promoting effect of ions in manganese oxide. The retention of an amorphous state, low reducibility, and the effects of lattice oxygen are the other key factors responsible for the enhanced catalytic activity. The UCT-18-Cs catalyst was found to oxidize various alcohols to the corresponding aldehydes and ketones selectively (100% selectivity) with very high conversion (as high as 100%). The UCT-18-Cs also exhibited solvent free green oxidation of 1.3.5-trimethylbenzene to yield 3,5-dimethylbenzoic acid and 3,5-dimethylbenzyl-3,5-dimethylbenzoate with > 90% conversion and 90% selectivity of acid and 9% selectivity of ester.

2.2 Background and Significance

The selective oxidation of alcohols to carbonyl compounds is one of the common and elegant classes of molecular transformations in synthetic organic chemistry. The

desired carbonyl products are high value components used in fine chemicals, pharmaceutical, and perfume industries. Numerous catalytic systems have been used to perform this partial oxidation of alcohols [1-3]. The two major problems associated with heterogeneous catalysts are the lifetime of the catalyst (catalyst deactivation) and the leaching of active species from the solid surface to the solution [4]. The design of an efficient heterogeneous catalyst system should ideally involve mild and environmentally friendly reaction conditions (air as oxidant, low temperature, low catalyst loading, avoidance of toxic materials, and minimum waste disposal with proper reusability) in addition to high efficiency. The selective C-H bond oxidation at the benzylic position to the corresponding oxy functional products is one of the important and challenging aspects in synthetic organic chemistry [5-8]. For example, the methyl benzoic acids (oxidation products of methyl aromatics) have versatile uses in chemical and pharmaceutical industries [9]. The traditional oxidizing agents involved in these oxidation reactions are stoichiometric amounts of oxidants like potassium permanganate ($KMnO_4$), chromium trioxide (CrO_3), sodium dichromate ($Na_2Cr_2O_7$) and nitric acid (HNO_3) [10]. Large amounts of toxic waste and difficulty in separations make these processes environmentally and industrially unfavorable. Despite the industrial importance, environmentally friendly oxidation processes are rarely described in the literature. Some of the efficient catalytic systems involve oxidants such as metaloxo materials, *tert*-butyl hydroperoxide (TBHP) or hydrogen peroxide (H_2O_2) and base additives [11-14]. However, these systems often suffer from low conversion (of alkylbenzenes), as well as requiring the use of conditions like high pressure and temperature. An efficient and economically feasible catalyst system should

perform alkylbenzene oxidation with high selectivity towards the corresponding acid under aerobic conditions.

Herein, 5 different ion promoted mesoporous manganese oxide materials were synthesized by using 5 different cations (Mg^{2+}, Ca^{2+}, K^{+}, Na^{+} and Cs^{+}) with tunable mesostructure parameters (such as pore size, pore volume, surface area). The synthesis relies on inverse micelle formation and unique NOx chemistry. The NOx species are formed *in situ* by thermal decomposition of NO_3^-. The metal oxide nanoparticles are packed closely in a random fashion to build the mesostructure. Selective aerobic oxidations of alcohols and oxidations of inert alkylbenzenes were performed using the catalysts and the catalytic activity was also compared with conventional active manganese oxide catalysts.

2.3 Experimental

2.3.1 Synthesis of UCT-1

In a typical synthesis 0.02 mol of manganese nitrate tetrahydrate ($Mn(NO_3)_2.4H_2O$) and 0.134 mol of 1-Butanol were added to a 120 mL beaker. To this solution 0.0034 mol of poly(ethyleneglycol)-*block*-poly(propyleneglycol)-*block*-poly(ethyleneglycol) (pluoronic P123, $PEO_{20}PPO_{70}PEO_{20}$, molar mass 5750 g mol^{-1}) and 0.0032 mol of concentrated nitric acid (HNO_3) were added and the mixture was stirred at room temperature until the solution became clear (light pink). The solution was then kept in an oven at 120°C for 3 h under air. The resulting black material was washed with excess ethanol, centrifuged and dried in a vacuum oven overnight. The dried black powders were subjected to a heating cycle. First they were heated at 150°C for 12 h and cooled to room temperature under ambient conditions, followed by a second heating step of 250°C for 3 h.

2.3.2 Synthesis of UCT-18

In a typical synthesis 0.02 mol of manganese nitrate tetrahydrate ($Mn(NO_3)_2.4H_2O$) and 0.134 mol of 1-Butanol were added into a 120 mL beaker. To this solution 0.0034 mol of poly(ethyleneglycol)-*block*-poly(propyleneglycol)-*block*-poly(ethyleneglycol) (Pluoronic P123, $PEO_{20}PPO_{70}PEO_{20}$, molar mass 5750 g mol^{-1}) and 0.032 mol of concentrated nitric acid (HNO_3) were added and the mixture was stirred at room temperature until the solution became clear (light pink). To this clear solution 100 µL of 2.0M XNO_3 (X= Cs, K, Na) and $X(NO_3)_2$ (X= Ca, Mg) was added maintaining the Mn/X ratio 100/1, mol/mol. The resulting clear solution was then kept in an oven at 120°C for 3 h under air. The black material was washed with excess ethanol, centrifuged, and dried in a vacuum oven overnight. The dried black powders were subjected to a heating cycle. First they were heated at 150°C for 12 h and cooled to room temperature under ambient conditions, followed by a second heating step of 250°C for 3 h.

* It is recommended to perform all reactions in ovens with proper ventilation due to the release of toxic NOx from the gel during the reaction.

2.3.3 Catalyst Characterization

Powder X-Ray diffraction (PXRD) analyses were performed on a Rigaku Ultima IV diffractometer (Cu Kα radiation, λ=1.5406 Å) with an operating voltage of 40 kV and a current of 44 mA. The low-angle PXRD patterns were collected over a 2θ range of 0.5–10° with a continuous scan rate of 0.5° min^{-1}, where the wide-angle PXRD patterns were collected over a 2θ range of 5–75° with a continuous scan rate of 1.0° min^{-1}. The nitrogen adsorption desorption experiments were done with a Quantachrome Autosorb-1-1C automated adsorption system. The samples were degassed at 150°C for 6 h under helium

prior to measurement. The surface areas were calculated using the Brunauer–Emmett–Teller (BET) method, and pore sizes and pore volumes were calculated from the desorption branch of the isotherm using the Barrett–Joyner–Halenda (BJH) method. A Zeiss DSM 982 Gemini field emission scanning electron microscope (FE-SEM) with a Schottky emitter at an accelerating voltage of 2.0 kV and a beam current of 1.0 mA was used for determination of surface morphology of the materials. The samples were ultrasonically dispersed in ethanol and deposited on silicon wafers prior to the analyses. High-resolution transmission electron microscopy (HR-TEM) images were recorded on a JEOL 2010 FasTEM microscope operating at 200 kV. The samples were prepared by using a focused-ion-beam (FIB) technique to make thin films to be observed by HR-TEM. The CO_2 chemisorption experiments were performed using a Quantachrome Autosorb-1-1C automated adsorption system. All the samples were heated in helium under vacuum at 150°C for 6 h prior to the experiment. The adsorption studies of UCT-18 and UCT-1 were done at room temperature. Then, both adsorption and desorption isotherms were measured for UCT-18-Cs, UCT-1, K-OMS-2 and commercial Mn_2O_3 at 0°C, 25°C and -78°C. Temperature-resolved *in situ* powder X-ray diffraction (TR-PXRD) analysis was performed in an XTRA X-ray diffractometer (Cu Kα radiation) equipped with an Anton Parr XRK 900 heating chamber. The structural stabilities of UCT-1 and UCT-18 Cs materials were investigated from 250°C to 550°C using a ramp rate of 5°C min^{-1} under air. Diffraction patterns were obtained in the range of 5-75° 2θ at scanning rate of 2.0° min^{-1}. X-ray photoelectron spectroscopy (XPS) was done on a PHI model 590 spectrometer with multiprobes (ΦPhysical Electronics Industries Inc.), using Al-K radiation (λ= 1486.6 eV) as the radiation source. The powder samples were pressed on carbon tape mounted on

adhesive copper tape stuck to a sample stage placed in the analysis chamber. The XPS spectra were analyzed and fitted using CasaXPS software (version 2.3.12). The C 1s photoelectron line at 284.6 eV was used as a reference for correction of the surface charging. A mixture of Gaussian (70%) and Lorentzian (30%) functions was used for the least-squares curve fitting procedure. The temperature programmed reduction (TPR), temperature programmed oxidation (TPO), and mass spectrometry were done with a Thermolyne 79300 model tube furnace equipped with an MKS gas analyzer coupled with a quadrupole mass selective detector. The samples were treated with Ar for 2 h at 250°C before the experiment. In the experiments 10% vol. H_2 in Ar (for H_2-TPR) and 10% vol. O_2 in Ar (for O_2-TPO) mixtures were used at a constant flow rate in the temperature range 50 - 600°C at a ramp of 10°C min^{-1}. The temperature programmed desorption (TPD) experiments were performed with the same Thermolyne 79300 model tube furnace equipped with an MKS gas analyzer coupled with a quadrupole mass selective detector using pure Ar as carrier gas. The sample was used without any pretreatment.

2.3.4 Catalytic Activity Measurement

2.3.4.1 Alcohol Oxidation

In a typical alcohol oxidation procedure, alcohol (1.0 mmol), catalyst (50 mg) and toluene (15 mL) were put in a 50 mL two-necked round bottom flask. The flask with the reaction mixture with a reflux condenser attached was immersed in a silicon oil bath preheated to the reaction temperature. The reaction mixture was refluxed under vigorous stirring (700 rpm) for the required time under air flow. After reaction, the mixture was cooled, the catalyst was removed by filtration, and GC-MS was used to analyze the filtrate. The conversion and selectivity were measured by gas chromatography-mass spectrometry

(GC-MS) methods using a 7820A GC system connected with a thermal conductivity detector of 5975 series MSD from Agilent Technologies. A nonpolar cross-linked methyl siloxane column with dimensions of 12 in × 0.200 mm × 0.33 μm was used. The conversions were determined based on concentration of alcohols. The selectivities were calculated based on aldehydes or ketones as the only products. Most reactions were repeated at least three times and the average values of conversions were used.

2.3.4.2 1,3,5-Trimethylbenzene Oxidation

In a typical oxidation reaction, 1,3,5-trimethylbenzene (required amount in mL) and catalyst (100 mg) were put in a 50 mL two-necked round bottom flask. The flask with the reaction mixture with a reflux condenser attached was immersed in a silicon oil bath pretreated at 130°C. The reaction mixture was then heated at 130°C under vigorous stirring (700 rpm) for a certain time under air flow. After reaction, the mixture was cooled, the catalyst was removed by filtration, and GC-MS was used to analyze the filtrate. The conversions were determined based on concentration of substrates. The selectivities were calculated based on aldehydes, acids and esters as the products.

2.4 Structural Characterization

Figure 2.1A and **Figure 2.1B** represent the low and the wide angle PXRD patterns of the UCT-18 materials respectively. The low angle diffraction lines, like those of other UCT materials, indicate the existence of an ordered mesostructure. The low-angle PXRD line positions are almost the same for UCT-18 and UCT-1 materials (in nm), indicating very similar particle sizes (**Table 2.1**). The wide-angle PXRD patterns suggest an amorphous nature of the materials. The N_2 adsorption and desorption isotherms (**Figure 2.1C**), show Type IV adsorption isotherms, followed by a Type I hysteresis loop, indicating regular

mesoporous structures for all materials. The BET surface areas are summarized in **Table 1**. All the UCT-18 materials exhibit higher surface areas with UCT-18-Na having the maximum (152 m^2/g). The BJH desorption pore size distributions of UCT-18 materials are the same (pore diameter 3.4 nm) (**Figure 2.1D, Table 2.1**). The FE-SEM images of UCT-18 materials (**Figure 2.2A-E**) show very similar features with no distinguishable differences. They all show aggregated micron size rounded particles. The HR-TEM images (**Figure 2.2F-H**) show aggregated nanoparticles with an average particle size of 10-12 nm and formation of a porous network in between the particles. The higher magnification HR-TEM images (**Figure 2.2B**) indicate that the nanoparticles are crystalline. The lattice fringes of 0.49 nm and 0.27 nm can be indexed to the crystal phase (200) and (222) of the Mn_2O_3 (bixbyite). The lack of diffraction in the PXRD can be attributed to the nano-particle nature of the materials.

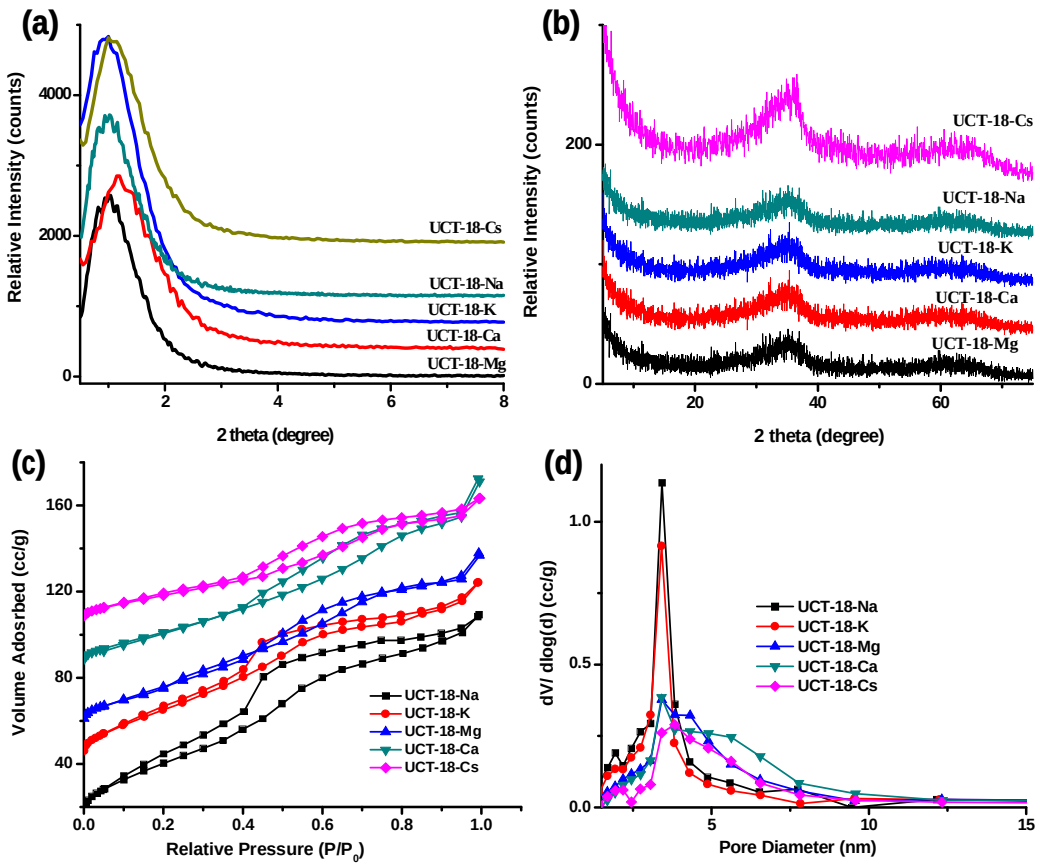

Figure 2.1 (A) Low angle (0.5° – 8°) PXRD patterns , (B) Wide angle (5° – 75°) PXRD patterns, (C) N_2 sorption isotherms, and (D) BJH desorption pore size distributions of cation promoted mesoporous manganese oxides (UCT-18-X, X= Mg^{2+}, Ca^{2+}, K^{+}, Na^{+}, and Cs^{+})

Table 2.1 Structural parameters of UCT-1 and UCT-18[a]

Metal	Title	Surface Area (m^2/g)	Pore Diameter (nm)	Pore Volume (cc/g)	Low-Angle PXRD peak position (nm)
Mn	UCT-1	200	2.8	0.153	6.7
Mn/Cs	UCT-18-Cs	78	3.4	0.107	7.6
Mn/Na	UCT-18-Na	152	3.4	0.192	8.5
Mn/K	UCT-18-K	149	3.4	0.161	8.5
Mn/Ca	UCT-18-Ca	101	3.4	0.163	7.1
Mn/Mg	UCT-18-Mg	97	3.4	0.151	8.9

[a] All materials were calcined at 150°C for 12 h, then at 250°C for 3 h.

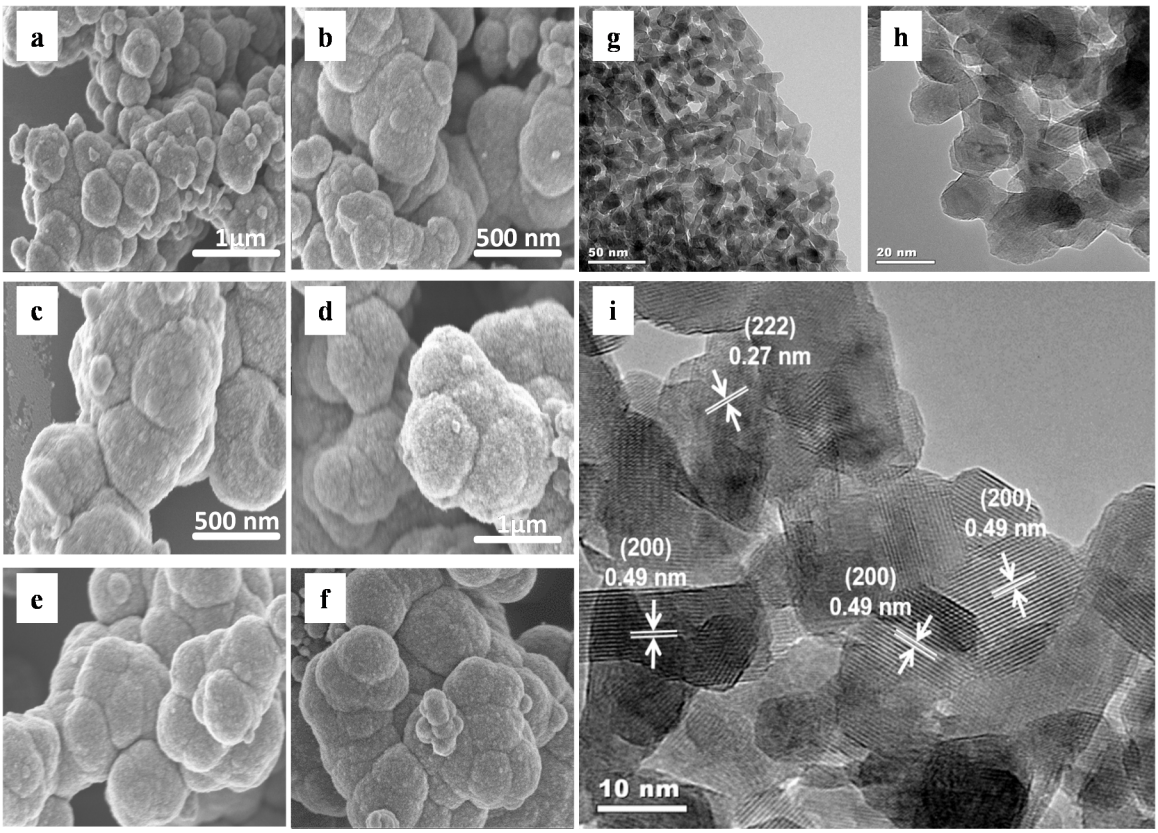

Figure 2.2 FE-SEM images of (A) UCT-18-Cs, (B) UCT-18-Na, (C) UCT-18-K, (D) UCT-18-Ca, (E) UCT-18-Mg (F) UCT-1 materials and HR-TEM images of UCT-18-Cs material (G, H) at lower magnifications (I) at higher magnification. The measured lattice distances 0.49 and 0.27 nm are indexed to bixbyite Mn_2O_3 (200) and (222) planes

The relative basicity of the materials was determined by CO_2 chemisorption studies, because of the known role of basicity in oxidation reaction. The CO_2 adsorption isotherms at 298K (**Figure 3**) indicate an increase in basicity with the addition of alkali metal ions for the manganese oxide resulting in an increase of the adsorbed volume of CO_2 being higher for promoted samples. The structural stabilities of UCT-1 and UCT-18-Cs materials were investigated in a temperature range of 250°C to 550°C under air by TR-PXRD

(**Figure 4A and 4B**). The samples are amorphous without any crystalline long-range order. Both UCT-1 and UCT-18-Cs materials transform to the bixbyite (Mn_2O_3) phase with rising temperatures. Interestingly, the addition of trace amounts of Cs cations (Mn/Cs, 3000/1) has a marked effect on the crystallization temperature. The non-promoted mesoporous manganese oxide (UCT-1) transforms from an amorphous state to a crystalline state around 350°C, whereas UCT-18-Cs can retain the amorphous state up to 400°C before crystallizing directly to the bixbyite (Mn_2O_3) phase.

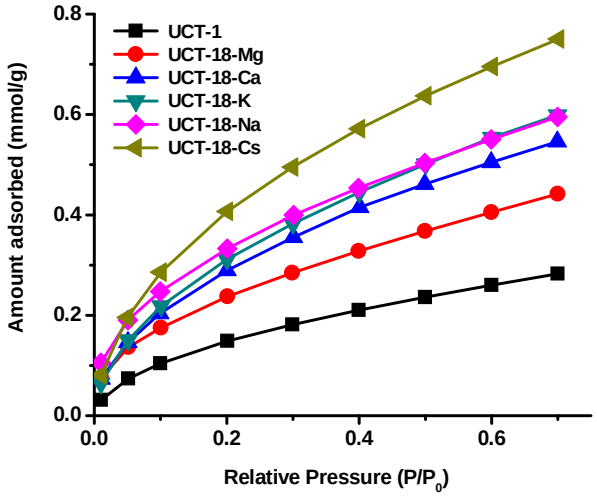

Figure 2.3 CO_2 adsorption isotherms of UCT-1 and UCT-18-X, X= Mg^{2+}, Ca^{2+}, K^+, Na^+, and Cs^+ at 298K.

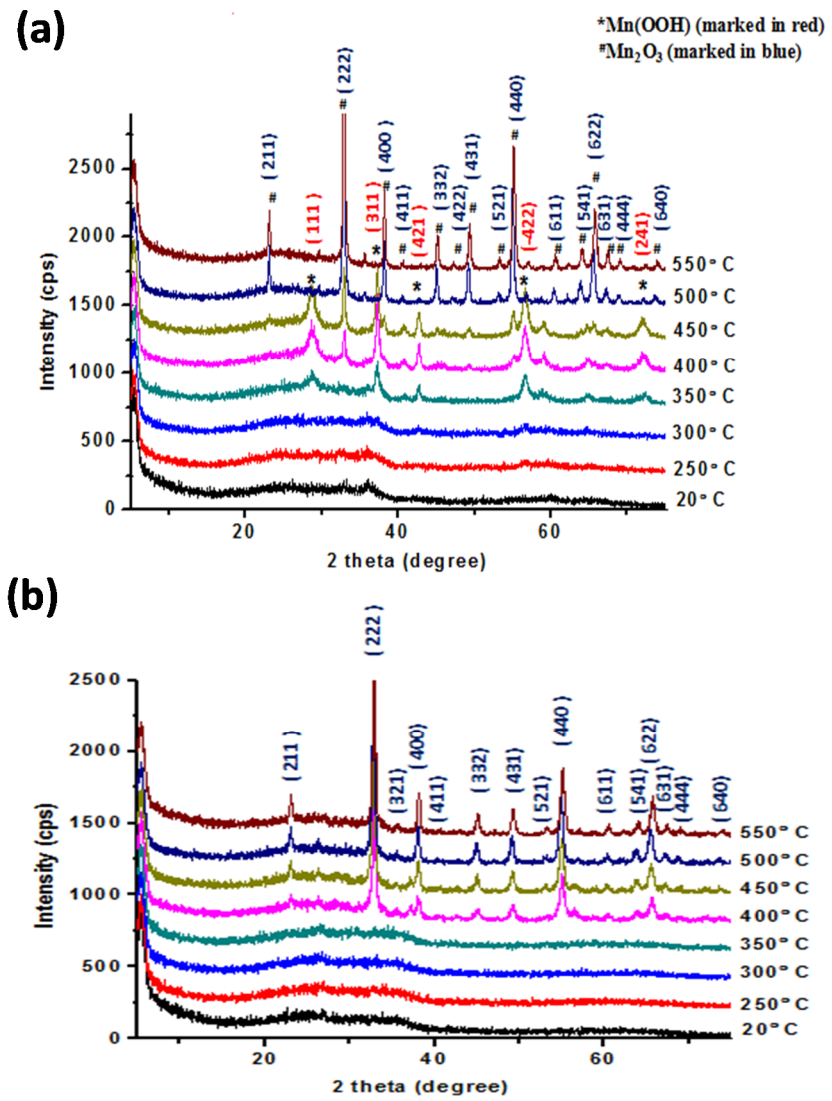

Figure 2.4 Temperature resolved *in situ* PXRD (TR-PXRD) of (A) UCT-18-Cs, and (B) UCT-1. The materials were ramped at 5°C min^{-1} up to 550°C. The diffraction patterns were obtained in the range of 5-75° 2θ at a scanning rate of 2° min^{-1}.

The oxidation reduction profiles of the materials were tested by temperature programmed reduction (H_2-TPR) and oxidation (O_2-TPO) studies. The two major reduction peaks in the H_2-TPR profile (**Figure 5A**) indicate a two-step reduction (Mn_2O_3 to Mn_3O_4 and Mn_3O_4 to MnO). When Cs^+ is incorporated in the manganese oxide (UCT-18-Cs), clear shifts of reduction temperatures to lower values (280°C, 420°C in UCT-1 and

260°C, 400°C in UCT-18-Cs) were observed, which indicate the easy reducible nature of UCT-18-Cs. Whereas, opposite to that of the reduction profile, the oxidation peak shifted to a higher temperature for the UCT-18-Cs (483°C) with respect to nonpromoted UCT-1 (477°C) in the O_2-TPO profile (**Figure 5B**). The temperature programmed desorption (O_2-TPD) under Ar was performed to look into the surface oxygen activity of the materials in the oxidation reaction. A major O_2 loss from both of the materials was observed (532°C for UCT-1 and 570°C for UCT-18-Cs) in the O_2-TPD (**Figure 5C**), which can be ascribed to the loss of lattice oxygen near the surface of the material [15].

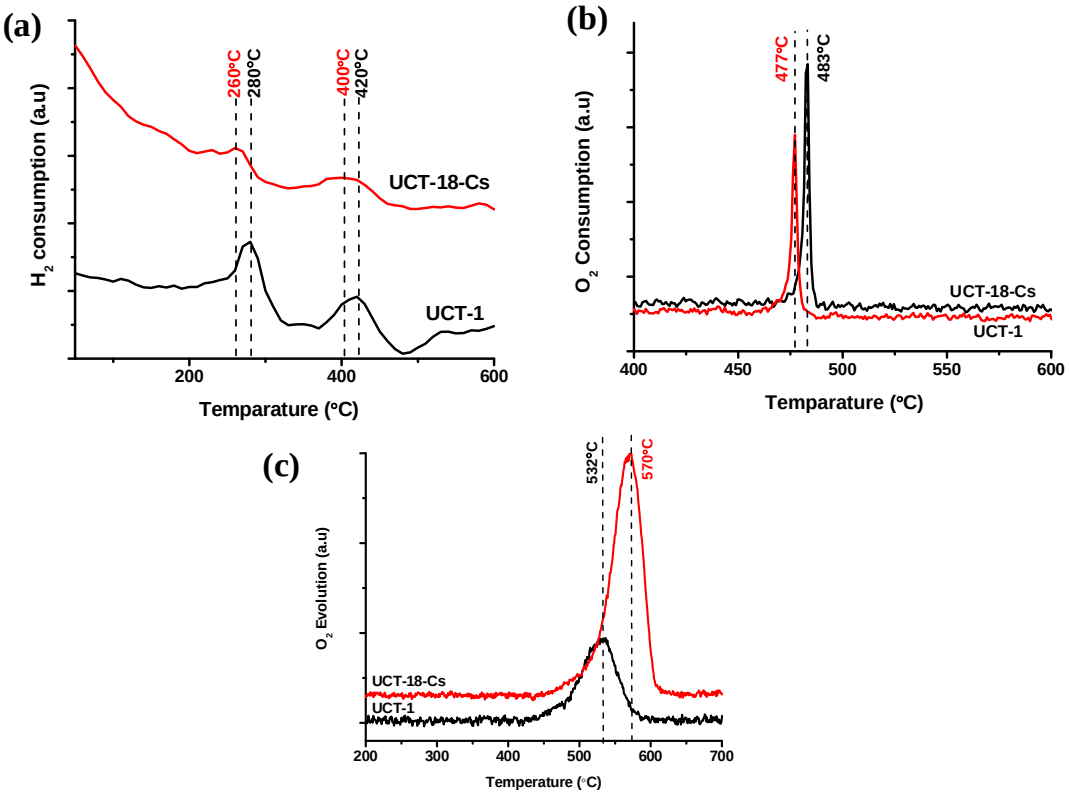

Figure 2.5 (a) H_2-TPR and (b) O_2-TPO and (c) O_2-TPD profile of UCT-18-Cs and UCT-1. The measurements were conducted from room temperature to 700°C (10°C/min) under a stream of 10 % H_2/Ar for H_2-TPR, 10 % O_2/Ar for O_2-TPO and pure Ar for O_2-TPD with a flow rate of 50 sccm.

The XPS measurements were done to investigate the oxidation states of manganese and binding energies of different elements in the materials. The XPS results show that the binding energies (BEs) of Mn fall in the region of BEs of Mn^{3+} for all the materials with negligible differences (**Figure 2.6, Table 2.2**) which is in good agreement with the Mn_2O_3 phase by both H_2-TPR and PXRD analyses. The O 1s region was deconvoluted to three components corresponding to three different oxygen species with distinct binding environments. The first component O_s is the structural or lattice oxygen. The deconvolution results suggest that the area of the O_s peak in all the promoted UCT-18 materials have a relatively higher amounts (**Table 2.2**) than that in the nonpromoted UCT-1 material.

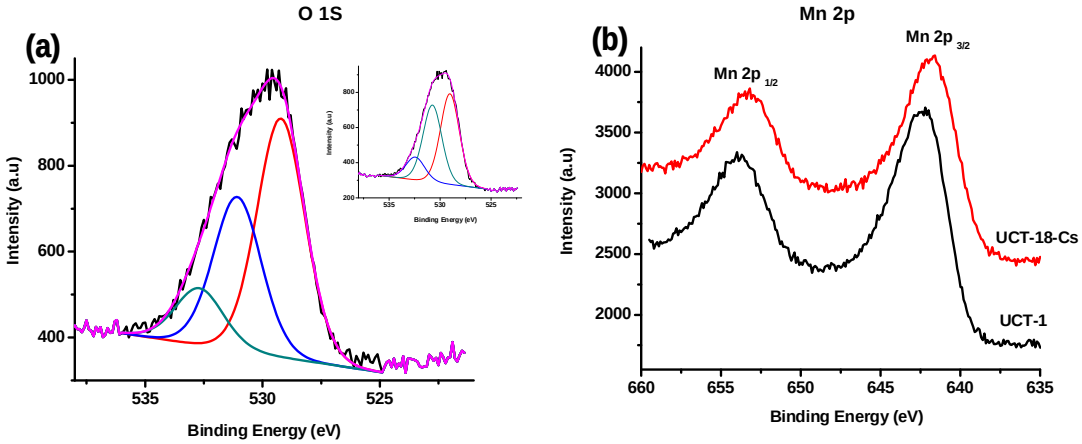

Figure 2.6 XPS analysis: (a) deconvoluted O1s spectra of UCT-18-Cs and UCT-1 (inset) and (b) Mn 2p spectra of UCT-1 and UCT-18-Cs materials. The C 1s photoelectron line at 284.6 eV was used as a reference for correction of surface charging.

Table 2.2 XPS results of UCT-1 and UCT-18-Cs materials.

Materials	Mn (eV)		O_s		O_{ads}		O_{mw}	
	$2p_{3/2}$	$2p_{1/2}$	BE (eV)	%A	BE (eV)	%A	BE (eV)	%A
UCT-1	641.9	653.5	529.0	47.5	530.8	40.5	532.4	12.0
UCT-18-Cs	641.5	653.2	529.2	55.3	531.0	32.1	532.5	12.6
UCT-18-Na	641.9	653.4	529.3	64.4	531.0	26.8	532.8	8.7
UCT-18-K	641.1	652.4	529.3	62.4	530.2	29.4	532.1	8.7
UCT-18-Ca	641.2	653.4	529.3	48.0	531.1	31.0	532.7	21.0
UCT-18-Mg	641.3	652.7	529.3	57.7	530.1	32.9	532.5	9.3

O_s: Structural or lattice oxygen, O_{ads}: Adsorbed oxygen on the surface, O_{mw}: Adsorbed water and hydroxyl group.

2.5 Catalytic Reactions

2.5.1 Catalyst Screening

The oxidation of benzyl alcohol was selected as a model reaction to evaluate the catalytic performances of ion promoted mesoporous manganese oxides. We used UCT-18-K as the model catalyst. Apart from the nominal Mn/cation (100/1, mol/mol) ratio, the UCT-18-K was also synthesized with different Mn/K molar ratios (50/1, 20/1 and 10/1). The Mn/K molar ratio 10/1 did not give any clear reaction gel, as surfactant became insoluble and precipitated. The benzyl alcohol oxidation was done by UCT-18-K with different Mn/K molar ratios (**Figure 2.7**). The Mn/K molar ratio 100/1 was found to be the optimum. After having the superior catalytic activity of K+ promoted manganese oxide (UCT-18-K) over

nonpromoted and other K+ promoted manganese oxide (UCT-1, K-OMS-2), other promoted oxide with different alkali metal cations (UCT-18-Mg, UCT-18-Ca, UCT-18-Na, UCT-18-Cs) were prepared. Selective aerobic oxidation of structurally different alcohols was performed to evaluate the catalytic performance of mesoporous UCT-1 and UCT-18 materials. **Figure 2.8** describes the increase of activity with the addition of metal ions for 4 different alcohols. There is a trend of increasing activity observed in the following order UCT-1 <UCT-18-Mg <UCT-18-Ca <UCT-18-K <UCT-18-Na <UCT-18-Cs. This trend in activity is related to both the size and charge of the ions in manganese oxide (the bigger the ratio, higher the catalytic activity). The observed trend suggests that the promoted materials are always better than nonpromoted ones, and Cs is the best promoter in the reaction.

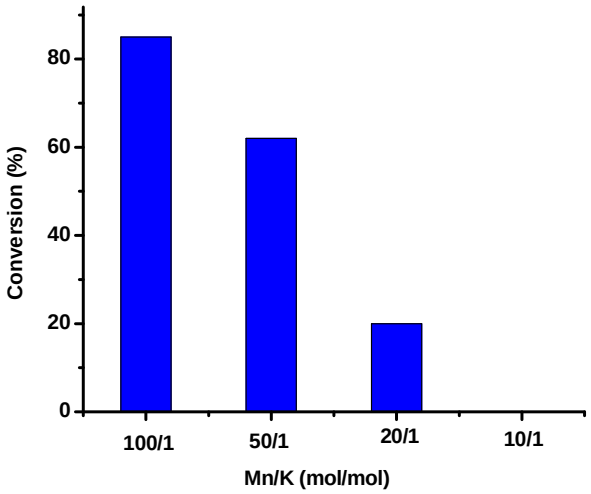

Figure 2.7 Oxidation of benzyl alcohol by UCT-18-K with different Mn/K (mol/mol) nominal ratio. Reaction conditions: benzyl alcohol (1.0 mmol), catalyst (50 mg), toluene (15 mL), 85°C, air flow, 2 h.

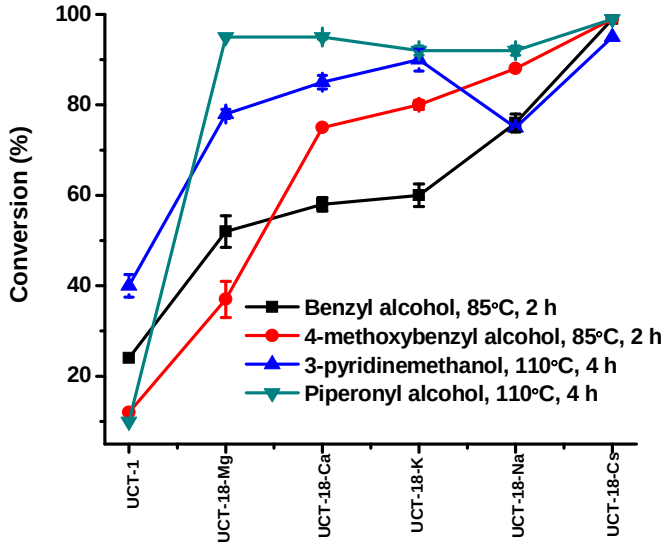

Figure 2.8 The oxidation of alcohols by UCT-1 and UCT-18. Reaction Conditions: alcohols (1.0 mmol), toluene (15 mL), catalyst (50 mg), air flow, 85°C/ 110°C, 2 h/4 h.

2.5.2 Oxidation of Alcohols

The UCT-18-Cs (as the most active promoted UCT-18) and non-promoted UCT-1 were selected for the further testing of oxidations of structurally different alcohols. **Table 2.3** summarizes the oxidation of 12 different alcohols catalyzed by the UCT-18-Cs and UCT-1. The UCT-18-Cs catalyst showed significantly higher activity for the conversion of all the alcohols to aldehydes or ketones as compared to UCT-1. UCT-18-Cs can oxidize various types of structurally different alcohols with almost 100% conversions. UCT-18-Cs can oxidize aromatic **[Entry 1-11, Table 2.3]**, aliphatic **[Entry 12, Table 2.3]**, primary **[Entry 1-8, Table 2.3]** and secondary **[Entry 9, Table 2.3]** alcohols selectively into the corresponding carbonyl compounds. For a long chain aliphatic alcohol **[Entry 12, Table 2.3]** the conversion was less, and longer reaction time was required. The alcohols containing S and N as heteroatoms **[Entry 7, 8, Table 2.3]** were converted to the

corresponding aldehydes selectively. In the case of oxidation of piperonyl alcohol **[Entry 6, Table 2.3]** to piperonyl aldehyde, the UCT-18-Cs had ten times better conversion than UCT-1. The UCT-18-Cs can convert 1,3-Benzenedimethanol chemoselectively (92% selectivity) to monoaldehyde with 93% conversion **[Entry 11, Table 2.3]**.

Table 2.3 Aerobic selective oxidation of different alcohols by UCT-1 and UCT-18-Cs[a]

Entry	Substrate	Product	Time (h)	Catalyst	Conversion[b,c] (%)
1	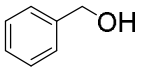	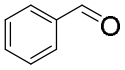	2[d]	UCT 1	24
				UCT-18-Cs	>99
2	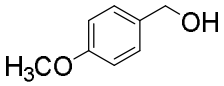	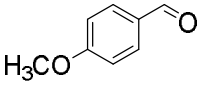	2[d]	UCT 1	12
				UCT-18-Cs	>99
3	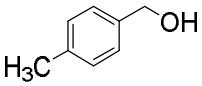	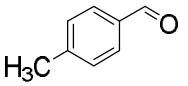	2[d]	UCT 1	30
				UCT-18-Cs	>99
4	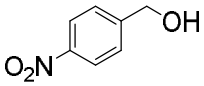	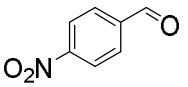	2	UCT 1	85
				UCT-18-Cs	>99
5	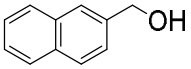	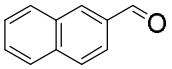	2	UCT 1	45
				UCT-18-Cs	>99
6	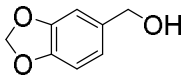	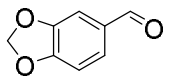	4	UCT 1	10
				UCT-18-Cs	>99
7	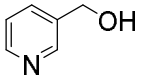	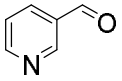	2	UCT 1	40
				UCT-18-Cs	95
8	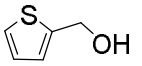	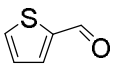	2	UCT 1	70
				UCT-18-Cs	92
9	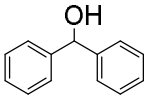	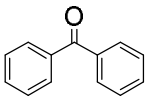	2	UCT 1	30
				UCT-18-Cs	>99
10	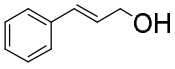	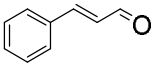	15	UCT 1	8
				UCT-18-Cs	50
11	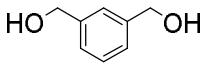	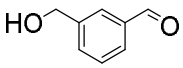	6	UCT 1	80
				UCT-18-Cs[e]	93
12	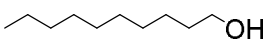	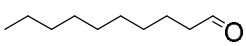	15	UCT 1	3
				UCT-18-Cs	30

[a] Reaction Conditions: alcohols (1.0 mmol), toluene (15 mL), catalyst (50 mg), 110°C, under air flow. [b] Determined by GC-MS [c] Selectivity was 100%, no products other than aldehyde and ketone were found. [d] Reactions were performed at 85°C. [e] Selectivity was 92%, the other product was di-aldehyde for UCT-18-Cs.

2.5.3 The oxidation of 1,3,5-trimethylbenzene (C-H activation)

The UCT-18-Cs was investigated further for the activation of relatively inert C-H bond. 1,3,5-Trimethylbenzene (mesitylene) was used as substrate. The UCT-18-Cs successfully oxidized 1,3,5-trimethylbenzene to 3,5-dimethylbenzoic acid with a very high conversion (99%) and selectivity (90%) under aerobic and solvent free conditions (**Table 2.4**). Similar to oxidation of alcohols, the UCT-18-Cs (99% conversion) demonstrate enhanced catalytic performance over UCT-1 (52% conversion) **[Entry 4, Table 2.4]** under similar conditions. The UCT-18-Cs also exhibits a high conversions (95%) and selectivity (~90%) with different scale of reactants **[Entry 2-3, Table 2.4].** The oxidation of 1,3,5-trimethylbenzene also produced (3,5-dimethylphenyl)methyl ester (~10% selectivity) via cross-dehydrogenative coupling.

Table 2.4 Aerobic oxidation and cross dehydrogenative coupling of 1,3,5-timethylbenzene[a]

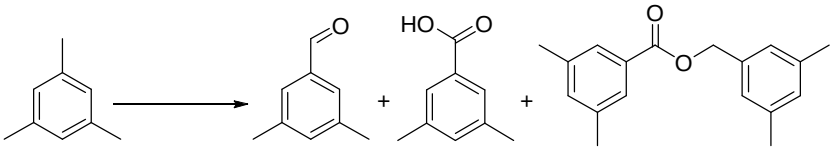

Entry	Catalyst	Amount (mL)	Time (h)	Conversion[b] (%)	Selectivity[c] (%)		
					Aldehyde	Acid	Ester
1	UCT-18-Cs	5 (35 mmol)	36	95	nd	88	12
2	UCT-18-Cs	10 (70 mmol)	40	99	1	90	9
3	UCT-18-Cs	25 (175 mmol)	72	91	nd	91	9
4	UCT-1	10 (70 mmol)	40	52	7	69	24

[a] Reaction Conditions: 1,3,5-trimethylbenzene (required amount in mL), catalyst (100 mg), 130°C, air flow. [b] Dtermined by GC-MS. [c] Selectivity (%) of product = [(concentration of product) × (total concentration of all products)$^{-1}$] ×100. nd = not detected (<1%).

2.6 Discussion

In the synthesis of UCT-18, Mn precursors, along with the other ionic sources, were confined in inverse surfactant (P123) micelles, which were then packed to form mesoporous materials. The uncontrolled aggregation of oxo-clusters was prevented by surfactant molecules in the reverse micelles and the interface modifier (1-butanol). The hydrotropic nitrate ion increased the solubility of the surfactants by decreasing the aggregation number. The nitrate ions penetrated into the micelles to hydrate it and pulled the positively charged oxo clusters into the micelles [16]. The reaction was driven by evaporation of the solvent at 120°C and thermal NOx formation (from the nitrate ion) to control the sol-gel chemistry of Mn sols. The surfactants in the resulting materials were washed off with ethanol (solvent extraction). The mesopores were formed by connected inter-particle voids. The chemisorbed nitric oxides and carboxylates were removed from the structure by heating the material at 150°C for 12 h and 250°C for 3 h under air [17].

Despite the promoter ions being mentioned several times in the literature, their major role in catalytic reactions is still unclear [18-21]. A trend of increasing catalytic activity with the increasing size/charge ratio of promoter cations has not been previously observed. One possible explanation concerning the role of promoter ions in the enhanced catalytic activity is the alteration of the surface basicity. Alkali metal ions on the surface of the oxides are known to increase the basicity of the material due to their electropositive nature[22]. The basic sites can be considered either as defects in the material or as enhanced electron density of the framework oxygen due to the presence of electropositive cations [23]. The effect of surface Cs^+ ions can cause the binding energy of lattice oxygen to decrease in energy as discussed by Santos et al. which also correlates with the increase of surface

basicity [24]. The presence of basic sites on the manganese oxide materials promote the dehydration step by aiding the deprotonation of the alcohol, which is an important step for partial oxidation [25]. The basicity of the materials also promotes the oxidation of alkylbenzenes [26]. Therefore, increasing the basicity of mesoporous manganese oxide by incorporation of alkali metal ions can enhance the catalytic activity for oxidation and esterification. In this work trace amounts of alkali metal ions (Mn/ion, >1000/1) were incorporated in the manganese oxide materials. However, the ions caused a remarkable increase in the catalytic activity towards oxidative transformations.

There is a trend of increasing basicity for the promoted materials (as revealed from CO_2 adsorption), which was correlated with the size/charge ratio of the cations. Like the trend observed for the oxidation of different alcohols, a similar trend was observed for the basicity of the materials, with Cs promoted material being the most basic. Therefore, the basicity of the promoted materials plays an important role in the higher activity in oxidation of alcohols and alkylbenzenes. Despite the fact that adding base in the reaction can increase the activity in oxidation in many systems, an efficient oxidation process should not involve any additives such as base or acid [27]. The bifuctional nature (redox and basic) of UCT-18-Cs can enhance the oxidation activity without any additional base.

The activity enhancement can be linked to the ease of reducibility of the materials. The low reduction temperatures of promoted UCT-18-Cs (280°C, 420°C in UCT-1 and 260°C, 400°C in UCT-18-Cs), as observed in H_2-TPR studies indicate an increase of mobility and accessibility of lattice oxygen. The presence of Cs^+ can cause a more facile supply of lattice oxygen, which can create defects in the materials [24]. The defects can promote the adsorption of the substrate, since high adsorption capacity of the mesoporous

materials is a well-established property [28]. The effect of lattice oxygen is more prominent as observed in the O_2-TPD studies. The UCT-1 and UCT-18-Cs evolve lattice oxygen at around 532°C and 570°C respectively. Though these materials are amorphous in nature they still have some crystallinity with a framework structure as observed in HR-TEM images. So the term lattice (or bulk) oxygen can be used for the amorphous UCT-1 and UCT-18-Cs materials. The involvement of lattice oxygen in the catalytic activity suggests that the reaction goes through the Mars-Van-Krevelen mechanism [29-32]. The Mn^{3+} species can disproportionate to Mn^{2+} and Mn^{4+} species under oxidative conditions [33]. The adsorbed alcohol molecules get oxidized with multi-electron transfer between the Mn centers (**Scheme 2.1**). The reduced Mn species, however, can get oxidized by labile lattice oxygen with creation of oxygen vacancies. The resulting oxygen vacancies are finally replenished by gas phase oxygen molecules. The presence of three different oxygen species in different binding environments was established by XPS studies. The areas of O_s peaks (structural or lattice oxygen) in all the promoted UCT-18 materials are relatively higher than nonpromoted UCT-1. Therefore, the easily reducible best promoted UCT-18-Cs evolve more labile lattice oxygen readily by creating active sites, which is related to the enhanced catalytic activity.

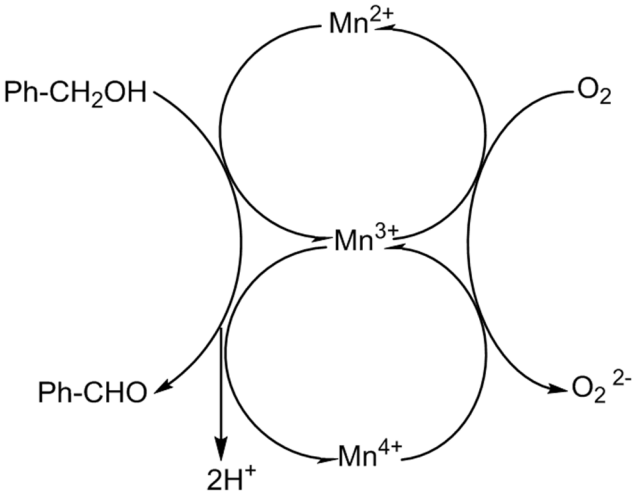

Scheme 2.1 Proposed alcohol oxidation mechanism over UCT-18-Cs.

Selective oxidation of several different alcohols were performed by nonpromoted (UCT-1) and promoted (UCT-18) mesoporous manganese oxides. The activity followed the series of cations according to the size/charge ratio, UCT-1 <UCT-18-Mg <UCT-18-Ca <UCT-18-K <UCT-18-Na <UCT-18-Cs. Among the promoted oxides, the Cs promoted one performed best. The Cs promoted material (UCT-18-Cs) was then used for oxidation of 12 different alcohols to the corresponding aldehydes and ketones. The reaction exhibited very high conversion (> 99% in most cases) in most cases under mild aerobic conditions. Only in the case of big and inactive 1-decanol [**Entry 12, Table 2]** the conversion was less. This may be due to the limitation of molecular transportation in the mesopores of the catalyst. Transition metal oxide based catalysts are notorious for not being ideal of heterogeneous catalysts for the selective oxidation of alcohols containing heteroatoms (i.e. S and N), because the strong coordination of the heteroatom with the metal center results in deactivation of the catalyst [34]. However, UCT-18-Cs successfully and selectively catalyzed the oxidation of alcohols containing S and N as heteroatoms **[Entry 7, 8, Table**

2.2] to the corresponding aldehydes. Moreover the recovered catalyst (UCT-18-Cs) gave conversions similar to the fresh catalysts in the case of oxidation of 2-thiophenemethanol. The catalytic performance of UCT-18-Cs can be restored by simply washing with toluene and methanol and reactivation (250°C for 2 h in air). The reactivation is required to remove adsorbed species from the surface of the catalyst. The first order dependence of rate on alcohol concentration is also an indication of the rate determining step, which could involve adsorption of alcohols or desorption of aldehydes from the active sites of the catalyst surface. The lower activity under N_2 (30% conversion) compared to air (> 99% conversion) is attributed to adsorbed oxygen on the catalyst surface and labile lattice oxygen. These observations also indicate the role of air in the oxidation reaction, as the loss of lattice oxygen should be replenished by the oxygen coming from air [32]. The significantly lower conversion (10% conversion in acetonitrile) in polar solvents is due to competitive binding of polar solvents and the substrate molecules to the active sites of the catalyst [32]. The reaction in acetonitrile (100% selectivity for benzaldehyde; no other products were detected) also rules out the formation of toluene due to a non-oxidative disproportionation reaction of benzyl alcohol [35,36] under the reaction conditions. The oxidation of reaction solvent, toluene (without the substrate) was carried out under identical conditions by UCT-18-Cs to verify if benzaldehyde was formed as a result of oxidation of toluene. The trace amount of benzaldehyde (<1%) formed after 15 h of reaction indicates that UCT-18-Cs selectively catalyzed the oxidation of alcohols under the mentioned reaction conditions. The oxidation of aromatic C-H bonds required prolonged reaction time with higher amounts of catalyst. Moreover, UCT-18-Cs can undergo solvent free green oxidation of 1,3,5-trimethylbenzene to 3,5-dimethylbenzoic acid with very high conversion (> 90%

conversion) and selectivity (90/10, acid/ester). This kind of green oxidation under mild and aerobic conditions has not been observed before. Even in the case of large scale transformation, the catalyst exhibited similar conversions and selectivities, (**Table 3**). The reaction also yielded (3,5-dimethylphenyl)methyl ester along with the acid. The formation of ester is due to cross dehydrogenative coupling (CDC) between 1,3,5-trimethylbenzene or any other intermediates like corresponding alcohols, aldehydes or acids. The typical catalysts used for the cross dehydrogenative coupling are catalysts containing metal centers like Ru, Rh, V, Cu with base additives and TBHP as oxidant [37-40]. The UCT-18-Cs can promote the formation of esters under ambient aerobic and green conditions without the presence of base or expensive oxidants.

2.7 Conclusion

To summarize, the incorporation of trace amounts of alkali metal ions leads us to promoted mesoporous manganese oxides. The cation promoted materials (UCT-18) exhibited regular mesoporosity with pore sizes of 3.4 nm. These catalysts demonstrated other characteristic features of UCT materials (one low angle diffraction line, Type IV isotherm, aggregation of rounded micron size nanoparticles). The cation promoted mesoporous manganese oxides exhibited high catalytic performance for oxidation of alcohols to carbonyl compounds under mild aerobic reaction conditions in the following order UCT-1 <UCT-18-Mg <UCT-18-Ca <UCT-18-K <UCT-18-Na <UCT-18-Cs. The order followed the size/charge ratios of the incorporated cations, which correlates with the increase of relative basicity of the materials. The Cs promoted mesoporous manganese oxide was found to be the most active for the selective alcohol oxidation reactions (> 95%

conversion in most cases, 100% selectivity). The UCT-18-Cs material demonstrated superior catalytic activity in formation of solvent free green oxidation of 1,3,5-trimethylbenzene to 3,5-dimethylbenzoic acid and (3,5-dimethylphenyl)methyl ester with very high conversions (> 90% conversion) and selectivity (90/10, acid/ester). Such kinds of scalable, green and mild aerobic oxidation and cross dehydrogenative coupling of relatively inert C-H bonds are observed for the first time. The enhancement in catalytic activity can be correlated to the bifunctional (redox and basic) nature of the material, which in turn correlates with the promoting effect of ions in the mesoporous manganese oxides. The easily reducible nature with retention of the amorphous phase reflects the involvement of greater amounts of accessible lattice or structural oxygen, which are the other contributing factor for the enhancement of catalytic activity. The use of mild reaction conditions, (use of air as oxidant, ambient pressure), excellent reusability and high activity towards inactive compounds make the UCT-18 (especially UCT-18-Cs) materials environmentally friendly, as well as a new class of oxidation catalysts. The tunable pore size and crystallinity by simple heating cycles make the materials more ubiquitous and this opens a new avenue for the design and application of heterogeneous catalysts.

2.8 References

(1) Vinod, C. P.; Wilson, K.; Lee, A. F. *J. Chem. Technol. Biotechnol.* **2011**, *86*, 161-171.

(2) Schultz, M. J.; Sigman, M. S. *Tetrahedron* **2006**, *62*, 8227-8241.

(3) Mallat, T.; Baiker, A. *Chem. Rev.* **2004**, *104*, 3037-3058.

(4) Shylesh, S.; Schünemann, V.; Thiel, W. R. *Angew. Chem. Int. Ed.* **2010**, *49*, 3428-3459.

(5) Ishii, Y.; Sakaguchi, S.; Iwahama, T. *Adv. Synth. Catal.* **2001**, *343*, 393-427.

(6) Shilov, A. E.; Shul'pin, G. B. *Chem. Rev.* **1997**, *97*, 2879-2932.

(7) Yoshino, Y.; Hayashi, Y.; Iwahama, T.; Sakaguchi, S.; Ishii, Y. *J. Org. Chem.* **1997**, *62*, 6810-6813.

(8) Dick, A. R.; Hull, K. L.; Sanford, M. S. *J. Am. Chem. Soc.* **2004**, *126*, 2300-2301.

(9) Shijina, A. V.; Renuka, N. K. *React. Kinet. Catal. Lett.* **2008**, *94*, 261-270.

(10) Bäckvall, J.-E. *Modern oxidation methods*; John Wiley & Sons, 2011.

(11) Nikalje, M. D.; Sudalai, A. *Tetrahedron* **1999**, *55*, 5903-5908.

(12) Das, T.; Chaudhari, K.; Nandanan, E.; Chandwadkar, A.; Sudalai, A.; Ravindranathan, T.; Sivasanker, S. *Tetrahedron Lett.* **1997**, *38*, 3631-3634.

(13) Bonvin, Y.; Callens, E.; Larrosa, I.; Henderson, D. A.; Oldham, J.; Burton, A. J.; Barrett, A. G. *Org. Lett.* **2005**, *7*, 4549-4552.

(14) Shaikh, T. M. A.; Sudalai, A. *Eur. J. Org. Chem.* **2008**, *2008*, 4877-4880.

(15) Genuino, H. C.; Dharmarathna, S.; Njagi, E. C.; Mei, M. C.; Suib, S. L. *J. Phys. Chem. C* **2012**, *116*, 12066-12078.

(16) Poyraz, A. S.; Dag, O. m. *J. Phys. Chem. C* **2009**, *113*, 18596-18607.

(17) Poyraz, A. S.; Kuo, C.-H.; Biswas, S.; King'ondu, C. K.; Suib, S. L. *Nat. Commun.* **2013**, *4*, 2952.

(18) Arai, M.; Nishiyama, S.; Tsuruya, S.; Masai, M. *J. Chem. Soc., Faraday Trans.* **1996**, *92*, 2631-2636.

(19) Genta, M.; Nishiyama, S.; Tsuruya, S.; Masai, M. *J. Chem. Soc., Faraday Trans.* **1996**, *92*, 1267-1275.

(20) Tang, Q.; Huang, X.; Wu, C.; Zhao, P.; Chen, Y.; Yang, Y. *J. Mol. Catal. A: Chem.* **2009**, *306*, 48-53.

(21) Li, Y.; Nakashima, D.; Ichihashi, Y.; Nishiyama, S.; Tsuruya, S. *Ind. Eng. Chem. Res.* **2004**, *43*, 6021-6026.

(22) Helwani, Z.; Othman, M.; Aziz, N.; Kim, J.; Fernando, W. *Appl. Catal., A: Gen.* **2009**, *363*, 1-10.

(23) Martra, G.; Ocule, R.; Marchese, L.; Centi, G.; Coluccia, S. *Catal. Today* **2002**, *73*, 83-93.

(24) Santos, V.; Pereira, M.; Órfão, J.; Figueiredo, J. *Appl. Catal. B: Environ* **2009**, *88*, 550-556.

(25) Zheng, N.; Stucky, G. D. *Chem. Commun.* **2007**, 3862-3864.

(26) Jana, S. K.; Wu, P.; Tatsumi, T. *J. Catal.* **2006**, *240*, 268-274.

(27) Abad, A.; Concepción, P.; Corma, A.; García, H. *Angew. Chem. Int. Ed.* **2005**, *44*, 4066-4069.

(28) Climent, M.; Velty, A.; Corma, A. *Green Chemistry* **2002**, *4*, 565-569.

(29) Makwana, V. D.; Son, Y.-C.; Howell, A. R.; Suib, S. L. *J. Catal.* **2002**, *210*, 46-52.

(30) Doornkamp, C.; Ponec, V. . *Mol. Catal. A: Chem.* **2000**, *162*, 19-32.

(31) Poyraz, A. S.; Song, W.; Kriz, D.; Kuo, C.-H.; Seraji, M. S. I.; Suib, S. L. *ACS Appl. Mater. Interfaces* **2014**, *6 (14)*, 10986-10991.

(32) Dharmarathna, S.; King'ondu, C. K.; Pahalagedara, L.; Kuo, C.-H.; Zhang, Y.; Suib, S. L. *Appl. Catal., B: Environ.* **2014**, *147*, 124-131.

(33) Takashima, T.; Hashimoto, K.; Nakamura, R. *J. Am. Chem. Soc.* **2012**, *134*, 1519-1527.

(34) Karimi, B.; Biglari, A.; Clark, J. H.; Budarin, V. *Angew. Chem. Int. Ed.* **2007**, *46*, 7210-7213.

(35) Sankar, M.; Nowicka, E.; Tiruvalam, R.; He, Q.; Taylor, S. H.; Kiely, C. J.; Bethell, D.; Knight, D. W.; Hutchings, G. J. *Chem. Eur. J.* **2011**, *17*, 6524-6532.

(36) Meenakshisundaram, S.; Nowicka, E.; Miedziak, P. J.; Brett, G. L.; Jenkins, R. L.; Dimitratos, N.; Taylor, S. H.; Knight, D. W.; Bethell, D.; Hutchings, G. J. *Faraday Discuss.* **2010**, *145*, 341-356.

(37) Majji, G.; Guin, S.; Gogoi, A.; Rout, S. K.; Patel, B. K. *Chem. Commun.* **2013**, *49*, 3031-3033.

(38) Zhang, J.; Leitus, G.; Ben-David, Y.; Milstein, D. *J. Am. Chem. Soc.* **2005**, *127*, 10840-10841.

(39) Liu, C.; Tang, S.; Zheng, L.; Liu, D.; Zhang, H.; Lei, A. *Angew. Chem.* **2012**, *124*, 5760-5764.

(40) Rout, S. K.; Guin, S.; Ghara, K. K.; Banerjee, A.; Patel, B. K. *Org. Lett.* **2012**, *14*, 3982-3985.

CHAPTER 3. Efficient Aerobic Oxidation of Amines to Imines by Cesium Promoted Mesoporous Manganese Oxide

3.1 Abstract

Selective oxidation of amines to imines is one of the most studied reactions in the field of heterogeneous catalysis. Cs ion promoted mesoporous manganese oxide (meso Cs/MnO_x) was synthesized using inverse surfactant micelles as a soft template. The meso-Cs/MnO_x material presented an aggregated nanocrystalline nature with monomodal mesoporous size distributions. The catalyst was found to be effective in oxidation of amines to imines under aerobic conditions. The meso Cs/MnO_x exhibited oxidation of primary, secondary, cyclic, aromatic, and aliphatic amines to imines, where the conversions reached as high as >99%. The catalyst was also effective in oxidative cross condensation of two different amines to produce asymmetrically substituted imines. Surface active Mn^{3+} species along with labile lattice oxygen, were found to play an important role in the catalytic activity. Mild reaction conditions (air atmosphere and absence of any oxidative or basic promoters), ease of product separation by simple filtration and significant reusability make this mesoporous manganese oxide material an economical and ecofriendly catalyst for the syntheses of versatile imine derivatives.

3.2 Introduction

Imines are a class of nitrogen based compounds with high reactivity due to the presence of unsaturated C=N double bonds. Derivatives of imines have versatile uses in the production of heterocyclic chemicals and pharmaceutical compounds[1]. The traditional

approach to imine synthesis involves condensation reaction between amines and carbonyl compounds. The process often requires Lewis acid catalysts, dehydrating agents, activated aldehydes and prolonged reaction time therefore restrain the use of this process practically and environmentally[2,3]. As an alternative approach, the direct oxidation of amines has attracted considerable attention for synthesis of imines. Stoichiometric oxidants such as chromate, permanganate, and 2-iodoxybenzoic acid[4] have been used for the oxidation of amines to imines. However, the use of stoichiometric oxidants has several drawbacks, which are the production of undesirable toxic waste and difficulties in product separation.

Some established heterogeneous catalytic systems for the oxidation of amines to imines include precious metal based catalysts such as palladium, gold[5-8], other systems like ruthenium[9,10], graphene oxide[11], metal organic frameworks[12], α-MnO_2[13], copper[14] and photocatalysts like TiO_2[15,16], $BiVO_4$[17] and Nb_2O_5[18]. In spite of good yields and selectivity, all of the catalysts either have cumbersome preparation methods or require the use of harsh reaction conditions such as high pressure, light irradiation, and use of oxidative promoters[19]. Moreover, limited activity of aliphatic amines with undesired side reactions is another flaw for the reported systems. Despite good activity in the syntheses of symmetrical imines, syntheses of asymmetrically substituted imines by cross condensation of two amines have barely been discussed. Therefore, design of an effective heterogeneous catalyst system for the oxidation of amines is desirable, which ideally involves mild aerobic atmospheric conditions, high TOF, avoidance of any additives, high reusability, and activity towards syntheses of symmetrical and asymmetrical substituted imines.

Herein, we report the aerobic oxidation of amines to imines and oxidative cross condensation of two different amines (benzylamine and other aromatic and aliphatic

amines) with mesoporous Cs promoted manganese oxide material (meso Cs/MnO_x). Use of air as the sole oxidant, ambient reaction conditions, high yields of imines, and absence of additives make this process superior over other heterogeneous catalytic systems. The mechanistic pathways and kinetic analysis were also studied in detail. This is the first example of additive free and non-photochemical heterogeneous catalytic system for synthesizing symmetrical and asymmetrical imines from diverse amines under aerobic atmospheric conditions.

3.3 Experimental Section

3.3.1 Synthesis of mesoporous Cs/MnO_x

In a typical synthesis 0.02 mol of manganese nitrate tetrahydrate ($Mn(NO_3)_2 \cdot 4H_2O$) and 0.134 mol of 1-butanol were added into a 120 mL beaker. To this solution 0.00034 mol of poly(ethyleneglycol)-block-poly(propyleneglycol)-block-poly(ethylene glycol) (Pluoronic P123, $PEO_{20}PPO_{70}PEO_{20}$, molar mass 5750 g mol^{-1}) and 0.032 mol of concentrated nitric acid (HNO_3) were added and stirred at room temperature until the solution became clear (light pink). To this clear solution 200 µL of 1.0 M cesium nitrate ($CsNO_3$) aqueous solution was added maintaining the Mn/Cs molar ratio of 100/1. The resulting clear solution was then kept in an oven at 120°C for 3 h under air. The black product was collected and washed with excess ethanol, centrifuged, and dried in a vacuum oven at room temperature overnight. At the end, the dried black powders were subjected to a heating cycle. First they were heated at 150°C for 12 h and cooled to room temperature under ambient conditions followed by a second heating step of 250°C for 3 h. Mesoporous MnO_x was synthesized by the same procedure without adding any $CsNO_3$ solution.

3.3.2 Catalyst Characterization

Powder X-Ray diffraction (PXRD) measurements were performed on a Rigaku Ultima IV diffractometer (Cu Kα radiation, λ=1.5406 Å) with an operating voltage of 40 kV and a current of 44 mA. The low-angle PXRD pattern was collected over a 2 theta range of 0.5–8° with a continuous scan rate of 0.5° min^{-1}, where the wide-angle PXRD pattern was collected over a 2 theta range of 5–75° with a continuous scan rate of 2.0° min^{-1}. Nitrogen sorption experiments were performed by a Quantachrome Autosorb-1-1C automated adsorption system. The material was degassed at 150°C for 5 h (ramp rate 10°C / min) under helium prior to measurement. The surface area was calculated using the Brunauer–Emmett–Teller (BET) method, and the Barrett–Joyner–Halenda (BJH) method was utilized to calculate the pore sizes and pore volume from the desorption branch of the isotherm. The surface morphology was determined with a Zeiss DSM 982 Gemini field emission scanning electron microscope (FE-SEM) with a Schottky emitter at an accelerating voltage of 2.0 kV having a beam current of 1.0 mA. High-resolution transmission electron microscopy (HR-TEM) experiments were carried out on a JEOL 2010 FasTEM microscope at an operating voltage of 200 kV. The samples were prepared by casting the suspension of material on a carbon coated copper grid. X-ray photoelectron spectroscopy (XPS) was done on a PHI model 590 spectrometer with multiprobes (ΦPhysical Electronics Industries Inc.), using Al-K radiation (λ= 1486.6 eV) as the radiation source and was fitted using CasaXPS software (version 2.3.12). The powder samples were pressed on carbon tape mounted on adhesive copper tape stuck to a sample stage placed in the analysis chamber. For correction of surface charging, the C 1s photoelectron line at 284.6 eV was taken as a reference. A mixture of Gaussian (70%) and Lorentzian (30%) functions was used for the

least-squares curve fitting procedure. The temperature programmed desorption (TPD) experiments were performed with a Thermolyne 79300 model tube furnace equipped with an MKS gas analyzer coupled with a quadrupole mass selective detector. The samples were treated with Ar for 2 h at 250°C before the experiment. Ar was used as a carrier gas in the experiments at a constant flow rate in the temperature range 50°C to 600°C at a ramp of 10°C min^{-1}. The amount of Cs in the material was determined with a Perkin Elmer/DRC-e inductively coupled plasma mass spectrometer (ICP-MS) CETAC laser ablation unit, whereas Perkin Elmer Optima 7300DV inductively coupled plasma optical emission spectrometer (ICP-OES) was used to determine the Mn concentration.

3.3.3 Catalytic Activity Measurements

3.3.3.1 Oxidation of amines to imines:

In a typical amine oxidation reaction, a mixture of amine (0.5 mmol), catalyst (25 mg) and toluene (5 mL) was added in a 25 mL round bottom flask equipped with a condenser. The reaction mixture was heated to reflux under vigorous stirring (700 rpm) for the required time under an air balloon. After reaction, the mixture was cooled, and the catalyst was removed by filtration. The product analysis was done using GC-MS (gas chromatography-mass spectrometry). The conversion was determined based on the concentration of amines. Most reactions were repeated twice and the average values were used.

Pure imines were obtained by washing and evaporation of the solvent. The reaction was cooled to room temperature after completion (having negligible amount of aldehydes and cyanides along with imines). The catalyst was removed by centrifugation and washed

several times with toluene. The filtrate was collected and kept for evaporation of solvent and finally dried under vacuum. The imine products were identified by the ^{1}H NMR and ^{13}C NMR spectra.

3.3.3.2 Cross-coupling of amines: In a typical cross-coupling reaction, a mixture (1/3 molar ratio) of benzylamine and other aliphatic and aromatic amines (Table 3), catalyst (25 mg) and toluene (5 mL) were put in a 25 mL round bottom flask equipped with a condenser. The reaction mixture was heated to reflux with vigorous stirring (700 rpm) for the required time under an air balloon. After reaction, the mixture was cooled, the catalyst was removed by filtration, and GC-MS was used to analyze the filtrate. The conversion was determined based on concentration of benzylamine (limiting reactant). The selectivity was calculated based on the self and cross products of benzylamine.

3.3.3.3 Analysis of reaction products

The GC-MS analyses were performed by a 7820A GC system connected with a mass detector of 5975 series MSD from Agilent Technologies, and a nonpolar cross-linked methyl siloxane column with dimensions of 12 in × 0.200 mm × 0.33 µm was used. The ^{1}H and ^{13}C NMR spectra were recorded on a Bruker AVANCE III- 400 MHz spectrometer. ^{1}H NMR spectra were collected at 400 MHz with chemical shift referenced to the residual peak in $CDCl_3$ (δ: H 7.26 ppm). ^{13}C NMR spectra were collected at 100 MHz and referenced to residual peak in $CDCl_3$ (δ: C 77.0 ppm). Multiplicities are written as s (singlet), d (doublet), t (triplet), and m (multiplet).

3.4 Structural characterization of Meso Cs/MnO_x

The physicochemical and morphological features of the material were characterized extensively by powder X-ray diffraction (PXRD), N_2 sorption, scanning electron microscopy (SEM), transmission electron microscopy (TEM), X-ray photoelectron spectroscopy (XPS), temperature programmed desorption (TPD) and inductive coupled plasma (ICP) techniques. The PXRD pattern (**Figure 3.1A**) at low angle region (0.5° to 8°) displayed a single peak, which represented the irregular porous nature of the materials. No distinct diffraction pattern was observed in the wide angle (5° - 75°) range (**Figure 3.1B**), which indicated the poorly crystalline nature of the material. The mesoporosity of the material was confirmed by N_2 sorption experiments (**Figure 3.1C**), where a Type IV adsorption isotherm followed by a Type I hysteresis loop was observed. Pore size of meso Cs/MnOx was calculated as 3.4 nm by the BJH method (**Figure 3.1D**) from the desorption branch of the isotherm, whereas the surface area was 79 $m^2\ g^{-1}$. SEM images (**Figure 3.2**) showed that aggregated nanoparticles formed quasi-spherical micron sized morphology. TEM image (**Figure 3.3A**) also revealed the random packing of nano-oxide particles. Unlike PXRD, the high resolution TEM (Figure **3.3B**) indicated the crystalline nature of the material. The lattice fringes were calculated as 0.27 nm, which can be correlated to the (222) plane of Mn_2O_3 (bixbyite) phase, which was in agreement with the literature findings[20]. The poorly crystalline nature of the material can be the reason for absence of any diffraction peaks under PXRD.

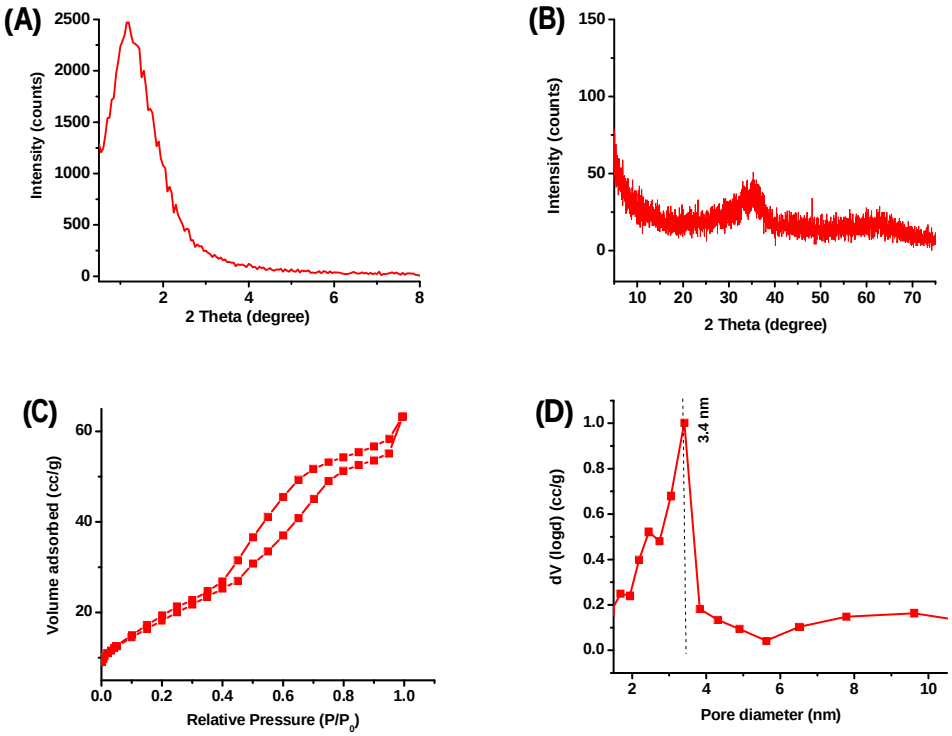

Figure 3.1 Structural characterization of meso Cs/MnO_x. PXRD patterns (A) Low angle (0.5° -8°), (B) Wide angle (5°-75°), (C) N_2 sorption isotherm and (D) BJH desorption pore size distribution.

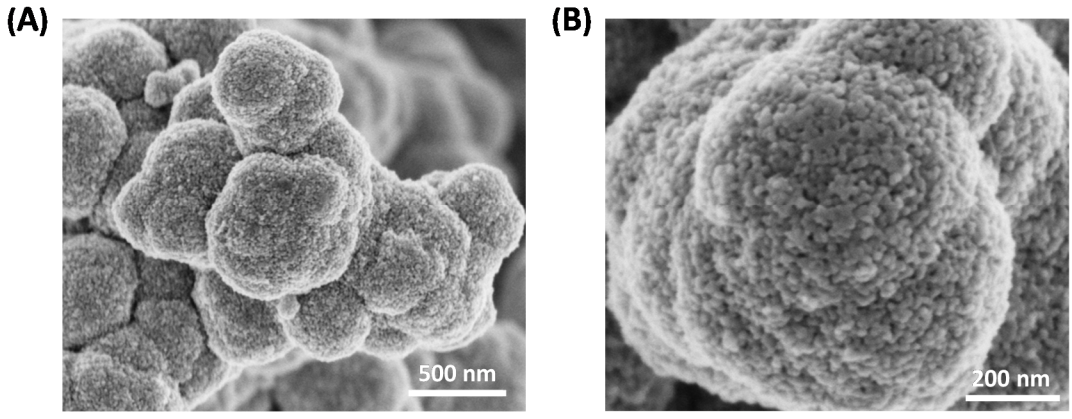

Figure 3.2 SEM images of meso Cs/MnO_x at (A) low and (B) higher magnifications.

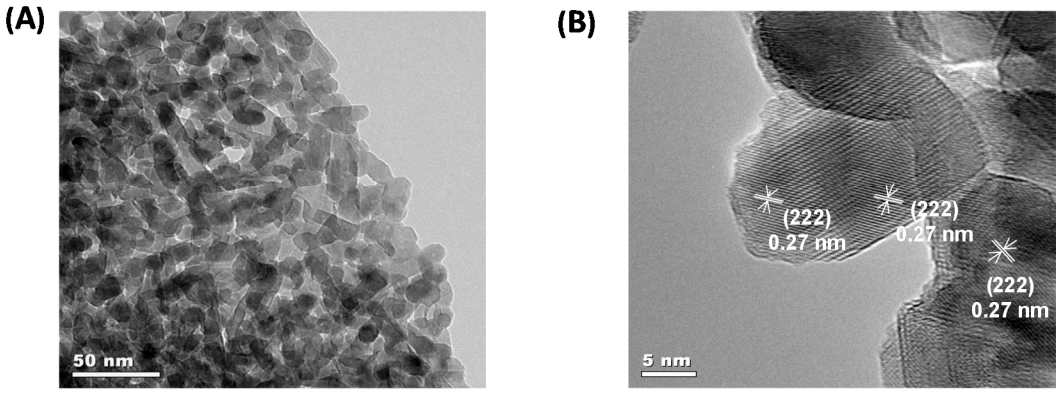

Figure 3.3 TEM images of meso Cs/MnO_x at (A) low and (B) higher magnification. The measured lattice distances of 0.27 nm can be indexed to bixbyite Mn_2O_3 (222) planes.

The Mn 2p XPS spectra in **Figure 3.4B** consist of two peaks, which were assigned as Mn $2p_{3/2}$ and Mn $2p_{1/2}$ core levels. The binding energies of 641.5 eV and 653.5 eV can be attributed to the Mn^{3+} oxidation state[20,21]. The O 1s spectra (**Figure 3.4A**) showed a broad peak of binding energy in the range of ~ 527 to 536 eV, indicating the presence of multiple oxygen species. Deconvolution of O 1s spectra (**Figure 3.4A**) specified the existence of three different binding oxygen species, namely, structural or lattice oxygen (O_s), surface adsorbed oxygen (O_{ads}) and adsorbed water or hydroxyl group (O_{mw})[21]. The relative amount of structural oxygen (O_s) was higher than the other type of oxygen species. O_2-TPD data under a stream of Ar gas are shown in **Figure 3.5**. In general, desorption of surface adsorbed oxygen species and labile lattice oxygen species with different Mn-O bond strengths cause the appearance of peaks in the O_2-TPD profile. A major loss of O_2 from the meso Cs/MnO_x material was observed at 570°C, which can be ascribed to the evolution of lattice oxygen from the manganese oxide[22]. ICP-MS was employed to verify the amount of Cs in the material. A very low concentration of Cs (Mn/Cs molar ratio was

604/1), quite different than the nominal ratio (100/1), was detected. Excess ions were probably removed by washing.

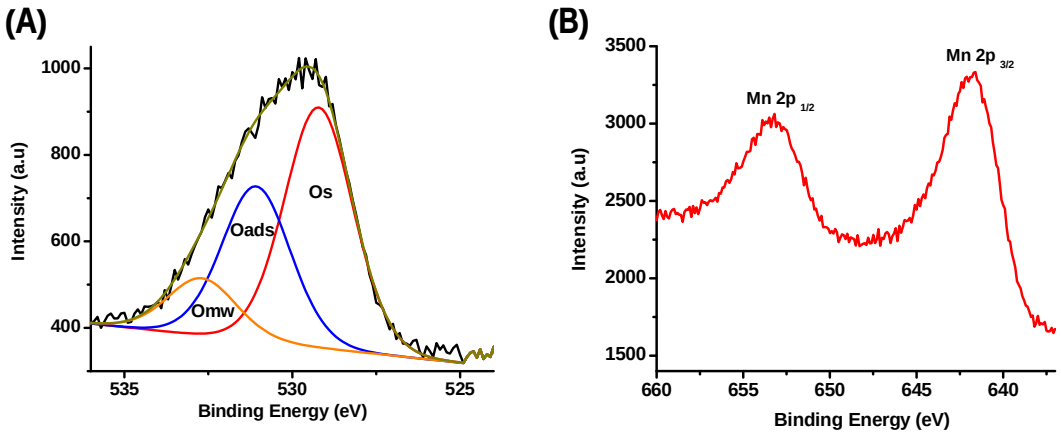

Figure 3.4. XPS of meso Cs/MnO_x. (A) Deconvoluted O1S spectra. Three different oxygen species were identified: Structural or lattice oxygen (O_s), surface adsorbed oxygen (O_{ads}) and adsorbed water or hydroxyl group (O_{mw}) and (B) Mn 2p spectra. The binding energy values fall in the binding energy of the Mn^{3+} oxidation state.

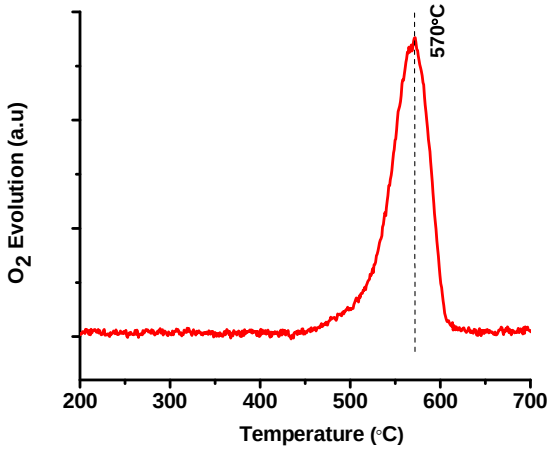

Figure 3.5 O_2-TPD of meso Cs/MnO_x. The peak around 570°C can be ascribed as the lattice or structural oxygen desorption from the material.

3.5 Catalytic reaction

3.5.1 Optimization of reaction conditions

Initially, we have selected the oxidative coupling of 4-methoxybenzylamine as a model reaction for developing the optimal reaction conditions. First, the reactions were performed in solvents of different polarity at their respective boiling points (**Entry 1-4, Table 3.1**). Toluene (the one with highest boiling point, 110°C) gave the highest conversion (>99%) (**Entry 4, Table 3.1**) and selectivity of 80% towards the imine, among the tested solvents and was selected for further studies. The imine formation reaction generally is initiated by the oxidative dehydrogenation of amines to form the RCH=NH intermediate followed by reacting with water to form aldehyde. The intermediate aldehyde was then condensed with the amines to form the target imine molecules. Aldehyde and cyanide as side products were observed in our system. Since the formation of side products is favored at high temperatures, the reaction was performed at relatively lower temperature (80°C). In spite of high selectivity of imine (>99%) achieved at 80°C, conversion decreased significantly to 45% (**Entry 5, Table 3.1**). Furthermore, the variation of selectivity for imine with catalyst loading was established for meso Cs/MnO_x (**Entry 5-7, Table 3.1**). While no significant changes in conversion and selectivity were observed with the catalyst loading of 100 mg (**Entry 6, Table 3.1**), decreasing the catalyst amount to 25 mg was found to be sufficient to drive the reaction towards a quantitative conversion (>99%) and high selectivity (96%) (**Entry 7, Table 3.1**). The reaction was completed in 5 h in aerobic atmospheric conditions without use of any additives. When pure oxygen was used instead of air as oxidant (**Entry 8, Table 3.1**), the reaction was completed even at shorter times. A

significant decrease of conversion (53%) was observed under a nitrogen atmosphere in 8 h (**Entry 9, Table 3.1**).

Table 3.1 Optimization of oxidative coupling of 4-methoxy benzyl amine[a]

Entry	Solvent	Temp. (°C)	Time (h)	Oxidant	Conversion[b] (%)	Selectivity[c] (%)	TOF[d]
1	Methanol	60	8	Air	50	94	0.097
2	Dioxane	100	8	Air	55	100	0.107
3	Hexane	66	8	Air	44	100	0.086
4	Toluene	110	8	Air	100	80	0.195
5	Toluene	80	8	Air	45	100	0.088
6[e]	Toluene	110	8	Air	100	85	0.099
7[f]	Toluene	110	5	Air	100	96	0.625
8[f]	Toluene	110	3	O_2	90	100	1.041
9[f]	Toluene	110	8	N_2	53	100	0.207

[a] Reaction conditions: 4-methoxy benzyl amine (0.5 mmol), meso Cs/MnO_x (50 mg), solvent (5 mL), air balloon, 3-5 h. [b] Conversions were determined by GC-MS based on concentration of amines. [c] The other products were aldehyde and cyanide. [d]TOF = TON . time (h) $^{-1}$, TON = moles of amine converted per mole of catalyst. nd = not determined by GC-MS. [e] 100 mg catalyst. [f] 25 mg catalyst.

3.5.2 Comparison with different catalysts

We then compared the activity with the well-established manganse oxide based catalysts. Very low conversion (10%) was achieved in the absence of any catalyst in 8 h (**Entry 7, Table 3.2**). No improvement of conversion was observed using commercial nonporous Mn_2O_3 indicating total inactivity under the present condition (**Entry 6, Table 3.2**). Using potassium containing manganese oxide octahedral molecular sieves (K-OMS-2[23]) selectivity for imines decreased drastically to 42% with formation a of high

concentration of cyanide and aldehyde products. Other manganese oxide based catalysts like amorphous manganese oxide and birnessite were also tested under the present reaction conditions (**Entry 4-5, Table 3.2**). Meso MnO_x without Cs promoter resulted in similar (>99%) conversion (**Entry 2, Table 3.2**) but much lower selectivity (78%) compared to meso Cs/MnO_x (96% selectivity).

Table 3.2. The catalytic results using different catalysts[a]

Entry	Catalyst	Time (h)	Conversion[b] (%)	Selectivity [c](%)	TON[d]
1	Meso Cs/MnOx	5	100	96	3.33
2	Meso MnOx	5	100	78	3.33
3	K-OMS-2[e]	5	100	42	0.87
4	Amorphous manganese oxide [e]	5	100	57	0.87
5	Birnessite [e]	8	94	96	0.82
6	C-Mn_2O_3	8	10	100	n/a
7	no	8	10	100	n/a

[a] Reaction conditions: 4-methoxy benzyl amine (0.5 mmol), catalyst (25 mg), solvent (5 mL), air balloon, 5-8 h. [b] Conversions were determined by GC-MS based on concentration of amines. [c] The side products were aldehyde and cyanide. [d]TON = moles of amines converted per mole of catalyst. [e] Catalyst: 50 mg.

In order to determine the role of Cs in the present amine oxidation catalytic system, a series of experiments were performed by changing the Cs loading in the material. The aerobic oxidation of a relatively inert secondary amine (1,2,3,4-tetrahydroisoquinoline) was selected as the model reaction. The nonpromoted meso MnO_x material exhibited only 12 % conversion (Entry 1, Table S3) after 1 h, whereas 87 -95% conversions (**Entry 2-4, Table 3.3**) were achieved by Cs incorporation. The meso Cs/MnO_x material with the

highest Cs loading (0.16%) gave maximum conversion (94%) under identical reaction conditions (**Entry 4, Table 3.3**).

Table 3.3 Oxidation of 1,2,3,4-tetrahydroisoquinoline by meso Cs/MnOx with different Cs loading[a]

Entry	Catalyst	Mn/Cs[b] (nominal)	Mn/Cs[b] (ICP)	Conversion[c] (%)	Selectivity [c](%)
1	Meso MnOx[d]	0	0	12	96
2	Meso Cs/MnOx	200/1	1767/1	87	96
3	Meso Cs/MnOx	150/1	1536/1	92	96
4	Meso Cs/MnOx	100/1	604/1	94	96

[a] Reaction conditions: 1,2,3,4-tetrahydroisoquinoline (0.5 mmol), catalyst (50 mg), solvent (5 mL), air balloon, 1 h. [b] Referred to molar ratio. [c] Determined by GC-MS. [d] 75% conversion after 24 h.

3.5.3 Reusability and heterogeneity

The reusability test was conducted for the oxidation of 4-methoxybenzylamine. At the end of the reaction, the catalyst was removed by filtration, washed with excess ethanol and reactivated at 250°C for 45 min prior to reuse. The catalyst retained activity and selectivity even after the fourth cycle (**Figure 3.6**). PXRD analyses of asynthesized and the recovered catalysts indicated that the amorphous nature of the catalyst was preserved (**Figure 3.6**). The hot filtration test was also carried out to verify any possible leaching of active species from the catalyst surface. No further consumption of amine took place after filtering off the catalyst at 47% conversion. Moreover, a very minute change of Cs amount (0.04%) was observed in the meso Cs/MnO_x after the reaction by ICP-MS. All of these results signified the truly heterogeneous nature of meso Cs/MnO_x, which was not only active but also had sustainability and recyclability.

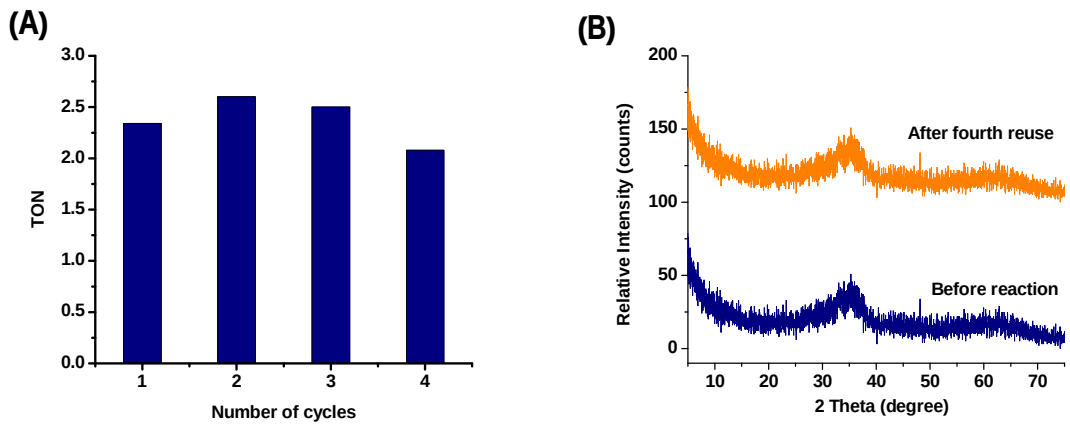

Figure 3.6 (A) Reusability test of the catalyst. Reaction condition: 4-methoxybenzylamine (0.5 mmol), catalyst (15 mg), solvent (5 mL), 110°C, air balloon, 4 h. Turnover number (TON) = [reacted mol amine]/[total mol catalyst]. (B) PXRD of meso Cs/MnOx before and after fourth reuse. The diffraction patterns without noticeable change were observed after fourth reuse.

3.5.4 Oxidation of amines to imines

3.5.4.1 Substrate scope and functional group tolerability

The results of catalytic oxidations of various amines, including aromatic, aliphatic, primary and secondary amine derivatives are listed in Table 3.4. The isolated yield of some of the imines are given in Table 2 (see values in parenthesis). Meso Cs/MnO_x was able to oxidize aromatic (**Entry 1 - 9, Table 3.4**), aliphatic (**Entry 10, Table 3.4**), primary (**Entry 1 - 7, Table 3.4**), secondary (**Entry 8-9, Table 3.4**) and cyclic (**Entry 9, Table 3.4**) amines to the corresponding imines with excellent conversion and selectivity. No dehalogenated product was detected in case of amines with halogen substitution (**Entry 4 - 5, Table 3.4**). An amine containing S as a heteroatom was converted to the imine effectively (**Entry 6, Table 3.4**). The catalyst was also useful for oxidation of the relatively bulky biphenyl (1-napthylmethylamine) system (**Entry 7, Table 3.4**). In the case of oxidation of a secondary amine (**Entry 8, Table 3.4**), conversion was less and much longer reaction time

Table 3.4 Aerobic oxidation of amines to imines by meso Cs/MnO_x[a]

Entry	Substrate	Time (h)	Conversion[b] (%)	Selectivity[b] (%)	TOF[c] (h^{-1})
1	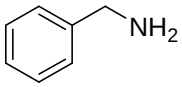	3	>99(82)	93	1.04
2	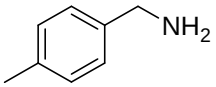	4	>99	75	0.78
3	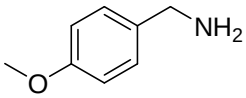	5	>99(80)	96	0.62
4	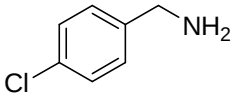	2	>99	98	1.56
5	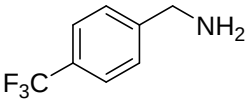	2	>99(96)	96	1.56
6	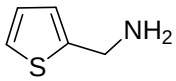	4	>99	92	0.78
7	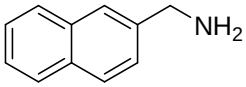	4	>99	80	0.78
8[d]	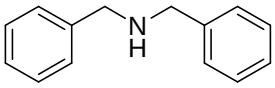	20	45	99	0.03
9[d]	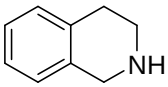	3	>99	95	0.56
10	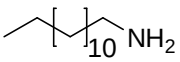	24	>99	50	0.13
11[e]	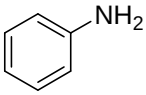	4	15	nd	nd

[a] Reaction conditions: amines (0.5 mmol), meso Cs/MnO_x (25 mg), toluene (5 mL), 110°C, air balloon. [b] Conversion and selectivity was determined by GC-MS based on the concentration of amines. Numbers in parenthesis refer to yields of isolated products. [c] TOF = TON / time (h), TON = moles of amines converted / moles of catalyst. [d] Meso Cs/MnO_x (50 mg). [e] Azobenzene was the only product. nd = not detected.

(20 h) and as well as higher amounts of catalyst (50 mg) were required. Oxidation of 1,2,3,4-tetrahydroisoquinoline (**Entry 9, Table 3.4**) produced a cyclic imine with high conversion (95%) and selectivity (95%). The remarkable catalytic activity of meso

Cs/MnO_x was demonstrated by the successful oxidation of a long chain inactive aliphatic amine (1-dodecylamine) to the corresponding imines (**Entry 10, Table 3.4**), though longer reaction time (24 h) was required. On the other hand, oxidation of aniline (lacking of α-H atoms) produced azo benzene as the only oxidation product (**Entry 11, Table 3.4**).

3.5.4.2 Spectral characterization of imine products

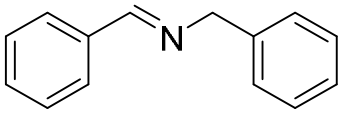

N-benzylidene benzylamine

Appearance: Yellow oil

^{1}H NMR (400 MHz, Chloroform-*d*): δ 8.41 (s, 1H), 7.80 (d, *J* = 4.2 Hz, 2H), 7.43 (dd, *J* = 5.1, 1.9 Hz, 3H), 7.37 (s, 4H), 7.27 (s, 1H), 4.85 (s, 2H).

^{13}C NMR (101 MHz, Chloroform-*d*): δ 161.78, 130.56, 128.41, 128.30, 128.09, 127.79, 126.79, 64.86.

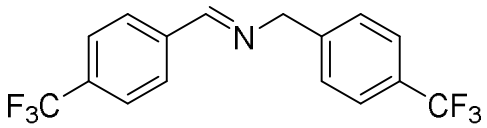

N-(4-(trifluoromethyl)benzylidene)(4-(trifluoromethyl)phenyl)methanamine

Appearance: Yellow oil

^{1}H NMR (400 MHz, Chloroform-*d*): δ 8.47 (s, 1H), 7.91 (d, *J* = 7.9 Hz, 2H), 7.69 (d, *J* = 8.0 Hz, 2H), 7.62 (d, *J* = 7.9 Hz, 2H), 7.48 (d, *J* = 7.8 Hz, 2H), 4.90 (s, 2H).

^{13}C NMR (101 MHz, Chloroform-*d*) δ 160.91, 142.85, 138.83, 128.34, 127.94, 125.39 (dd, *J* = 16.5, 3.6 Hz), 64.22.

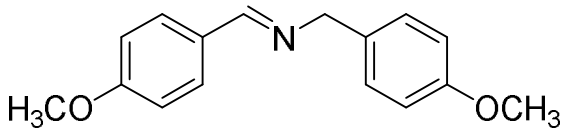

N-(4-methoxybenzylidene)(4-methoxyphenyl)methanamine

Appearance: Yellow oil

^{1}H NMR (400 MHz, Chloroform-*d*) δ 8.68 (s, 1H), 8.11 (d, *J* = 8.6 Hz, 2H), 7.64 (d, *J* = 8.4 Hz, 2H), 7.37 – 7.22 (m, 4H), 5.11 (s, 2H), 4.20 (d, *J* = 14.6 Hz, 6H).

^{13}C NMR (101 MHz, Chloroform-*d*) δ 162.06, 161.28, 159.04, 132.09, 130.19, 129.55, 114.33 (d, *J* = 6.7 Hz), 64.79, 55.72.

3.5.5 Oxidative cross-coupling of amines

For condition screening, reactions between benzylamine and 4-methoxybenzylamine were performed in different molar ratios (**Entry 1-3, Table 3.5**). The reaction having 1/3 molar ratio of benzylamine/4-methoxybenzylamine exhibited the highest selectivity towards the unsymmetrical imine (77% selectivity) with minimum formation of symmetrical imine (23% selectivity). Then, a variety of structurally different amines and benzylamine were tested with the best optimized reaction conditions (1/3 molar ratio). Using amines with electron releasing and electron withdrawing groups produced unsymmetrical imines with high (73 – 89%) selectivity (**Entry 3 - 5, Table 3.5**). An unsymmetrical imine having S heteroatom was synthesized (58% selectivity) by the reaction between benzylamine and 2-thiopheneamine using the established method (**Entry 6, Table 3.5**). The method was further utilized to perform a reaction between an aromatic amine (benzylamine) and aliphatic amines (butylamine and dodecylamine) (**Entry 7 - 8, Table 3.5**). The selectivity (>99%) towards the unsymmetrical imines was excellent

compared to the coupling of two aromatic amines. A very low selectivity (30% selectivity) of unsymmetrical imine was observed by a reaction between benzylamine and aniline.

Table 3.5 Aerobic oxidative cross coupling of benzylamine with different amines[a]

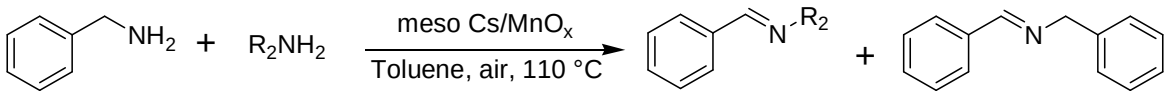

1a 2a

Entry	Substrate	Molar ratio[b]	Conversion[c] (%)	Selectivity[d] (%)	
				1a	2a
1	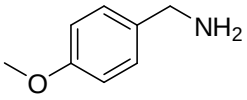	2/1	>99	62	25
2	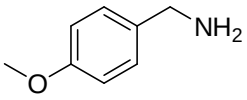	1/2	>99	30	70
3	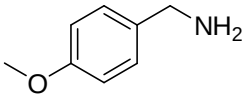	1/3	>99	23	77
4	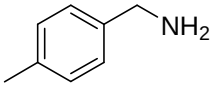	1/3	>99	10	89
5	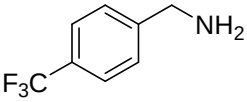	1/3	>99	27	73
6	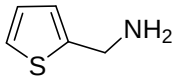	1/3	>99	42	58
7	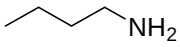	1/3	>99	nd	>99
8	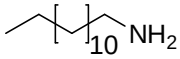	1/3	>99	nd	>99
9	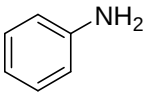	1/3	15	70	30

[a] Reaction conditions: benzylamine and other aromatic and aliphatic amines (0.5 mmol), meso Cs/MnO_x (25 mg), toluene (5 mL), 110°C, 3 h, air balloon. [b] Molar ratio of benzylamine and different amines. [c] Conversion was determined by GC-MS based on the concentration of benzylamine. [d] Selectivity was calculated based on self-coupled (1a) and cross-coupled (2a) products of benzylamine. nd = not detected.

3.5.6 Kinetic and mechanistic study

Time dependent experiments on oxidation of 4-methoxybenzylamine were conducted to study reaction kinetics (**Figure 3.7**). Formation of benzaldehyde in minutes was observed during the reaction pathway along with the desired imine as the major product. The apparent activation energy was calculated as 11.5 KJ mol^{-1} from the Arrhenius plot (**Figure 3.8A**). Kinetically relevant elementary steps in the reaction pathways were measured by changing the benzylic H to D in benzylamine. From the first order reaction plot between ln[benzylamine] and ln[benzylamine-α,α-d2], the obtained kinetic isotope effect (KIE) value was 2.04 (**Figure 3.8B**). This result signified abstraction of α C-H proton of amine as the rate determining step in the reaction.

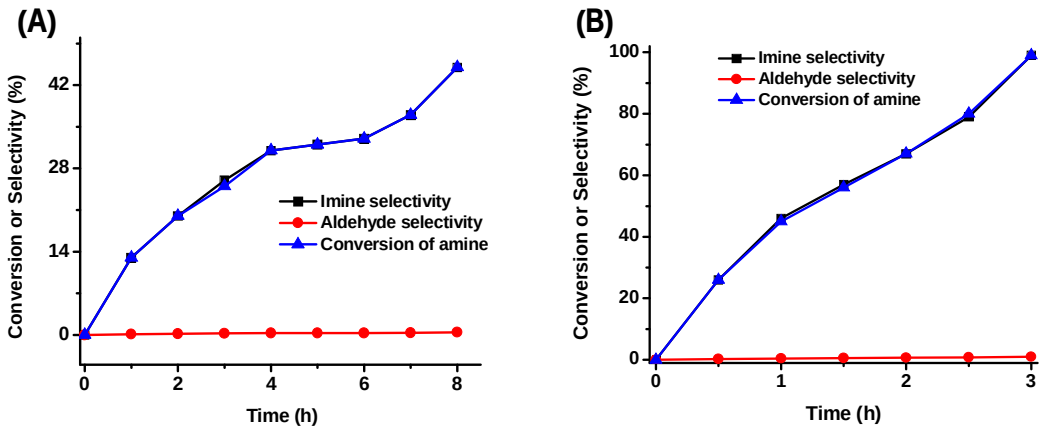

Figure 3.7 Time dependent studies of 4-methoxybenzylamine by meso Cs/MnO_x: (A) at 80°C and (B) at 110°C. Reaction condition: 4-methoxybenzylamine (0.5 mmol), catalyst (25 mg), solvent (5 mL), O_2 balloon, 3/8 h. The formation of benzaldehyde was clearly observed in both cases.

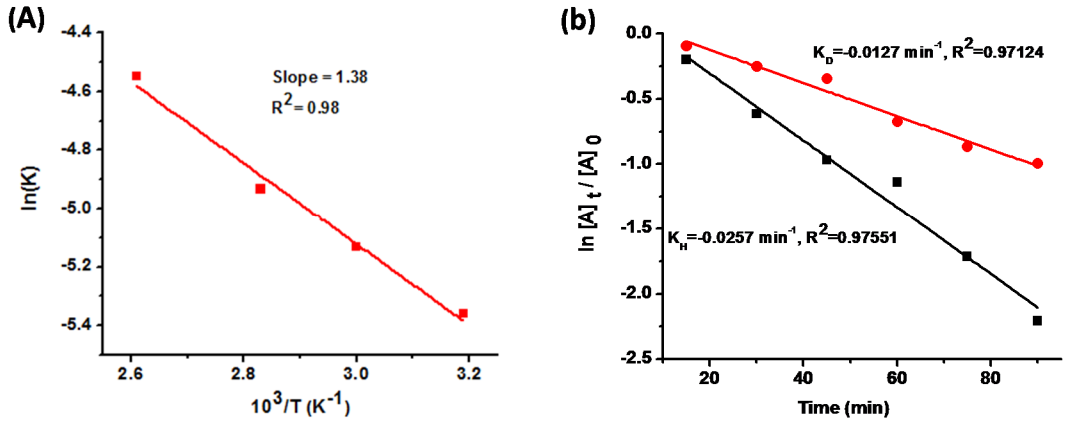

Figure 3.8 (A) Arrhenius plot for the oxidation of amine by meso Cs/MnO_x and (B) Kinetic plot of oxidation of benzylamine and benzylamine-α,α-d_2. The ratio of K_H/K_D = 2.02; which signified the oxidative dehydrogenation of benzylamine was the rate determining step. Reaction condition: amine (0.5 mmol), catalyst (25 mg), solvent (5 mL), 110°C, air balloon, 3 h. A_0: original concentration of substrate. A_t: concentration of substrate at time t. k: rate constant.

Benzylamine with electron withdrawing groups (CF_3 and Cl) displayed >99% conversion with TOF 1.56 h^{-1}, whereas the presence of electron donating groups (OCH_3 and CH_3) resulted in >99% conversion but lower TOF (0.78 h^{-1} for 4-methylbenzylamine and 0.68 h^{-1} for 4-methoxybenzylamine). The Hammett equation can be used to interpret the electronic or steric influence of the substituents on the reaction rate[24]. The relative rates of oxidation of para substituted benzylamines (p-Cl, p-H, p-Me, p-OMe) were investigated. A linear relationship was found between ln (k_x/k_H) and the Brown–Okamato constant (σ_p^+) (**Figure 3.9**). The slope of the plot resulted in a reaction constant (ρ) value of 1.264, which illustrated the development of a negative charge at the reaction center in the transition state of the rate-limiting step[25].

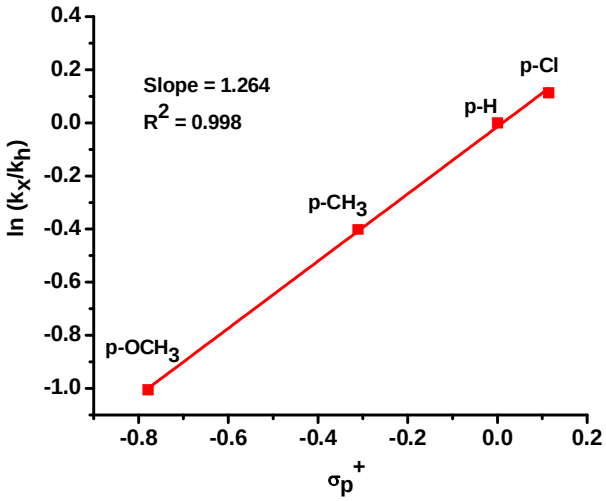

Figure 3.9 Hammett plot of competitive oxidation of para substituted benzylamine at 15 min of reaction time. Reaction condition: amine (0.5 mmol), catalyst (25 mg), solvent (5 mL), 110°C, air balloon, 15 min. A linear relationship between $\ln(k_x/k_H)$ and Brown–Okamoto constant (σ_p^+) for para substituted benzylamines with slope (ρ) of 1.264 were obtained, which indicated the formation of negatively charged intermediate.

3.6 Discussion

This study featured catalytic aerobic oxidation of amines to imines in the presence of meso Cs/MnOx. Diverse amine derivatives were converted to the corresponding imines efficiently. Catalytic reaction of halobenzene derivatives without dehalogenation is a challenge[40]. We tested oxidation of 4-chlorobenzylamine to verify any dehalogenation. >99% selectivity towards imines with no dehalogenated products were observed, indicating the effectiveness of meso Cs/MnO_x in oxidation of halogen containing substrates. Substrates bearing hetero atoms like S or N are known to poison transition metal oxide based catalysts due to strong coordination of the heteroatom to the transition metal centers. However, in the present study, 2-thiophene benzylamine was converted efficiently to the corresponding imines with no significant change of TOF and selectivity compared

to the benzylamines (Entry 6, Table 2). As observed, secondary amines can also be transformed to the corresponding imines with very high conversions (45 – 95%) and excellent selectivity (95 – 99%), but a much longer reaction time (20 h) and a higher amount of catalysts (50 mg) were required. This may be due to the steric effect due to the relative difficulty in abstracting the H atoms next to the N-H group. The reaction with dibenzylamine produced benzaldehyde as the side product, which can be attributed to the oxidative cleavage of the C=N bond of imine or the hydrolysis. Aliphatic amines are relatively difficult to oxidize as mentioned in the previous studies. However, in the case of oxidation of long chain inactive 1-dodecylamine by meso Cs/MnO_x, an imine was formed having twenty four carbon atoms. Such kinds of reactions with the inactive aliphatic amines have not been observed in previous studies. The bifunctional nature (oxidative and basic) of the meso Cs/MnO_x is believed to be the reason for the superior activity of the long chain 1-dodecylamine, as the dehydrogenation of the amine can be promoted by the basic nature of the catalyst. The easy diffusion and transportation of 1-dodecylamine in the mesoporous network may be the other reason behind the activity.

Depending on the molar ratio and nucleophilic properties of the partner amines, nonsymmetrical imines can also be synthesized efficiently. The reaction between an aromatic amine (benzylamine) and aliphatic amines (1-butylamine and 1-dodecylamine) produced nonsymmetrical imines with >99% selectivity. This can be attributed to the higher nucleophilic nature of aliphatic amines in comparison to aromatic amines. Once benzaldehyde was formed, the more nucleophilic aliphatic amines competed with benzylamine to minimize the self-coupling and yielded the unsymmetrical amines with very high selectivity (>99%). The difference in nucleophilic properties also explained the

relatively less selective unsymmetrical imine production from benzylamine and aniline. The lower nucleophilic property of anilines in comparison to benzylamine drove the reaction towards self-oxidative coupling of benzylamines (70% selectivity).

In general, a Mars-Van-Krevelen mechanism[26], is anticipated to occur for oxidation types of reactions over manganese oxides. According to the mechanism, structural defects and labile lattice oxygen are the key properties of manganese oxide catalysts. In this study, the poorly crystalline nature of the meso Cs/MnO_x promoted a facile supply of lattice oxygen, as observed by XPS and O_2-TPD studies. The basicities of the metal oxides are known to be increased due to the presence of electropositive alkali metal ions. As observed in our previous study, incorporation of trace amounts of electropositive Cs ions induced basicity in the meso MnO_x, which can be considered as surface defects of the material[27,28]. The presence of basic sites in the meso Cs/MnO_x material can enhance the oxidative dehydrogenation of amine by aiding the deprotonation of α C-H bond[29]. Secondary amines are considered as tough substrates for oxidation due to the inert nature of α C-H bonds[17]. However, in our study, an 87% increase of conversion of oxidation of an inert secondary amine (1,2,3,4-tetrahydroisoquinoline) was observed by incorporation of Cs in meso MnO_x. All of these experiments signified the poorly crystalline and bifunctional nature of meso Cs/MnO_x towards the augmented catalytic activity in oxidation of amines.

Based on experiments and the literature, we propose a mechanism for oxidation of amines by meso Cs/MnO_x (**Scheme 3.2**). Adsorbed amine molecules transferred an electron to the Mn center, followed by an elimination of an α C-H proton and an N-H proton to form the RCH=NH intermediate. The surface active Mn centers simultaneously involved a one electron reduction , which can lead to facile release of lattice oxygen,

thereby promoting the oxidation ability[30]. The labile lattice oxygen reoxidized the Mn center with production of H_2O_2, which could easily be decomposed over manganese oxide and form water. The abstraction of an α C-H proton produced the negatively charged intermediate (**Scheme 3.1**), which was the rate determining step as indicated by the linearity of the Hammett plot [positive value (1.264) of reaction constant (ρ)] and isotope labelling study. The trapping of negatively charged intermediate (by abstraction of α C-H proton) by addition of radical inhibitor was unsuccessful. This may be due to the formation of the intermediate inside the mesoporous network of the catalyst, where transportation of radical inhibitor was not proper. The supply of oxygen from the air is crucial for the catalytic activity, as loss of lattice oxygen should be replenished by the oxygen from the air. This also was supported by the observation that the elimination of air by nitrogen diminished the reaction rate. The reactive RCH=NH intermediate was rapidly hydrolyzed by the water and formed the aldehyde, which was condensed with another amine molecule to generate the corresponding imine.

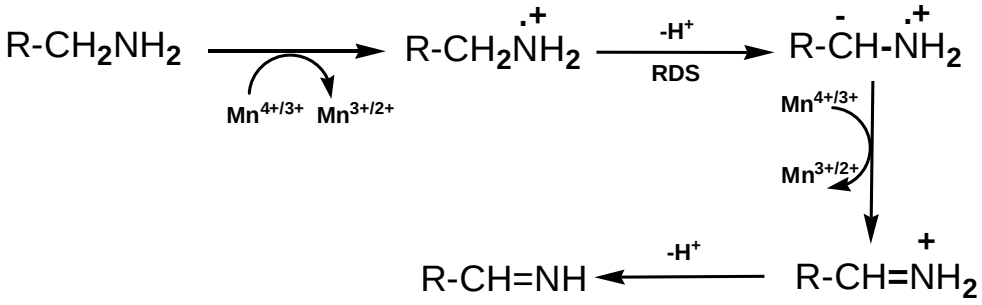

Scheme 3.1 Proposed reaction pathways of Mn mediated RCH=NH formation from amine. The forming of negatively charged intermediate due to abstraction of proton by oxidative dehydrogenation is the rate determining step (RDS).

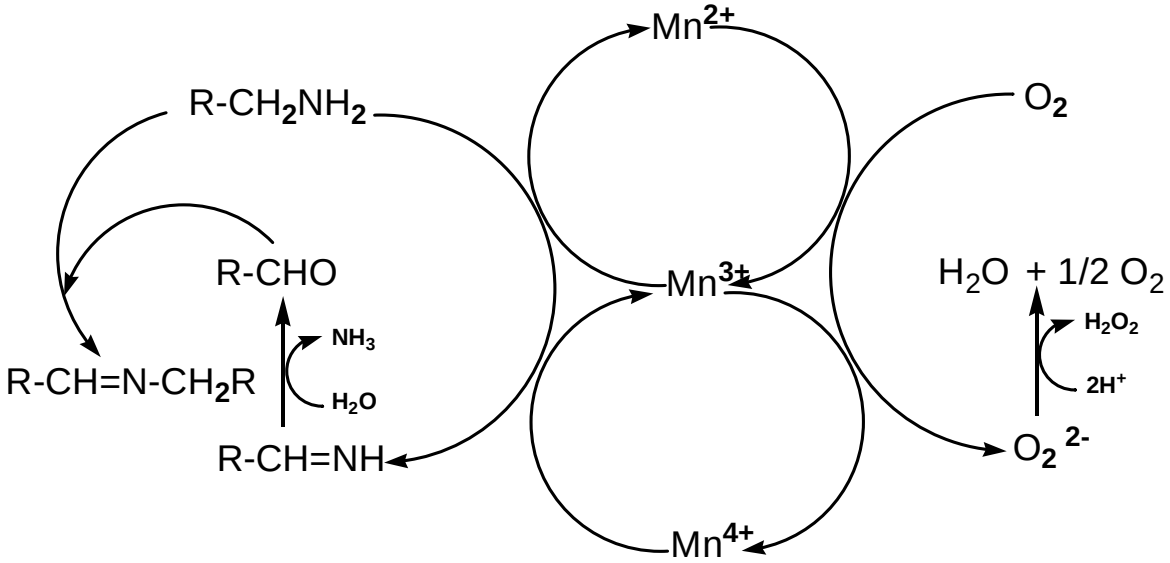

Scheme 3.2 Suggested overall mechanism of oxidation of amines over meso Cs/MnO_x following Mars-Van-Krevelen mechanism.

The role of adsorbed water in the catalyst surface (as observed by XPS) is also believed to be significant in the reaction system. A faster reaction rate was observed by the deliberate introduction of water in the reaction, which further confirms our process to follow the above-mentioned reaction pathways. The activation energy (11.5 $KJmol^{-1}$) was significantly lower than the previous study using α-MnO_2 catalyst and TBHP oxidant conducted at room temperature. The activation energy data suggested lower energy pathways for the meso Cs/MnO_x system under the present reaction conditions. The high surface area and the monomodal uniform mesoporous size distribution are the other important factors related to the catalytic activity. This can be attributed as enhanced catalytic activity of meso Cs/MnO_x (surface area 78 $m^2 g^{-1}$) compare to commercial nonporous Mn_2O_3 (surface area 11 $m^2 g^{-1}$) The high surface area of meso Cs/MnO_x exposed the lattice oxygen more to the surface, whereas the mesoporous network promoted the adsorption and molecular transportation of the substrates.

3.7 Conclusion

In summary, we demonstrated mesoporous Cs promoted manganese oxide as an efficient, selective, reusable, and, therefore, environmentally benign catalyst for the catalytic oxidation of amines to imines. The catalyst was able to oxidize diverse amine derivatives to produce imines with very high percent conversions (as high as >99%) and high selectivity (50 – 100%). The material was found to oxidize inactive long chain aliphatic amines (i.e. 1-dodecylamine) with quantitative conversion (>99%) and high selectivity (50% selectivity). The material was also able to promote the synthesis of nonsymmetrical imines including coupling of benzylamine with other aromatic and aliphatic amines with excellent selectivity (as high as >99%). Our mechanistic investigation revealed an involvement of surface active Mn^{3+} species, labile lattice oxygen, and the basic nature of the catalyst towards the augmented catalytic activity. High surface area, low crystalline nanoparticle nature and presence of mesoporous structure are the other crucial factors.

3.8 References

(1) Kobayashi, S.; Mori, Y.; Fossey, J. S.; Salter, M. M. *Chem. Rev.* **2011**, *111*, 2626-2704.

(2) Naeimi, H.; Salimi, F.; Rabiei, K. . *Mol. Catal. A: Chem.* **2006**, *260*, 100-104.

(3) Westheimer, F.; Taguchi, K. *J. Org. Chem.* **1971**, *36*, 1570-1572.

(4) Nicolaou, K.; Mathison, C. J.; Montagnon, T. *Angew. Chem.* **2003**, *115*, 4211-4216.

(5) Wang, J.-R.; Fu, Y.; Zhang, B.-B.; Cui, X.; Liu, L.; Guo, Q.-X. *Tetrahedron Lett.* **2006**, *47*, 8293-8297.

(6) Zhu, B.; Lazar, M.; Trewyn, B. G.; Angelici, R. J. *J. Catal.* **2008**, *260*, 1-6.

(7) Grirrane, A.; Corma, A.; Garcia, H. *J. Catal.* **2009**, *264*, 138-144.

(8) Zhu, B.; Angelici, R. J. *Chem. Commun.* **2007**, 2157-2159.

(9) Taketoshi, A.; Koizumi, T.-a.; Kanbara, T. *Tetrahedron Lett.* **2010**, *51*, 6457-6459.

(10) Murahashi, S.-I.; Okano, Y.; Sato, H.; Nakae, T.; Komiya, N. *Synlett* **2007**, *2007*, 1675-1678.

(11) Huang, H.; Huang, J.; Liu, Y.-M.; He, H.-Y.; Cao, Y.; Fan, K.-N. *Green Chem.* **2012**, *14*, 930-934.

(12) Dhakshinamoorthy, A.; Alvaro, M.; Garcia, H. *ChemCatChem* **2010**, *2*, 1438-1443.

(13) Zhang, Z.; Wang, F.; Wang, M.; Xu, S.; Chen, H.; Zhang, C.; Xu, J. *Green Chem.* **2014**, *16*, 2523-2527.

(14) Maeda, Y.; Nishimura, T.; Uemura, S. *Bull. Chem. Soc. Jpn.* **2003**, *76*, 2399-2403.

(15) Lang, X.; Ji, H.; Chen, C.; Ma, W.; Zhao, J. *Angew. Chem., Int. Ed.* **2011**, *50*, 3934-3937.

(16) Ovoshchnikov, D.; Donoeva, B.; Golovko, V. B. *ACS Catal.* **2014**.

(17) Yuan, B.; Chong, R.; Zhang, B.; Li, J.; Liu, Y.; Li, C. *Chem. Commun.* **2014**, *50*, 15593-15596.

(18) Furukawa, S.; Ohno, Y.; Shishido, T.; Teramura, K.; Tanaka, T. *ACS Catal.* **2011**, *1*, 1150-1153.

(19) Hu, Z.; Kerton, F. M. *Org. Biomol. Chem.* **2012**, *10*, 1618-1624.

(20) Biswas, S.; Poyraz, A. S.; Meng, Y.; Kuo, C.-H.; Guild, C.; Tripp, H.; Suib, S. L. *Appl. Catal., B: Environ.* **2015**, *165*, 731-741.

(21) Özacar, M.; Poyraz, A. S.; Genuino, H. C.; Kuo, C.-H.; Meng, Y.; Suib, S. L. *Appl. Catal., A: Gen.* **2013**, *462*, 64-74.

(22) Genuino, H. C.; Dharmarathna, S.; Njagi, E. C.; Mei, M. C.; Suib, S. L. *J. Phys. Chem. C* **2012**, *116*, 12066-12078.

(23) Sithambaram, S.; Kumar, R.; Son, Y.-C.; Suib, S. L. *J. Catal.* **2008**, *253*, 269-277.

(24) Johnson, C. D. *The Hammett Equation*; CUP Archive, 1973.

(25) Brown, H. C.; Okamoto, Y. *J. Am. Chem. Soc.* **1958**, *80*, 4979-4987.

(26) Doornkamp, C.; Ponec, V. . *Mol. Catal. A: Chem.* **2000**, *162*, 19-32.

(27) Martra, G.; Ocule, R.; Marchese, L.; Centi, G.; Coluccia, S. *Catal. Today* **2002**, *73*, 83-93.

(28) Helwani, Z.; Othman, M.; Aziz, N.; Kim, J.; Fernando, W. *Appl. Catal., A: Gen.* **2009**, *363*, 1-10.

(29) Zheng, N.; Stucky, G. D. *Chem. Commun.* **2007**, 3862-3864.

(30) Makwana, V. D.; Son, Y.-C.; Howell, A. R.; Suib, S. L. *J. Catal.* **2002**, *210*, 46-52.

CHAPTER 4. Facile Access to Versatile Functional Groups from Alcohol by Single Multifunctional Reusable Catalyst

4.1 Abstract

Tandem oxidation processes enabling one-pot multistep reactions received great attention as an efficient synthetic methodology for construction of complex molecules from simple substrates by a single operation. We report here tandem oxidative transformations of seven different functional groups (imine, imidazole, cyanide, amide, lactone, ester and olefin) from a single substrate (alcohol) by a single cesium promoted mesoporous manganese oxide catalyst (meso Cs/MnO_x). High conversions were obtained with a broad range of substrates including aliphatic long chain alcohols. The catalyst can be reused without any loss of catalytic activity. We also demonstrated a unique multiple esterification reaction from a single aliphatic alcohol under aerobic atmospheric conditions catalyzed by meso Cs/MnO_x.

4.2 Background and significance

The development of cleaner, safer and environment friendly technologies by using renewable feedstocks, reducing chemical wastes and working with ecofriendly reagents has been stimulated by extensive research in past decades. To this end, tandem catalysis that enables “one-pot” multistep reactions, followed by a single work up, has drawn much attention. “One-pot” processes have several advantages: 1) operational simplicity due to a reduced number of steps; 2) significant time-cost benefits; 3) preventing isolation of

volatile and toxic intermediates and 4) less waste generation. Although several types of transition metal based catalysts have been introduced for tandem catalysis, most systems are homogeneous which have shortcomings of product separations and catalyst reusability. One the other hand, truly heterogeneous systems capable of performing tandem reactions with proper reusability have scarcely been reported. Moreover, a single, cost-effective, multifunctional heterogeneous catalyst for versatile tandem one-pot reactions from a single substrate is not yet known.

Manganese oxides as catalysts in 'tandem oxidation processes' (TOP) was first developed by establishing a synthetic route for the preparation of antibiotics, where a MnO_2 mediated oxidation combined with a Wittig olefination was performed.[1] In TOP, oxidation of alcohols is followed by trapping the intermediate aldehydes or ketones by nucleophilic reagents to form the desired product. Manganese oxide has been utilized in TOP such as formation of imines, amides, quinoxalines, and terminal alkynes directly from alcohols.[2-6] However, manganese oxide mediated, challenging, and tandem oxidative reactions involving three or more steps have not significantly been explored.

Nitrogen containing derivatives, such as imines, imidazoles, cyanides and amides, are key building blocks in the syntheses of natural products and biological compounds.[7,8] Regarding several strategies, one-pot TOP between alcohols and related nucleophiles are most acceptable, due to use of cheap and stable starting material (alcohol).[1,9,10] However, the effective catalytic systems for one-pot TOP involve either precious metals, long reaction times, or have narrow applicability for a limited numbers of alcohols.[11-14] The other important aspect of TOP is to utilize commercially available alcohols in carbon-carbon bond formation, a fundamental reaction in organic synthesis. To this end, one pot

metal catalyzed oxidation/olefination of alcohols with ketones and Wittig reagents are two common technologies.[15-19] Other functionalities such as esters are widely used in fine chemicals, natural products, and fuel additives.[20] Among several methodologies, oxidative esterification of alcohols is a promising protocol in terms of green, economical, and sustainable chemistry. Nevertheless, most of the heterogeneous systems in this regard are based on noble metals (Au, Pd), and the assistance of basic promoters are inevitable to achieve high efficiency.[21,22]

Herein, we document cesium ion promoted mesoporous manganese oxide (meso Cs/MnO_x) material as a multifunctional catalyst for transformation of alcohol to different functional moieties in one-pot tandem oxidative conditions. Seven different functional groups (imine, imidazole, cyanide, amide, lactone, ester and olefin) can be obtained starting from alcohol by the same catalyst (**Scheme 4.1**). The catalytic procedure described herein has the following advantages over the current catalytic systems for the tandem oxidation process: 1) a variety of commercially available alcohols can be used as starting material to produce different functional groups; 2) reactions can be done mostly in aerobic atmospheric conditions; 3) water is the only by-product in most of the reactions; 4) inexpensive manganese oxide can be used as a catalyst instead of precious metal based systems; and 5) products can be separated easily by simple filtration and the catalyst is reusable.

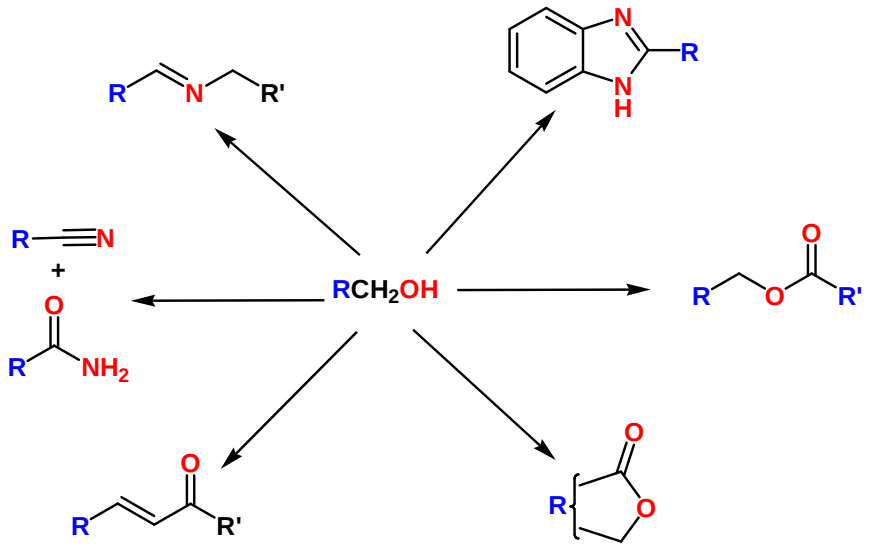

Scheme 4.1 Versatile tandem oxidation process from alcohol by meso Cs/MnO_x

4.3 Experimental Section

4.3.1 Synthesis of mesoporous Cs/MnO_x

The catalyst was synthesized following the procedure described in Chapter 3. In a typical synthesis 0.02 mol of manganese nitrate tetrahydrate ($Mn(NO_3)_2 \cdot 4H_2O$) and 0.134 mol of 1-butanol were added into a 120 mL beaker. To this solution 0.0034 mol of poly(ethyleneglycol)-block-poly(propyleneglycol)-block-poly(ethyleneglycol) (Pluoronic P123, $PEO_{20}PPO_{70}PEO_{20}$, molar mass 5750 g mol^{-1}) and 0.032 mol of concentrated nitric acid (HNO_3) were added, and stirred at room temperature until the solution became clear (light pink). To this clear solution 200 µL of 1.0 M cesium nitrate ($CsNO_3$) aqueous solution was added maintaining the Cs loading to 1.0 % with respect to Mn by mol (though ICP-MS revealed very low loading (0.16%) of Cs with respect to Mn). The resulting clear solution was then kept in an oven at 120°C for 3 h under air. The product was collected

and washed with excess ethanol, centrifuged, and dried in a vacuum oven overnight. At the end, the dried black powders were subjected to a heating cycle. First they were heated at 150°C for 12 h and cooled down to room temperature under ambient conditions followed by a second heating step of 250°C for 3 h.

4.3.2 Catalytic activity measurement

4.3.2.1 Preparation of imines

In a 25 mL one necked round bottom flask equipped with a condenser, a mixture of alcohol (1.0 mmol), amine (2.0 mmol), catalyst (50 mg) and toluene (5 mL) was added. The reaction mixture was heated to reflux under vigorous stirring (700 rpm) for the required time under an air balloon. After reaction, the mixture was cooled and the catalyst was removed by filtration. The product analysis was done using GC-MS (gas chromatography-mass spectrometry). The conversion was determined based on the concentration of alcohols. Most reactions were repeated twice and the average values were used. For kinetic experiments, a two-necked flask was used where the other neck was used as a sampling port.

4.3.2.2 Preparation of benzimidazoles

In a 25 mL two necked round bottom flask equipped with a condenser, a mixture of alcohol (0.5 mmol), catalyst (50 mg) and toluene (5 mL) was added. The reaction mixture was heated to reflux under vigorous stirring (700 rpm) for the required time under an air balloon. The consumption of alcohol was monitored by GC-MS. After complete conversion of alcohol to aldehyde, *ortho*-phenyldiamine (1.0 mmol) was introduced into the reaction mixture in order to scavenge the aldehyde. After reaction, the mixture was

cooled and the catalyst was removed by filtration. The product analysis was done using GC-MS.

4.3.2.3 Preparation of α,β unsaturated ketones

Coupling of alcohol and Wittig reagent: A mixture of alcohol (0.5 mmol), Wittig reagent (1.0 mmol), catalyst (100 mg), and toluene (5 mL) was placed in a 25 mL round bottom flask equipped with a condenser. The reaction mixture was heated to reflux under vigorous stirring (700 rpm) for the required time under an air balloon. After reaction, the mixture was cooled, and the catalyst was removed by filtration. The product analysis was done using GC-MS. The conversion was determined based on the concentration of alcohol.

Coupling of acetophenone and benzyl alcohol: A mixture of benzyl alcohol (0.5 mmol), acetophenone (1.0 mmol), catalyst (100 mg), K_2CO_3 (1.5 mmol) and toluene (5 mL) was placed in a 25 mL round bottom flask equipped with a condenser. The reaction mixture was heated to reflux under vigorous stirring (700 rpm) for the required time under an air balloon. After reaction, the mixture was cooled, and the catalyst was removed by filtration. The product analysis was done using GC-MS. The conversion was determined based on the concentration of benzyl alcohol.

Coupling of 1-phenylethanol and benzyl alcohol: A mixture of benzyl alcohol (0.5 mmol), 1-phenylethanol (1.0 mmol), catalyst (100 mg), K_2CO_3 (1.5 mmol) and toluene (5 mL) was placed in a 25 mL round bottom flask equipped with a condenser. The reaction mixture was heated to reflux under vigorous stirring (700 rpm) for the required time under an air balloon. After reaction, the mixture was cooled, and the catalyst was removed by filtration. The product analysis was done using GC-MS. The conversion was determined based on the concentration of benzyl alcohol.

4.3.2.4 Preparation of amides

The oxidation experiments of alcohols to amide were carried out in a 100 mL cylindrical stainless steel pressurized reactor made by PARR Instrument Company, USA. The reactor was charged with a mixture of alcohol (0.5 mmol), catalyst (100 mg), acetonitrile (10 ml) and aqueous ammonia (28 wt%, 400µL), followed by purging with oxygen and pressurized to 5 bar. The reactor was then heated to 130°C for 15 h with constant stirring. After reaction, the reactor was cooled to room temperature and the catalyst was removed by filtration. The product analysis was done using GC-MS.

4.3.2.5 Preparation of esters

In a 25 mL two necked round bottom flask equipped with a condenser, a mixture of alcohol (4 mL) and catalyst (100 mg) was added. The reaction mixture was heated to reflux under vigorous stirring (700 rpm) for the required time under an air flow. After reaction, the mixture was cooled and the catalyst was removed by filtration. The product analysis was done using GC-MS. The conversion was determined based on the concentration of alcohol.

4.3.2.6 Preparation of lactones

In a 25 mL one necked round bottom flask equipped with a condenser, a mixture of diol (0.5 mmol), catalyst (50 mg) and toluene (5 mL) was added. The reaction mixture was heated to reflux under vigorous stirring (700 rpm) for 15 h under an air balloon. After reaction, the mixture was cooled and the catalyst was removed by filtration. The product analysis was done using GC-MS. The conversion was determined based on the concentration of alcohol.

4.3.3 Analysis of reaction products

The Gas chromatography – mass spectra (GC-MS) analyses were performed by a 7820A GC system connected with a thermal conductivity detector of 5975 series MSD from Agilent Technologies and a nonpolar cross-linked methyl siloxane column with dimensions of 12 in × 0.200 mm × 0.33 µm. The ^{1}H and ^{13}C nuclear magnetic resonance (NMR) spectra were recorded on a Bruker AVANCE III- 400 MHz spectrometer. ^{1}H NMR spectra were collected at 400 MHz with chemical shift referenced to the residual peak in $CDCl_3$ (δ: H 7.26 ppm). ^{13}C NMR spectra were collected at 100 MHz and referenced to residual peak in $CDCl_3$ (δ: C 77.23 ppm). Multiplicities are written as s (singlet), d (doublet), t (triplet), and m (multiplet).

4.4 Time-of-flight secondary ion mass spectrometry (TOF-SIMS) measurement

We used time-of-flight secondary ion mass spectrometry (TOF-SIMS) to determine the lateral and depth homogeneity of Cs ions on the manganese oxide surface. As revealed from **Figures 4.1 and 4.2**, the highest relative level of Cs is on the surface, however, Cs also penetrated into the bulk.

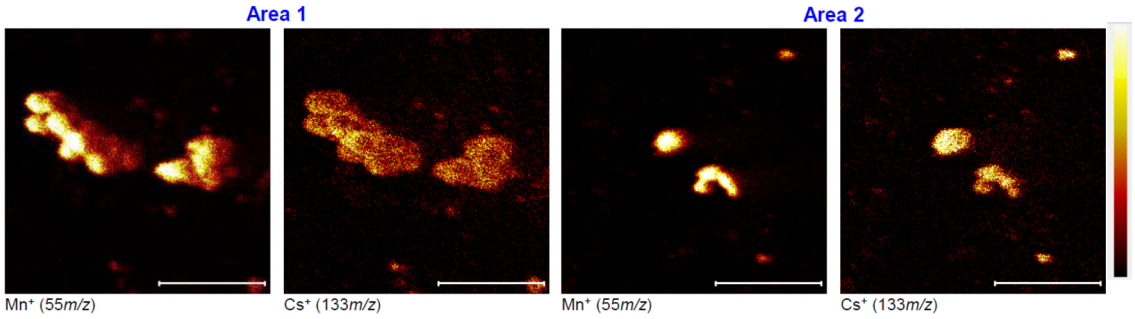

Figure 4.1 TOF-SIMS images of meso Cs/MnO_x in two different regions (scale bar is 10 µm).

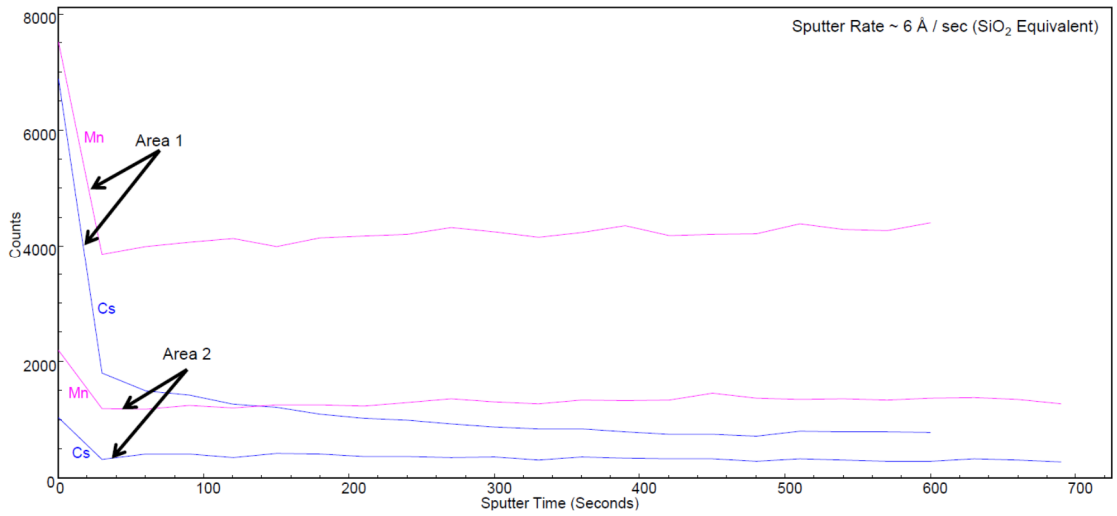

Figure 4.2 TOF-SIMS depth profiles of meso Cs/MnO_x in two different regions.

TOF-SIMS experiments were performed with a PHI *nanoTOF* II instrument from Physical Electronics. The liquid metal ion gun (LMIG) utilized focused ion beams of Bi_3^{++} (60 keV) for both the analysis and sputtering. A water vapor leak was used to keep the surface oxidized during sputtering for more uniform ion yields. The depth profiles were extracted from the particle region only.

4.5 Catalytic reactions

4.5.1 One-pot imine formation

4.5.1.1 Substrate scope

Initially, we focused on one-pot tandem imine formation from alcohols and amines. The imine products could be separated easily by basic alumina column chromatography using hexane and dichloromethane as solvent. The isolated yields of some of the imine derivatives are given in **Table 4.1**. We first selected n-butylamine as a model nucleophile and reacted this with alcohols having diverse structures. A reaction between benzyl alcohol and n-butylamine produced the corresponding imine with a very high conversion (>99%)

and selectivity (>99%) **[Table 4.1, Entry 1]**. Whereas, benzyl alcohol with different functional groups (electron withdrawing and electron donating) formed the corresponding imines with excellent conversion (>99%) and moderate selectivity **[Table 4.1, Entry 2-3]**. The other products were the corresponding aldehydes. Meso Cs/MnO_x displayed high conversion (>99%) and selectivity (94%) towards imine when 2-thiophenemethanol was used as the substrate **[Table 4.1, Entry 4]**. High activity (77% conversion, 60% selectivity) in tandem oxidation of an allylic alcohol (cinnamyl alcohol) **[Table 4.1, Entry 5]** revealed the superior chemo-selectivity nature of the meso Cs/MnO_x, since no reaction at the double bond was identified by GC-MS. A bulky alcohol (2-napthylmethanol) was converted to the corresponding imine efficiently **[Table 4.1, Entry 6]**. The catalyst was also able to oxidize a sterically hindered alcohol to corresponding imine in high conversion (90%) **[Table 4.1, Entry 7]**. However, a longer reaction time (8 h) as well as higher amount of catalyst (100 mg) were required. Furthermore, a reaction between an inactive long chain alcohol (n-dodecyl alcohol) and a long chain amine (n-dodecylamine) produced an imine bearing 24 carbon atoms with moderate conversion (20%) but excellent selectivity (>99%) **[Table 4.1, Entry 8]**. The catalyst also exhibited high conversions and selectivity when structurally different amines were selected as substrates **[Table 4.1, Entry 9-12]**. N-benzylideneaniline was produced with excellent selectivity (>99%) by a reaction between benzyl alcohol and aniline **[Table 4.1, Entry 9]**. Direct imine formation between benzyl amine and benzyl alcohol was observed with a very high conversion (>99%) and selectivity (>99%) **[Table 4.1, Entry 10]**. A very low conversion (40 %) was achieved by selecting a weak nucleophilic amine (4-nitro benzylamine) **[Table 4.1, Entry 11]**, whereas amines with a

higher nucleophilic nature produced imines with excellent conversion (>99%) and selectivity (>99%) **[Table 4.1, Entry 1, 12]**.

Table 4.1 Tandem imine formation from alcohol by meso Cs/MnO_x [a]

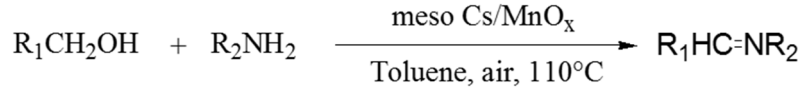

Entry	R_1	R_2	time [h]	Conv. [%][b]	Selec. [%][b,c]	TON[d]
1	Ph	n-butyl	2	>99	>99 (89)	3.3
2	4-OMe-Ph	n-butyl	2	97	56	3.2
3	4-NO_2-Ph	n-butyl	2	90	75	3.0
4	2-thiophene	n-butyl	6	>99	94	3.3
5	cinnamyl	n-butyl	6	77	60	2.6
6	2-napthalene	n-butyl	2	97	56	3.2
7[e]	2,4,6-trimethyl-Ph	n-butyl	8	90	75	3.0
8[e]	n-dodecyl	n-dodecyl	20	25	>99	0.8
9	Ph	Ph	2	>99	>99 (87)	3.3
10	Ph	$PhCH_2$	2	>99	>99 (82)	3.3
11	Ph	4-NO_2-Ph-CH_2	15	40	80	1.3
12	Ph	n-dodecyl	4	>99	>99	3.3

[a] Reaction Conditions: Alcohols (1.0 mmol), amines (2.0 mmol), catalyst (50 mg), toluene (5 mL),110°C, air balloon. [b] Determined by GC-MS. Numbers in parenthesis refer to yields of isolated products. [c] The other products were the corresponding aldehydes. [d] TON = no of moles of alcohol converted per mole of catalyst. [e] 100 mg catalyst were used.

4.5.1.2 Spectral charecterozation of imine products

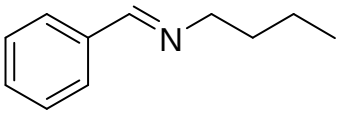

N-benzylidenebutan-1-amine

^{1}H NMR (400 MHz, Chloroform-*d*): δ 8.13 (t, *J* = 1.3 Hz, 1H), 7.66 – 7.54 (m, 2H), 7.31 – 7.23 (m, 3H), 3.48 (td, *J* = 7.0, 1.4 Hz, 2H), 1.66 – 1.49 (m, 1H), 1.30 – 1.20 (m, 2H), 0.82 (t, *J* = 7.4 Hz, 3H).

^{13}C NMR (101 MHz, Chloroform-*d*): δ 160.79, 136.45, 130.49, 128.62, 128.09, 61.53, 33.09, 20.54, 13.98.

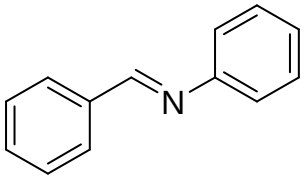

N-benzylidenebenzenamine

^{1}H NMR (400 MHz, Chloroform-*d*): δ 8.54 (s, 1H), 8.08 – 7.97 (m, 2H), 7.57 (hept, *J* = 3.6 Hz, 3H), 7.50 (t, *J* = 7.8 Hz, 2H), 7.37 – 7.32 (m, 3H).

^{13}C NMR (101 MHz, Chloroform-*d*) δ 160.02, 151.76, 135.92, 131.04, 128.85, 128.51, 128.44, 125.64, 120.59.

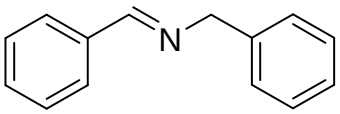

N-benzylidene benzylamine

^{1}H NMR (400 MHz, Chloroform-*d*): δ 8.32 (t, *J* = 1.4 Hz, 1H), 7.74 – 7.68 (m, 2H), 7.34 (d, *J* = 2.2 Hz, 2H), 7.33 (d, *J* = 1.8 Hz, 1H), 7.27 (s, 2H), 7.26 (s, 2H), 7.21 – 7.16 (m, 1H), 4.75 (d, *J* = 1.5 Hz, 2H).

^{13}C NMR (101 MHz, Chloroform-*d*): δ 162.10, 139.44, 136.31, 130.88, 128.72, 128.62, 128.40, 128.10, 127.11, 65.18.

4.5.1.3 Resuablility and heterogenity

Control experiments were then performed to verify the heterogeneous nature of the catalyst. We tested catalytic transformation of benzyl alcohol and n-dodecylamine under tandem oxidation conditions by meso Cs/MnO_x. After the reaction, the catalyst was removed by filtration and the filtrate was tested by inductively coupled plasma (ICP) analysis. No Mn and Cs ions were detected by ICP and a minute change in Cs amount (0.04%) was observed in the used material. X-ray diffraction (XRD) analyses before and after use revealed no change of amorphous structure of the material **(Figure 4.3)**. Furthermore, the catalyst could be reused with the same catalytic performance for at least three times **(Table 4.2)**. On the basis of these observations, we can conclude that our catalyst has truly heterogeneous nature, and is not only active but also has sustainability and reusability.

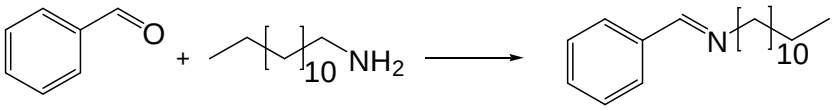

Table 4.2. Reusability test of the catalyst[a]

Entry	Cycle	Conversion [%]	TON
1	1	33	2.2
2	2	35	2.3
3	3	33	2.2

[a] Reaction condition: benzyl alcohol (1.0 mmol), n-dodecylamine (2.0 mmol), meso Cs/MnO_x (25 mg), toluene (5 mL), 110°C, 1 h, air balloon. Turnover number (TON) = [reacted mol amine]/[total mol catalyst].

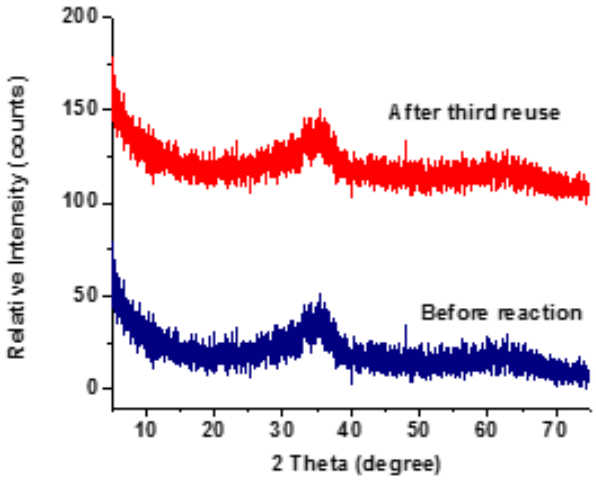

Figure 4.3 Powder X-ray diffraction of meso Cs/MnO_x before and after third reuse.

4.5.1.4 Mechanistic investigation

To gain insight into the origin of the catalytic activity of meso Cs/MnO_x, we have selected tandem imine conversion of benzyl alcohol and n-dodecylamine as the model reaction. We first observed the oxidation of benzyl alcohol in absence of amine (**Figure 4.4**). Next, a significant increase of conversion was achieved in the presence of amine, due to fast consumption of benzaldehyde (**Figure 4.4**). On the other hand, no significant difference in conversion was found in the direct condensation of benzaldehyde and n-dodecylamine in the presence of catalyst. We then selected a poorly nucleophilic amine (4-nitroaniline) and performed the condensation reaction in the presence of catalyst. Meso Cs/MnO_x was found to expedite the condensation of benzaldehyde and 4-nitroaniline by 21% after 3 h of reaction (**Table 4.3**).

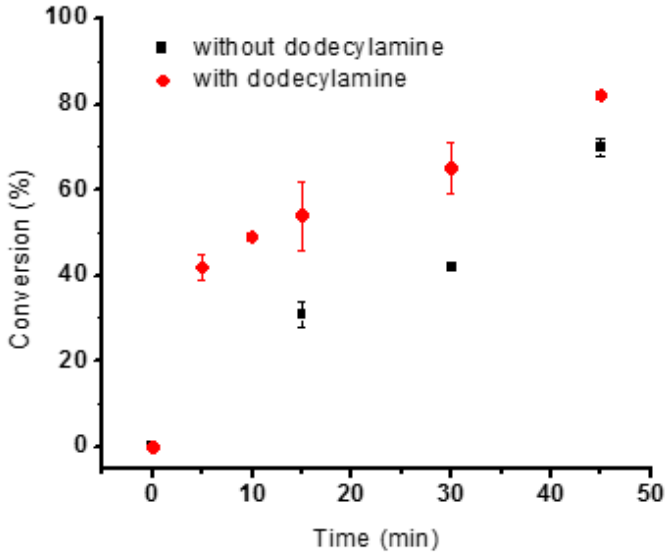

Figure 4.4 Conversion of benzyl alcohol over time course with and without n-dodecylamine. Reaction condition: benzyl alcohol (1.0 mmol), n-dodecylamine (2.0 mmol), meso Cs/MnO_x (50 mg), toluene (5 mL), 110°C, air balloon.

Table 4.3. Percent Conversion of condensation of benzaldehyde and 4-nitroaniline.[a]

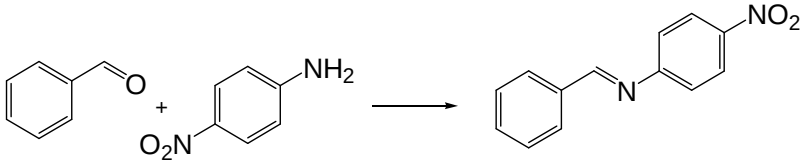

Entry	Time [min]	No catalyst	Meso Cs/MnO_x
1	0	0	0
2	30	5	8
3	60	23	30
4	120	51	56
5	180	58	70

[a] Reaction condition: benzaldehyde (1.0 mmol), 4-nitroaniline (2.0 mmol), meso Cs/MnO_x (50 mg), toluene (5 mL), 110°C.

4.5.2 Benzimidazole formation

Benzimidazole derivatives are nitrogen containing cyclic compounds, which are classically synthesized by coupling of *ortho*-phenyldiamine and carboxylic acid derivatives under acidic and harsh reaction condition.[23] We synthesized benzimidazole derivatives by combining oxidation of alcohols to aldehydes followed by condensation with *ortho*-phenyldiamine with under tandem one-pot conditions. In an initial attempt, no product was found when we use benzyl alcohol and *ortho*-phenyldiamine at the same time in reaction mixture. A competitive adsorption of alcohol and diamine in the porous catalysts may be the reason behind the reluctance of both reactants to react at the same time. Therefore, we first conducted the oxidation of benzyl alcohol by the catalyst in the presence of air at 110°C. The diamine was incorporated after full conversion of benzyl alcohol to benzaldehyde to afford the desired benzimidazole compound. Using this sequential addition of diamine after full conversion of alcohol, the corresponding imidazole was formed with 50% selectivity after 15 h of reaction. The other product was the intermediate aldehyde. Both benzyl alcohol and 2-napthyl alcohol **[Table 4.4, Entry 1-2]** produced the corresponding imidazole under aerobic one-pot conditions. Based on previous reports, the imidazole formation reaction was believed to be promoted by one pot multiple transformations over meso Cs/MnO_x, involving a manganese oxide assisted catalytic oxidation of alcohol to aldehyde, and an oxidative dehydrogenation of benzimidazoline derivatives generated from the condensation of *ortho*-phenylenediamine and aldehyde (**Scheme 4.2**)[14,24]. However, in our study the benzimidazoline intermediate has not been identified by GC-MS, which is due to the facile oxidation of C-N bonds of benzimidazoline by meso Cs/MnO_x. This is in agreement with our previous study, where

the catalyst exhibited superior activity in oxidation of C-N bonds of amines to imines promoted by the Cs ion induced basicity of manganese oxide [25].

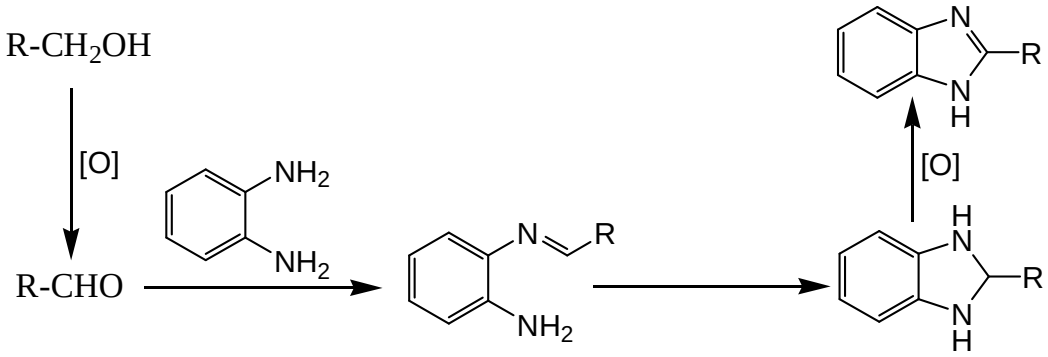

Scheme 4.2. Possible reaction pathways of imidazole formation over meso Cs/MnO_x.

4.5.3 Oxidative amidation

Synthesis of amide from primary alcohols and ammonia in the presence of O_2 is a challenge, since the catalyst can be deactivated in presence of ammonia and water. In our case, primary amides can be synthesized from primary alcohol and ammonia using meso Cs/MnO_x. The reactions between benzyl alcohol and 4-methoxy benzyl alcohol with aqueous ammonia (28 wt%, 400µL) under O_2 (5 atm) produced the corresponding amide and nitrile with excellent conversion (>99%) high selectivity (25/75% and 70/30% selectivity of amide/nitrile respectively) **[Table 4.4, Entry 3 and 4]**. Meso Cs/MnO_x has shown several advantages in primary amide syntheses, such as, use of inexpensive manganese oxide, easy handling of aqueous ammonia, water as the only side product, and readily available alcohols as the starting reagents. The possible reaction pathway can be described as a one-pot four step process: (1) oxidation of alcohol to aldehyde, (2) condensation of aldehyde and ammonia to produce the aldimine intermediate, (3) oxidative dehydrogenation of aldimine to cyanide and (4) hydration of cyanide to amide.

Table 4.4 Various tandem reactions from alcohols by meso Cs/MnO_x [a]

Entry	Alcohol	Amine	Product	Time (h)	GC yield [b] (%)
1 [c]	$PhCH_2OH$	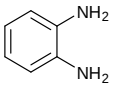	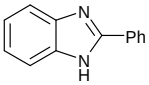	15	50 [d]
2 [c]	$NpCH_2OH$	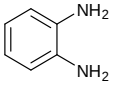	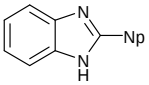	15	50 [d]
3 [e]	$PhCH_2OH$	NH_4OH	$PhCONH_2$	15	25 [f]
4 [e]	4OMe-$PhCH_2OH$	NH_4OH	4OMe-$PhCONH_2$	15	70 [f]
5	$PhCH_2OH$	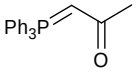	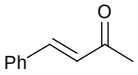	4	80 [d]
6	n-dodecyl-OH	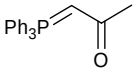	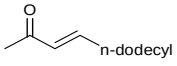	24	90 [d]
7 [g]	$PhCH_2OH$	$PhCOCH_3$	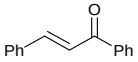	36	80 [d]
8 [g]	$PhCH_2OH$	$PhCHOHCH_3$	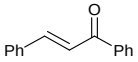	24	20 [d]
9 [h]	n-octyl-OH	N/A	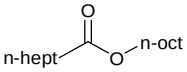	72	63 [i]
10	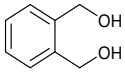	N/A	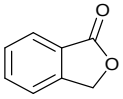	15	90 [j]

[a] Reaction Conditions: Alcohols (0.5 mmol), tandem reagents (1.0 mmol), catalyst (50 mg), toluene (5 mL),110°C, air balloon. [b] Determined by GC-MS based on alcohols as the limiting reagents. [c] Diamine was added after full conversion of aldehydes. [d] The other products were the corresponding aldehydes. [e] Catalyst (100 mg), 400 μL NH_4OH, 5 bar of O_2, 130°C, Acetonitrile as solvent (10 mL). [f] The other products were the corresponding cyanides. [g] 1 eq of K_2CO_3 was used. [h] 4 mL of 1-octanol, no solvent, under air flow. [i] Other products were octyl octanoate (21%), and octyl hexanoate (16%) [j] The other product was phthaldialdehyde.

4.5.4 C-C bond formation

We have successfully employed three different strategies to develop one-pot oxidation/olefination reaction by meso Cs/MnO_x, applicable to aromatic as well as inactive aliphatic alcohols. The first strategy (one pot oxidation/Wittig reaction) is associated with oxidation of alcohols to aldehydes followed by *in situ* reaction of aldehydes with a stabilized Wittig reagent. Using an aromatic (benzyl alcohol) and an aliphatic (1-dodecanol) alcohol as substrates afforded quantitative conversion and high selectivity to the corresponding α,β unsaturated ketones by meso Cs/MnO_x **[Table 4.4, Entry 5 and 6]**. In the second strategy, benzaldehyde was trapped by a base mediated condensation reaction with a ketone (acetophenone) to produce the α,β unsaturated ketone with excellent selectivity (80%) **[Table 4.4, Entry 7]**. The cross coupling procedure was further improved by applying a third strategy, which was the direct oxidation of primary and secondary alcohols followed by a condensation of the *in situ* generated aldehyde and ketone with moderate (20%) selectivity to α,β unsaturated ketones **[Table 4.4, Entry 8]**.

4.5.5 Oxidative esterification

The meso Cs/MnO_x catalyst was also applied to one-pot synthesis of esters by oxidation of alcohols. Unlike other tandem oxidation reactions, addition of a second substrate was not required as the alcohol can itself act as the tandem substrate. We performed oxidation of an aliphatic alcohol (1-octanol) with meso Cs/MnO_x under aerobic conditions. Surprisingly, the reaction yielded three different esters (octyl otanoate (21%), octyl heptanoate (63%) and octyl hexanoate (16%)) [**Table 4.4, Entry 9**]. To date, this kind of multiple esterification from one single alcohol has not been reported. This synthetic strategy has several advantages such as multiple long chain esters can be manufactured

from single alcohols as the only reactant, no precious metals and additives are required, and the reaction can be performed under aerobic conditions.

Table 4.5. Solvent free aerobic oxidation of 1-octanol by different catalysts[a]

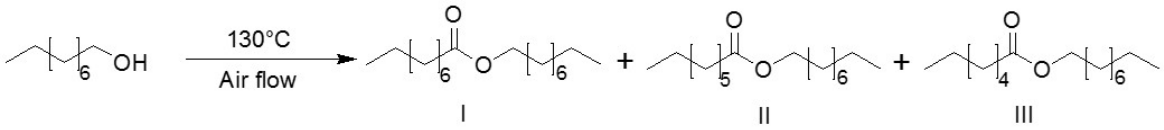

Entry	Catalyst	Conversion (%)	Selectivity (%)		
			I	II	III
1	no	0	nd	nd	nd
2	Comm Mn_2O_3	0	nd	nd	nd
3	K-OMS-2[b]	2	nd	50	25
4	Meso MnO_x	72	26	67	7
5	AMO	42	28	58	14
6	Meso Cs/MnO_x	>99	16	63	21

[a] Reaction condition: 1-octanol (4 mL), catalyst (100 mg), air flow, 130°C, 72 h. [b] The other product was 1-otanal. Nd = not detected.

In order to determine the effectiveness of meso Cs/MnO_x over the conventional highly active manganese oxide based catalysts, we have selected the oxidation of 1-octanol under aerobic and solvent free conditions as the model reaction. The reaction did not proceed in the absence of catalyst **[Table 4.5, Entry 1]**. Similar to catalyst free conditions, commercial nonporous Mn_2O_3 was totally inactive **[Table 4.5, Entry 2]** under the present reaction conditions. The state-of-the-art manganese oxide catalyst for oxidation reactions, K-OMS-2[26], displayed very low activity under identical conditions **[Table 4.5, Entry 3]**. Using bare mesoporous manganese oxide (made by UCT method)[27] and amorphous manganese oxide (AMO)[28] as reference catalysts, much lower conversions were achieved

[Table 4.5, Entry 4, 5]. Meso Cs/MnO_x outperformed all other manganese oxide based catalysts in the oxidative esterification of 1-octanol **[Table 4.5, Entry 6]**.

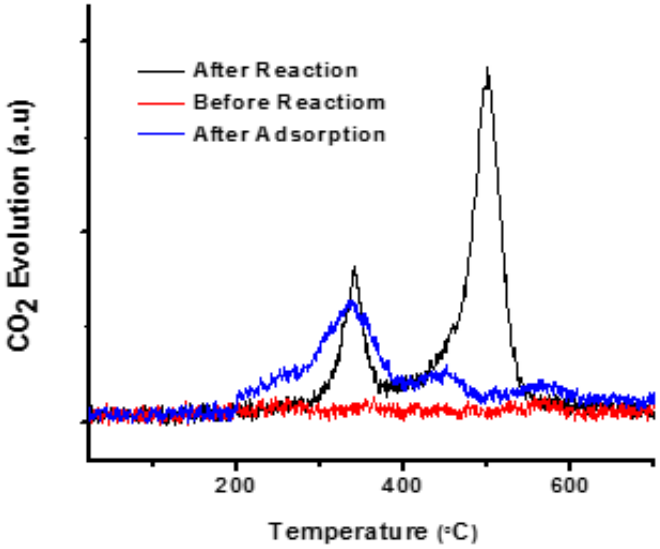

Figure 4.5. CO_2-TPD study A sharp peak of CO_2 (at 500°C) was observed from the material after the reaction, which can be ascribes as the adsorbed CO_2 coming from the reaction due to decarboxylation. Whereas, the material only showed a small peak due to adsorption of the substrate and no CO_2 was evolved from the bare material itself.

Formation of esters with their acidic part bearing less carbons than the parent alcohol indicates a decarboxylation mechanism[29]. To form fewer esters, we selected solvent free oxidation of 2-phenylethanol (one aliphatic CH_2 group) for the mechanistic investigation. The oxidation of 2-phenylethanol led to phenethyl benzoate (the acidic part of the ester has one less carbon than the parent alcohol) as the only ester. We used temperature programmed desorption (TPD) of the used catalyst to detect the CO_2 probably due to decarboxylation of the 2-phenylethanoic acid (by oxidation of 2-phenylethanol). To compare, the bare catalyst and the catalyst after adsorption of 2-phenylethanol at room

temperature were also tested for CO_2-TPD (**Figure 4.5**). The used catalyst displayed two desorption peaks of CO_2 at 340°C and 500°C respectively, whereas no CO_2 desorption was observed for the bare catalyst. On the other hand, the treated catalyst after adsorption displayed only one peak at 335°C. Based on these observations, we propose an oxidation-decarboxylation-oxygen rebound mechanism[30]. The ester production was initiated by the oxidation of alcohol to acid, followed by a decarboxylation with a subsequent oxygen rebound mechanism by a radical intermediate, which generated an aldehyde having one carbon less than the parent alcohol (**Scheme 4.3 and 4.4**). Formation of a trace amount of benzaldehyde and inhibition of reaction by addition of a radical inhibitor (phenothiazine) support our mechanism. The aldehyde was further reacted with the alcohol to yield the desired ester, promoted by the basic nature of meso Cs/MnO_x [31]. The bifunctional nature (oxidative and basic) of the meso Cs/MnO_x is believed to be the reason for the enhanced activity over other manganese oxide based catalysts in oxidative esterification, as esterification is strongly promoted by the basic nature of the catalyst.

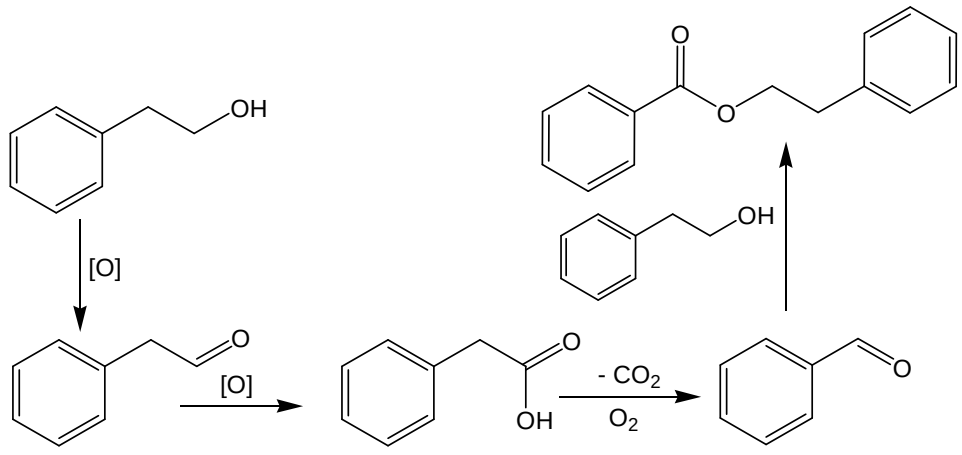

Scheme 4.3. Possible reaction pathways of oxidation of phenethyl alcohol by oxidation-decarboxylation-oxygen rebound mechanism over meso Cs/MnO_x. A trace amount of benzaldehyde was detected by GC-MS.

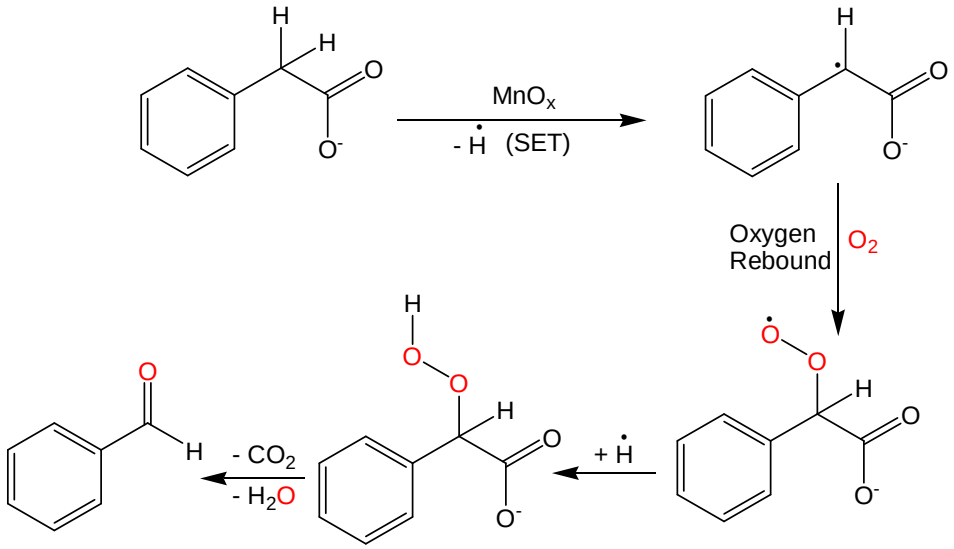

Scheme 4.4. Possible manganese oxide assisted oxygen rebound mechanism. No reaction was observed when a radical inhibitor was added, which confirmed the radical intermediate formation by single electron transfer (SET) mechanism.

The oxidative esterification method was further extended for lactonization of diols. 1,2-benzenedimethanol was converted to the corresponding lactone with excellent conversion (90%) and selectivity (98%) using air as the terminal oxidant **[Table 4.4, Entry 10]**.

4.6 Discussion

Based on the catalytic results discussed above, the meso Cs/MnO_x material can be considered as an efficient catalyst for versatile tandem oxidation reactions. In general, imines are synthesized by two distinct reaction steps from alcohols. The first step involved oxidation of benzyl alcohol to the corresponding benzaldehyde. In the second step, the imine was formed by a nucleophilic condensation of amine with the *in situ* generated

benzaldehyde. The mechanism of oxidation of alcohol by meso Cs/MnO_x was thoroughly investigated in our previous study, where the redox cycle of active manganese centers along with its labile lattice oxygen molecules have been found to be the dominant factors. On the other hand, the condensation between aldehyde and amine is generally very facile due to good electrophilic properties of aldehyde and the nucleophilic nature of the amine. In our study, condensation reactions between benzaldehyde and n-dodecylamine did not require any catalytic assistance. However, synthesis of imines can be difficult when amines with poor nucleophilic nature are used as substrates. In those cases, catalysts with strong coordinating ability (Lewis acidic sites) with the carbonyl oxygen can increase the electrophilic nature of the aldehyde to accelerate the reaction rate. The Mn^{3+} centers of meso Cs/MnO_x can act as coordinating sites in order to facilitate imine formation. This scenario is reinforced by the fact that the condensation between benzaldehyde and a weak nucleophilic amine (4-nitroaniline) was accelerated in the presence of meso Cs/MnO_x.

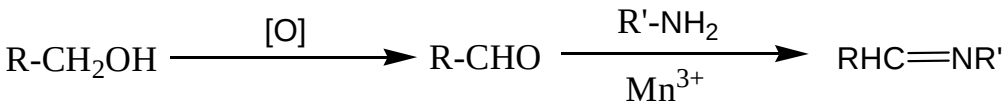

Scheme 4.5. Possible reaction pathways of imine formation from alcohol over meso Cs/MnO_x.

The reaction mechanism was then proposed based on the experimental findings and previous reports (**Scheme 4.5**). First, alcohols were oxidized to corresponding aldehydes in the presence of air, which was subsequently condensed with the amines to form imines catalyzed by coordinating sites of Mn^{3+} centers. Notably, the slower reaction rate of alcohol oxidation (30% conversion in 15 min) than condensation (> 99% conversion in 5 min) indicates that the initial oxidation of alcohol is the rate determining step. Thus, a

cooperation between redox and coordinating sites of the catalyst, plays a key role in determining the activity for not only the oxidation of alcohols to aldehydes but also in the subsequent condensation step for the formation of imines.

The diversity of the one pot imine formation was also shown by broad substrate scope. Our methodology worked well for diverse aromatic and aliphatic alcohol/ amine derivatives. The effectiveness of the catalyst was observed in reaction of heteroatom (S) containing substrates, where a high conversion (>99%) and selectivity (94%) were observed, though heteroatoms are known to poison transition metal centers of the catalyst. The longer reaction time and higher catalyst amount for a sterically hindered alcohol is likely due to difficult abstraction of the benzylic proton caused by the steric hindrance of three adjacent methyl groups. The nucleophilic property of the amine had a significant influence in the reaction. This is supported by the results of very low conversion (40%) of a weakly nucleophilic 4-nitroaniline even after 15 h of reaction, whereas aliphatic amines with high nucleophilic nature gave very high conversion (>99%) and selectivity in 4 h.

4.7 Conclusion

In conclusion, we demonstrated meso Cs/MnO_x as a multifunctional catalyst for versatile tandem oxidation processes. This material was found to be efficient in catalyzing different mechanistically distinct reactions in one-pot under similar conditions. Seven different functional moieties can be evolved from a single substrate (alcohol) by using a single catalyst. Moreover, for the first time we observed multiple esterification from a single alcohol by a single catalyst under aerobic atmospheric conditions. A cooperative effect between different active sites (redox, Lewis acidic, and basic) was found to be the notable feature of the multifunctional meso Cs/MnO_x. The observed catalysis was truly

heterogeneous and the catalyst can be reused without any loss of catalytic performance. Our catalytic protocol provides a new route for sustainable tandem oxidation processes by using an inexpensive material.

4.8 References

(1) Taylor, R. J.; Reid, M.; Foot, J.; Raw, S. A. *Acc. Chem. Res.* **2005**, *38*, 851-869.

(2) Sithambaram, S.; Kumar, R.; Son, Y.-C.; Suib, S. L. *J. Catal.* **2008**, *253*, 269-277.

(3) Sithambaram, S.; Ding, Y.; Li, W.; Shen, X.; Gaenzler, F.; Suib, S. L. *Green Chem.* **2008**, *10*, 1029-1032.

(4) Quesada, E.; Raw, S. A.; Reid, M.; Roman, E.; Taylor, R. J. *Tetrahedron* **2006**, *62*, 6673-6680.

(5) Wang, Y.; Yamaguchi, K.; Mizuno, N. *Angew. Chem., Int. Ed.* **2012**, *51*, 7250-7253.

(6) Yamaguchi, K.; Kobayashi, H.; Wang, Y.; Oishi, T.; Ogasawara, Y.; Mizuno, N. *Catal. Sci. Technol* **2013**, *3*, 318-327.

(7) Monk, K. A.; Siles, R.; Hadimani, M. B.; Mugabe, B. E.; Ackley, J. F.; Studerus, S. W.; Edvardsen, K.; Trawick, M. L.; Garner, C. M.; Rhodes, M. R. *Bioorg. Med. Chem. Lett.* **2006**, *14*, 3231-3244.

(8) Dhakshinamoorthy, A.; Garcia, H. *Chem. Soc. Rev.* **2014**, *43*, 5750-5765.

(9) Jeena, V.; Robinson, R. S. *RSC Adv.* **2014**, *4*, 40720-40739.

(10) Tamura, M.; Tomishige, K. *Angew. Chem., Int. Ed.* **2015**, *54*, 864-867.

(11) Maki, B. E.; Chan, A.; Phillips, E. M.; Scheidt, K. A. *Org. Lett.* **2007**, *9*, 371-374.

(12) Sun, H.; Su, F. Z.; Ni, J.; Cao, Y.; He, H. Y.; Fan, K. N. *Angew. Chem., Int. Ed.* **2009**, *48*, 4390-4393.

(13) Shiraishi, Y.; Sugano, Y.; Tanaka, S.; Hirai, T. *Angew. Chem., Int. Ed.* **2010**, *49*, 1656-1660.

(14) Ruiz, V. R.; Corma, A.; Sabater, M. J. *Tetrahedron* **2010**, *66*, 730-735.

(15) Verhaak, M.; Van Dillen, A.; Geus, J. *Catal. Lett.* **1994**, *26*, 37-53.

(16) Kwon, M. S.; Kim, N.; Seo, S. H.; Park, I. S.; Cheedrala, R. K.; Park, J. *Angew. Chem.* **2005**, *117*, 7073-7075.

(17) Shimizu, K. i.; Sato, R.; Satsuma, A. *Angew. Chem.* **2009**, *121*, 4042-4046.

(18) Fischer, A.; Makowski, P.; Müller, J. O.; Antonietti, M.; Thomas, A.; Goettmann, F. *ChemSusChem* **2008**, *1*, 444-449.

(19) Dixit, M.; Mishra, M.; Joshi, P. A.; Shah, D. O. *Catal. Commn.* **2013**, *33*, 80-83.

(20) Otera, J.; Nishikido, J. *Esterification: methods, reactions, and applications*; John Wiley & Sons, 2009.

(21) Jagadeesh, R. V.; Junge, H.; Pohl, M.-M.; Radnik, J. r.; Brückner, A.; Beller, M. *J. Am. Chem. Soc.* **2013**, *135*, 10776-10782.

(22) Wang, L.; Li, J.; Dai, W.; Lv, Y.; Zhang, Y.; Gao, S. *Green Chem.* **2014**, *16*, 2164-2173.

(23) Preston, P. *Chem. Rev.* **1974**, *74*, 279-314.

(24) Raghavendra, G. M.; Ramesha, A. B.; Revanna, C. N.; Nandeesh, K. N.; Mantelingu, K.; Rangappa, K. S. *Tetrahedron Lett.* **2011**, *52*, 5571-5574.

(25) Biswas, S.; Dutta, B.; Mullick, K.; Kuo, C.-H.; Poyraz, A. S.; Suib, S. L. *ACS Catal.* **2015**, *5*, 4394-4403.

(26) Son, Y. C.; Makwana, V. D.; Howell, A. R.; Suib, S. L. *Angew. Chem.* **2001**, *113*, 4410-4413.

(27) Poyraz, A. S.; Kuo, C.-H.; Biswas, S.; King'ondu, C. K.; Suib, S. L. *Nat. Commun.* **2013**, *4*, 2952.

(28) Cao, H.; Suib, S. L. *J. Am. Chem. Soc.* **1994**, *116*, 5334-5342.

(29) Feng, Q.; Song, Q. *J. Org. Chem.* **2014**, *79*, 1867-1871.

(30) Mukherjee, A.; Angeles-Boza, A. M.; Huff, G. S.; Roth, J. P. *J. Am. Chem. Soc.* **2010**, *133*, 227-238.

(31) Biswas, S.; Poyraz, A. S.; Meng, Y.; Kuo, C.-H.; Guild, C.; Tripp, H.; Suib, S. L. *Appl. Catal., B: Environ.* **2015**, *165*, 731-741.

CHAPTER 5. Mesoporous Copper/Manganese Oxide-Catalyzed Coupling of Alkynes: Evidence for Synergistic Cooperative Catalysis

5.1 Abstract

Copper oxide supported on mesoporous manganese oxide (meso Cu/MnO_x) was synthesized by an inverse micelle templated evaporation induced self-assembly procedure. An aggregation of nanoparticle and monomodal mesoporous size distribution with tunable structural properties were observed. Evidence of incorporation of copper in the form of oxide on the manganese oxide surface was detected by performing structural parameter refinements and supported by other characterization techniques such as SEM, TEM, EDX and XPS. A homogeneous distribution of copper oxide on manganese oxide surface was suggested by TEM-EDX studies. The material possessed superior catalytic activity in aerobic oxidative coupling of terminal alkynes. Excellent conversion (>99 % in most cases) and selectivity were observed in both homo and cross-coupling of alkynes using the best optimized reaction condition. Use of air as sole oxidant, avoidance of any kind of additives, ease of product separation, great functional group tolerability, wide synthetic scope and superior reusability (up to 8^{th} cycle) are the notable features of our catalytic protocol. While elucidating the reaction mechanism, we established a synergistic cooperative effect between the copper and manganese to be responsible for superior catalytic activity. The labile lattice oxygen of the meso Cu/MnO_x played a vital role in deprotonation of alkyne proton as supported from the TPD studies. Moreover, for the first time, we designed model complexes for the active sites of the catalyst by DFT calculations and provided a qualitative description of the coupling mechanism, which supported the experimental findings.

5.2 Background and significance

1,3-diyne motif is encountered in numerous natural products with prominent biological activities such as antibacterial, antimicrobial, antifungal, antitumor, anticancer, anti-HIV, and pesticidal properties[1]. Rigid and sterically undemanding acetylenic moieties pursue interesting electronic and optical properties due to the presence of extensive π conjugation. 1,3-diyne derivatives are also utilized in supramolecular chemistry, designing of advanced conjugated polymeric and optical materials, molecular wires, and liquid crystals[2,3]. Pioneered by Glaser in 1869, using stoichiometric amounts of copper salt, oxidative homo-coupling of terminal alkynes was considered as the most straightforward route for synthesizing diyne molecules[4]. Since then, many ligand/metal salt combinations have been reported for alkyne coupling under homogeneous and mild reaction conditions[5-8]. From the viewpoint of green and environmental aspect, heterogeneous catalysts are more advantageous over the homogeneous systems owing to easy separation, recyclability and high stability[9-11]. In this context, palladium based immobilized heterogeneous systems have been successfully used[12-14]. However, high price of palladium, tedious synthesis methodology and use of copper as co-catalyst in some cases hinder their practical applications.

Copper based heterogeneous catalysts, in particular supported copper catalysts are specifically attractive, since they provide similar or higher performance than palladium even with lower loading of copper[15-22]. Nevertheless, these catalysts often lacked reusability, required molecular oxygen or other chemical oxidant, high copper loading and assistance of base and ligand was indispensable for achieving high efficiency[23-26]. In addition, cross-coupling of two different terminal alkynes yet remains a challenging issue

because of a competing homo-coupling reaction.[11,27] Peng et al. reported a gold catalyzed alkyne cross-coupling protocol with high selectivity towards unsymmetrical diynes[28]. However, assistance of nitrogen based ligand was identified as a crucial factor to promote the transformation. Therefore, considering the afore-mentioned disadvantages, designing of a copper based heterogeneous catalyst for alkyne coupling reaction is highly desirable, which ideally involves air as the terminal oxidant, avoidance of any kind of additives, low catalyst loading, proper reusability and high activity towards synthesis of symmetrical and asymmetrical diyne derivatives .

Despite wide synthetic applicability, current understanding of the exact mechanism of the copper mediated alkyne coupling reaction remains unsatisfactory[5]. In between several existing hypotheses, the mechanism proposed by Bohlmann et al. is considered as the most reasonable and acceptable among those[29]. Based on their understanding, initially, a π co-ordination species between triple bond and copper (I) was established, which further formed a dinuclear copper (II) acetylide species, and essentially collapsed to give the coupled product. However, considered as an oxidative reaction, little has been discussed about the role of dioxygen in the mechanistic details. In spite of some efforts to describe the copper mediated coupling reaction mechanism by computational techniques, proper designing of catalytic active sites has not been made[30-32]. Moreover, the proposed mechanisms were specific for particular reaction conditions and a correlation between the theoretical and experimental results has been scarcely established. Therefore, a complete mechanism of the copper mediated oxidative coupling reaction emphasizing the role of dioxygen must be discussed in detail, since a simple alkyne coupling reaction can be used as a benchmark for other oxidative complex coupling reactions.

Synergistic–cooperative catalysis involving two metals is an exciting phenomenon in those organic transformations which cannot be accomplished by individual metal catalyst[33,34]. Joint participation of dual metals having distinctive properties is often required for acquiring high activity. The biggest challenge in this field is to exploit the relative compatibility of the two metals in the same reaction medium. Mizuno et al described a synergistic catalytic system for alkyne homo-coupling reaction using copper hydroxide on manganese oxide-octahedral molecular sieves ($Cu(OH)_x$/OMS-2)[15]. Manganese oxide acted as an electron mediator between dioxygen and copper to re-oxidize the reduced copper species after the coupling reaction. They mentioned that the presence of hydroxyl species was indispensable for the abstraction of alkyne protons. However, the catalyst was designed conceptually and no clear understanding of the active sites has been provided. Basic pretreatment, use of molecular oxygen, and high catalyst loading for aliphatic alkynes are considered as drawbacks for the methodology. It is also difficult to estimate if cross-coupling of alkynes would be obtained with similar efficiency like homo-coupling, since no example of cross-coupling has been mentioned.

Herein, we designed mesoporous manganese oxide supported copper oxide for oxidative homo and cross-coupling of alkynes to 1,3-diyne derivatives. Use of air as the terminal oxidant, no pretreatment by basic additives, high turnover numbers, proper reusability, and high functional group tolerability make our catalytic protocol superior to existing catalytic systems. The mechanistic pathways and kinetic analysis were studied in detail. Additionally, we performed density functional theory (DFT) computational techniques in order to establish a correlation with the experimental results towards

disclosing the active catalytic centers and determined the role of manganese and labile lattice oxygen towards the activity.

5.3 Experimental Section

5.3.1 Synthesis of mesoporous Cu/MnO_x

The synthesis was performed following the synthetic procedure of University of Connecticut (UCT) mesoporous materials[35]. Copper nitrate trihydrate ($Cu(NO_3)_2.3H_2O$) was selected as the dopant source in the synthesis. In a 120 mL beaker, 0.02 mol of manganese nitrate tetrahydrate ($Mn(NO_3)_2.4H_2O$), different amounts of $Cu(NO_3)_2.3H_2O$, and (0.134 mol) 1-butanol were added. To this solution (0.0034 mol) P123 ($PEO_{20}PPO_{70}PEO_{20}$, molar mass 5750 g mol^{-1}) and (0.032 mol) concentrated nitric acid (HNO_3) were added and stirred at room temperature until the solution became clear. The resulting clear blue solution was then kept in an oven at 120°C for 3 h under air. After reaction, the black material was washed with excess ethanol, centrifuged, and dried in a vacuum oven overnight. The dried black powder was then subjected to a heat treatment of 150°C for 12 h, cooled to room temperature, followed by heating at 250°C for 3 h under air (named as meso Cu/MnO_x).

5.3.2 Catalyst Characterization

The powder X-Ray diffraction (PXRD) data were collected with a Rigaku Ultima IV diffractometer (Cu Kα radiation, λ=1.5406 Å) with an operating voltage of 40 kV and a current of 44 mA. The low-angle PXRD patterns were collected over a 2θ range of 0.5–10° with a continuous scan rate of 0.5° min^{-1}, where the wide-angle PXRD patterns were collected over a 2θ range of 5–75° with a continuous scan rate of 1.0° min^{-1}. The nitrogen

adsorption desorption experiments were performed with a Quantachrome Autosorb-1-1C automated adsorption system. The samples were treated at 150°C for 6 h under helium prior to measurement. The surface areas and pore sizes (from the desorption branch of isotherm) were measured by the Brunauer–Emmett–Teller (BET) and the Barrett–Joyner–Halenda (BJH) methods. The surface morphology was determined by a Zeiss DSM 982 Gemini field emission scanning electron microscope (FE-SEM) with a Schottky emitter at an accelerating voltage of 2.0 kV having a beam current of 1.0 mA. Transmission electron microscopy (TEM) experiments were carried out on a JEOL 2010 FasTEM microscope with an operating voltage of 200 kV. The samples were prepared by casting the suspension of material on a carbon coated copper grid. The X-ray photoelectron spectroscopy (XPS) studies were performed with a PHI model 590 spectrometer with multiprobes (ΦPhysical Electronics Industries Inc.), using Al-K alpha radiation (λ= 1486.6 eV) as the radiation source. The curves were fitted using CasaXPS software (version 2.3.12). The powder samples were pressed on carbon tape mounted on adhesive copper tape stuck to a sample stage placed in the analysis chamber. For correction of surface charging, the C 1s photoelectron line at 284.6 eV was taken as a reference. A mixture of Gaussian (70%) and Lorentzian (30%) functions was used for the least-squares curve fitting procedure. The temperature programmed desorption (TPD) experiments were performed with a Thermolyne 79300 model tube furnace equipped with an MKS gas analyzer coupled with a quadrupole mass selective detector. The samples were treated with Ar for 2 h at 250°C before the experiments. In the experiments Ar as a carrier gas was used at a constant flow rate in the temperature range 50°C to 600°C at a ramp of 10°C min^{-1}. Inductively coupled

plasma optical emission spectrometer (ICP-OES) was performed with a Perkin Elmer Optima 7300DV instrument.

5.3.3 Homo-coupling of terminal alkynes

In a typical homo-coupling reaction, alkyne (0.5 mmol), meso Cu/MnO_x (6 mol % with respect to alkyne) and toluene (5 mL) were put in a 25 mL round bottom flask (two necked flask for time dependent study, where the second neck was used as a sample port). The flask with the reaction mixture with a reflux condenser attached was immersed in a silicone oil bath preheated to 105°C. The reaction mixture was refluxed under vigorous stirring (700 rpm) for the required time under an air balloon. After reaction, the mixture was cooled, the catalyst was removed by filtration, and gas chromatography – mass spectra (GC-MS) was used to analyze the filtrate. The conversions were determined based on concentration of alkynes. The selectivity was calculated based on diyne as the only product. The products were isolated with silica gel column chromatography (n-hexane or a mixed solvent of n-hexane and dichloromethane was used as an eluent). Data of diynes are summarized in the supporting information.

5.3.4 Hetero-coupling of terminal alkynes

In a typical cross-coupling reaction, alkynes with the required molar amounts, meso Cu/MnO_x (6 mol % with respect to total alkyne amount), and toluene (5 mL) were put in a 25 mL round bottom flask. The flask with the reaction mixture with a reflux condenser attached was immersed in a silicone oil bath preheated to 105°C. The reaction mixture was refluxed under vigorous stirring (700 rpm) for the required time under an air balloon. After

reaction, the mixture was cooled, the catalyst was removed by filtration, and GC-MS was used to analyze the filtrate. The conversions were determined based on the concentration of limiting alkynes.

5.3.5 Analysis of reaction products of alkyne coupling

The gas chromatography – mass spectra (GC-MS) analyses were performed by a 7820A GC system connected with a thermal conductivity detector of 5975 series MSD from Agilent Technologies and a nonpolar cross-linked methyl siloxane column with dimensions of 12 in × 0.200 mm × 0.33 µm. The ^{1}H and ^{13}C nuclear magnetic resonance (NMR) spectra were recorded on a Bruker AVANCE III- 400 MHz spectrometer. ^{1}H NMR spectra were collected at 400 MHz with chemical shift referenced to the residual peak in $CDCl_3$ (δ: H 7.26 ppm). ^{13}C NMR spectra were collected at 100 MHz and referenced to residual peak in $CDCl_3$ (δ: C 77.0 ppm). Multiplicities are written as s (singlet), d (doublet), t (triplet), and m (multiplet).

5.4 Structural characterization of meso Cu/MnO_x

The Cu incorporated mesoporous manganese oxide (meso Cu/MnOx) was characterized extensively by various techniques including powder X-ray diffraction (PXRD), nitrogen sorption, scanning electron microscopy (SEM), transmission electron microscopy (TEM), energy dispersive X-ray spectroscopy (EDXS) and X-ray photoelectron spectra (XPS). A typical ordered mesoporous UCT material has a diffraction line in the low angle (0.5° - 8°) region of PXRD pattern, which indicates the existence of a mesostructure. **Figure 5.1A** displayed the low angle diffraction pattern of meso Cu/MnO_x with different concentrations

of Cu. All the meso Cu/MnO_x material exhibited the characteristic low angle peak irrespective of the dopant amount. A change of crystallinity with the Cu incorporation was observed in the wide angle (5° - 75°) diffraction patterns of the meso Cu/MnO_x (**Figure 5.1B**). No diffraction peaks were observed in the wide angle PXRD pattern for the 1% and 5% incorporation of Cu in the meso MnO_x. 10% meso Cu/MnO_x revealed diffraction peaks corresponding to CuO, but no diffraction peaks were observed for the MnO_x. This indicates a poorly crystalline nature of manganese oxide at this calcination temperature (250°C). A Type-IV adsorption isotherm followed by a Type –I hysteresis loop was observed in the N_2 sorption studies (**Figure 5.1C**). The surface areas were calculated as 227 – 290 m^2g^{-1} (by Brunauer–Emmett–Teller (BET) methods) and 1% Cu containing sample exhibited the highest surface area of 290 m^2g^{-1} (**Table 5.1**). The Barrett-Joyner-Halenda (BJH) adsorption pore size distribution (**Figure 5.1D**) indicated a narrow monomodal pore size distribution for all the Cu containing materials. The pore diameters (**Table 1**) are within the mesoporous range (3.0 – 3.4 nm).

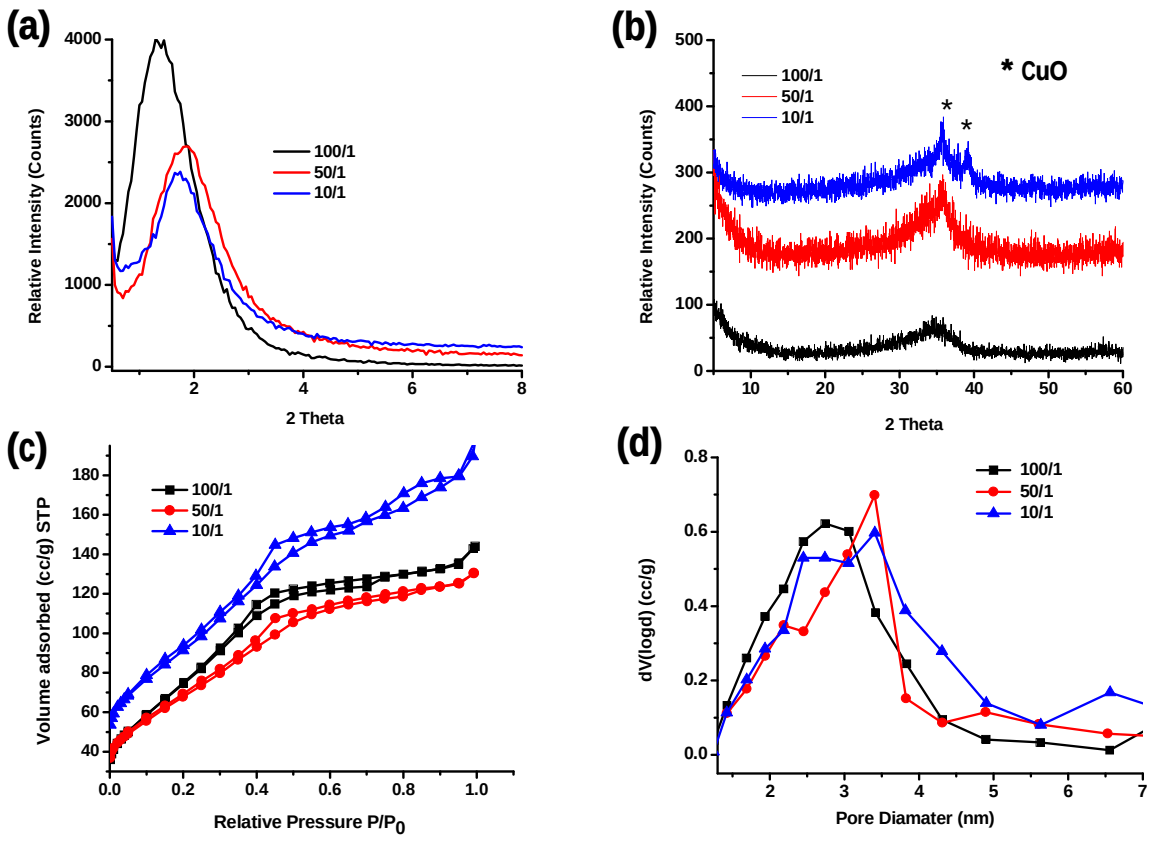

Figure 5.1 Structural characterization of meso Cu/MnO_x with different Mn/Cu molar ratio. PXRD patterns (A) Low angle (0.5° -8°), (B) Wide angle (5°-75°), (C) Nitrogen sorption isotherms and (D) BJH adsorption pore size distributions.

Table 5.1 Structural parameters of meso Cu/MnO_x

Mn/Cu molar ratio	Surface Area S_{BET} (m^2g^{-1})	BJH ads. pore size (nm)	Pore volume (cc g^{-1})	EDX Cu mol %	Crystal Structure (PXRD)
n/a	200	2.8	0.153	n/a	Amorphous
100/1	290	2.9	0.244	1.0	Amorphous
50/1	227	3.4	0.202	3.8	Amorphous
10/1	270	3.4	0.301	6.0	CuO

n/a = not applicable.

The morphological features of meso Cu/MnO_x were studied by field emission scanning electron microscope (FE-SEM) and have a various Cu loadings (**Figure 5.2**). The materials are composed of aggregated micron-sized rounded nanoparticles. Random packing of metal oxide particles was also observed by Transmission electron microscopy (TEM) (**Figure 5.3)** of 10% meso Cu/MnO_x material. Energy dispersive X-ray spectroscopy (EDX) was used to analyze the concentration of each element in the material (**Table 5.1**). The high resolution TEM-EDX elemental map analyses of Mn, Cu, and O (**Figure 5.3)** indicate a homogeneous distribution of CuO over the MnO_x nanoparticle throughout the material.

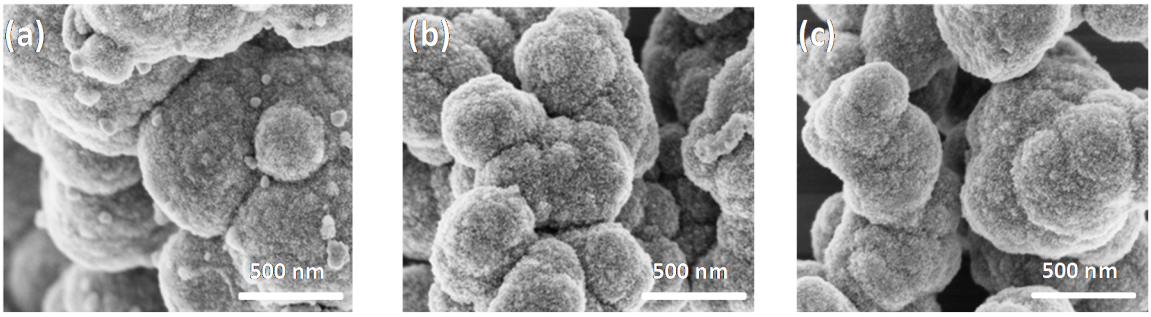

Figure 5.2 The FE-SEM images of meso Cu/MnO_x with different Mn/Cu molar ratio (a) 100/1, (b) 50/1 and (c) 10/1.

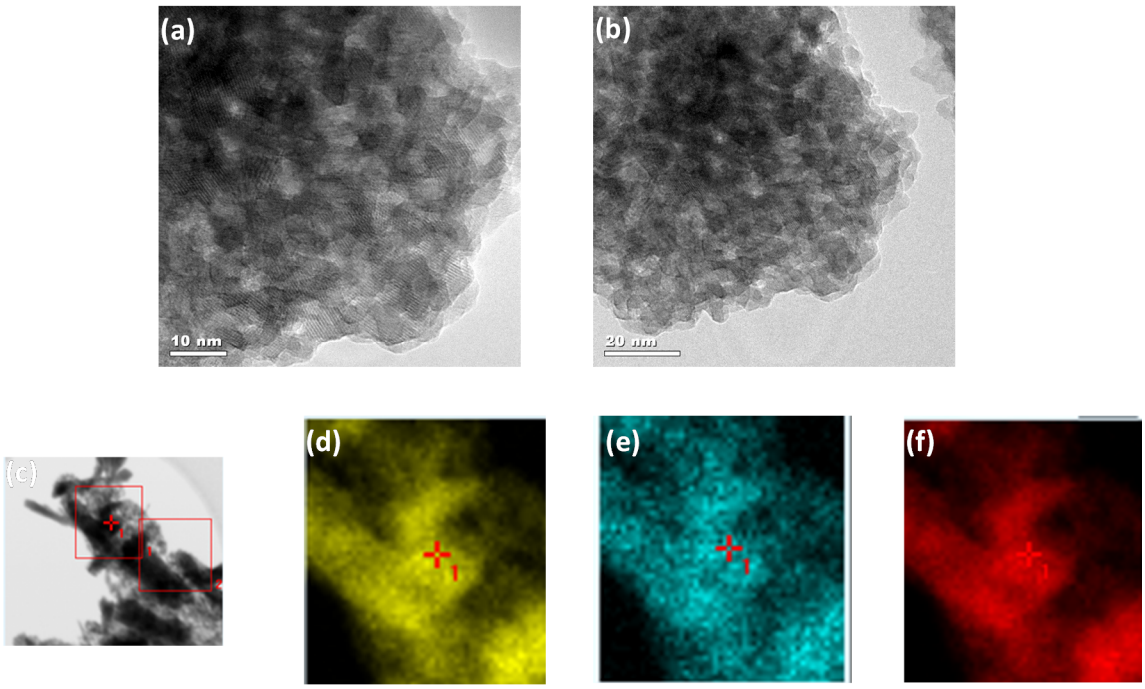

Figure 5.3 (a, b and c) The TEM images and TEM-EDX elemental maps (d) Mn-L, (e) Cu-L and (f) O-L of meso Cu/MnO_x with Mn/Cu molar ratio 10/1.

In the case of metal oxide mediated oxidative reactions, oxidation states of active metals, and the nature of surface oxygen species are two important parameters to be considered. A Cu $2p_{3/2}$ binding energy of 933.3 eV and the presence of shake up satellite peaks from X-ray photoelectron spectra (XPS) studies confirmed the oxidation state of Cu as $2+$[15], which is in agreement with the PXRD data (**Figure 5.4a, Table 5.2**). The Mn 2p XPS signal consists of two peaks, which were assigned as Mn $2p_{3/2}$ and Mn $2p_{1/2}$ core levels (**Figure 5.4b**). The binding energies of 641.5 eV and 653.2 eV can be attributed to the Mn^{3+} oxidation state[36]. On the other hand, deconvolution of O 1s spectra (**Figure 5.4c**) specified the existence of three different binding oxygen species, namely, structural or lattice oxygen (O_s), surface adsorbed oxygen (O_{ads}), and adsorbed water or hydroxyl groups (O_{mw}). In comparison to the reference catalyst (meso MnO_x), a shift of the O 1s peak at

lower binding energy (530.2 eV in meso MnO_x and 529.2 eV in meso Cu/MnO_x) was observed (**Figure 5.4d**). This signifies an increase of mobility of lattice oxygen due to copper incorporation. The deconvolution O 1s spectra also suggest a predominance of lattice oxygen (O_s) near the surface of the catalyst.

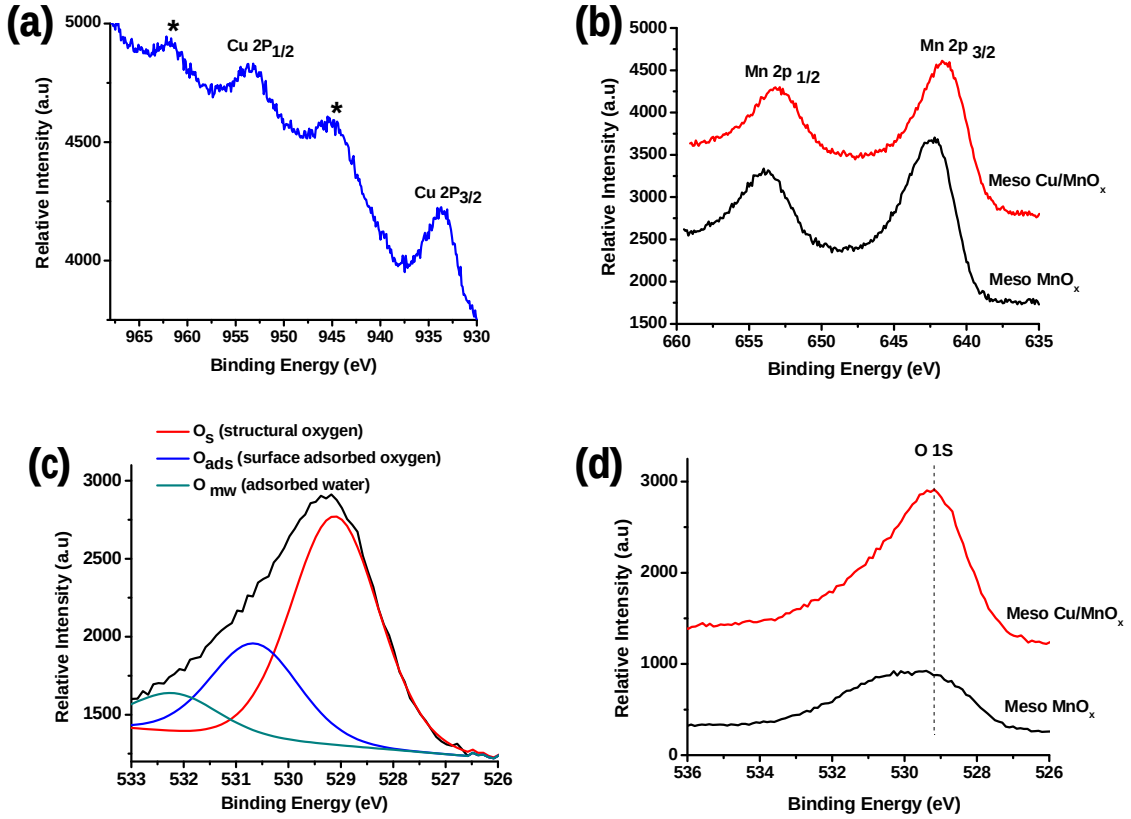

Figure 5.4 XPS of meso Cu/MnO_x (10% Cu): (a) Cu 2p (* indicates the shake up satellite peaks), (b) Mn 2p, (c) deconvoluted O 1s and (d) comparison of the O 1s transitions of meso Cu/MnO_x and meso MnO_x.

Table 5.2 Comparion of XPS of Mn 2p and O 1s signal

Materials	Cu (eV)		Mn (eV)		O_s (eV)		O_{ads} (eV)		O_{mw} (eV)	
	$2p_{3/2}$	$2p_{1/2}$	$2p_{3/2}$	$2p_{1/2}$	BE	% A	BE	% A	BE	%A
Meso Cu/MnO_x	933.3	953.2	641.5	653.2	529.1	63.2	530.6	23.2	532.2	10.6
Meso MnO_x	n/a	n/a	641.4	652.8	529.0	47.5	530.8	40.5	532.4	12.0

O_s = Structural or lattice oxygen, O_{ads} = surface adsorbed oxygen, O_{mw} = adsorbed water or hydroxyl group. n/a = not applicable.

5.5 Catalytic reactions

5.5.1 Optimization of reaction condition

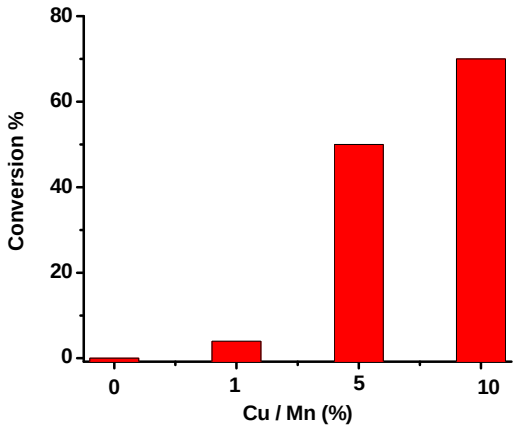

Figure 5.5 Effect of copper loading in catalytic activity. Reaction condition: phenylacetylene (1.0 mmol), meso Cu/MnO_x (50 mg), toluene (5 mL), 105°C, 3 h, under air balloon.

We started the initial investigation by selecting oxidative homo-coupling of phenylacetylene as the model reaction for developing the optimal reaction conditions. The bare mesoporous manganese oxide was totally inactive suggesting presence of no active sites for the coupling reaction. An increase of conversion from 4 to 70% was observed by

increasing the copper concentration from 1% to 10% in the MnO_x (**Figure 5.5**). The selectivity in all the cases were 100% as 1,3-diyne was the only product. Changing the oxidant source from air (45% conversion) to oxygen (55% conversion) resulted in an increase of activity [**Entry 1 and 2, Table 5.3**], whereas, reaction under nitrogen atmosphere displayed much lower conversion (24%) [**Entry 3, Table 5.3**]. A significant enhancement of conversion (70%) was achieved by addition of base [**Entry 4, Table 5.3**] and the combination of oxygen and base displayed the best (85% conversion) activity [**Entry 5, Table 5.3**]. On the other hand, the reaction did not proceed at all in the presence of an acid [**Entry 6, Table 5.3**]. However, performing catalytic reaction under aerobic conditions without any additives is much more desirable in terms of green and sustainable chemistry. While performing further optimizations, an increment of catalyst loading from 3 to 6 mol% with respect to alkyne yielded the desired diyne quantitatively within 40 min (TOF 24.7) [**Entry 8-9, Table 5.3**] without any additives under an air balloon. The reaction also proceeded under nitrogen, though having a much lower TOF value of 3.9 [**Entry 10, Table 5.3**]. Therefore the best optimized reaction conditions [**Entry 9, Table 5.3**] were used for the rest of the work.

Table 5.3 Optimization of reaction conditions[a]

Entry	Cu (mol%)	Oxidant	Additives	Time (min)	Conversion[b] (%)	TOF[c] (h^{-1})
1	3	Air	None	180	45	3
2	3	O_2	None	180	55	6
3	3	N_2	None	180	24	2.7
4	3	Air	K_2CO_3[d]	180	70	7.8
5	3	O_2	K_2CO_3[d]	180	85	9.4
6	3	Air	PTSA[e]	180	0	0
7	3	Air	None	360	80	8.9
8	6	Air[f]	None	45	94	21
9	6	Air	None	40	>99	24.7
10	6	N_2	None	180	70	3.9

[a] Reaction conditions: phenylacetylene (0.5 mmol), catalyst (different mol% of meso Cu/MnO_x), toluene (5 mL), balloon of air/O_2/N_2 , 105°C. [b] Conversions were determined by GC-MS and based on phenylacetylene. [c] TOF = TON/ time (h), TON = no of moles of phenylacetylene converted per mol of Cu in the catalyst. [d] 1 equivalent of K_2CO_3 was used. [e] PTSA (p-Toluenesulfonic acid, 1 equivalent). [f] Open to atmosphere.

The catalyst precursor $Cu(NO_3)_2$. $2H_2O$ and other Cu salts (CuCl, $CuCl_2$, $CuSO_4.5H_2O$) [**Entry 1-4, Table 5.4**] and commercial Cu oxide (CuO, Cu_2O) [**Entry 5-6, Table 5.4**] did not produce any coupling product. No reaction proceeded with a physical mixture of CuO and meso MnO_x [**Entry 7, Table 5.4**]. To determine the role of MnO_x in the reaction, we selected mesoporous Cu/TiO_2 (prepared by the same UCT method, see supporting information for details) as a reference catalyst for comparison. In contrast to meso Cu/MnO_x (>99 % conversion), meso Cu/TiO_2 displayed much lower conversion (7 %) [**Entry 8-9, Table 5.4**], under identical conditions. No reaction happened in the absence of catalyst [**Entry 10, Table 5.4**]. Therefore, the highly dispersed copper oxide species on

mesoporous manganese oxide is indispensable for the present aerobic oxidative coupling of terminal alkynes.

Table 5.4 Oxidative homo-coupling of phenyl acetylene by different catalysts[a]

Entry	Catalyst	Cu (mol%)	Conversion[b] (%)
1	$Cu(NO_3)_2$	6	nd
2	CuCl	6	nd
3	$CuCl_2.2H_2O$	6	nd
4	$CuSO_4.5H_2O$	6	nd
5	CuO	6	nd
6	Cu_2O	6	nd
7[c]	CuO + meso MnO_x	6	nd
8	meso Cu/TiO_2	6	7
9	meso Cu/MnO_x	6	>99
10	None	0	nd

[a] Reaction conditions: phenylacetylene (0.5 mmol), catalyst (6mol% Cu with respect to phenylacetylene), toluene (5 mL), air balloon, 105°C, 45 min. [b] Conversions were determined by GC-MS and based on phenylacetylene [c] A physical mixture of meso MnO_x (50 mg) and CuO (6 mol%) were used. Nd = not determined.

5.5.2 Oxidative homo-coupling of terminal alkynes

5.5.2.1 Substrate scope

The methodology worked well for diverse alkyne derivatives such as aromatic **[Entry 1-8 and 13, Table 5.5]**, aliphatic **[Entry 9-12, Table 5.5]**, heterocyclic **[Entry 8, Table 5.5]**, olefinic **[Entry 7, Table 5.5]**, and silylic **[Entry 10, Table 5.5]**. In all cases, the reaction exhibited >99% selectivity, as the corresponding 1,3-diyne was the only observed product. Alkynes with electron releasing **[Entry 2-4, Table 3]** or electron withdrawing **[Entry 5-6, Table 5.5]** groups reacted smoothly to give the corresponding

1,3-diynes with excellent yields. The position of the methyl group in the aromatic ring did not affect the reaction rate **[Entry 3-4 Table 5.5]**. No dehalogenated product was observed in the case of halogen substituted alkynes **[Entry 5-7, Table 5.5]**. The dimerization of a heterocyclic substituted alkyne **[Entry 8, Table 5.5]** was conducted to afford high yield and selectivity but a much longer reaction time (12 h) was required. Excellent activity (>99% conversion, >99% selectivity) in oxidative coupling of an enyne (1-ethynylcyclohexene) **[Entry 9, Table 5.5]** revealed the superior chemo-selectivity nature of the meso Cu/MnO_x, since no reaction at the double bond was identified by GC-MS. Moreover, aliphatic alkynes were successfully converted to the corresponding diynes with similar turnover numbers (16.7) to the aromatic alkynes **[Entry 10-11, Table 5.5].** Great functional group tolerability was also observed with silylated alkyne **[Entry 12, Table 5.5]** and substrates containing reactive ester groups **[Entry 13, Table 5.5]**.

Table 5.5 Aerobic oxidative homo-coupling of terminal alkynes[a]

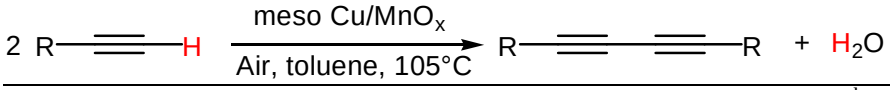

Entry	Substrate	Time (h)	Conversion[b, c] (%)
1	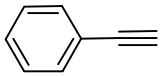	1	>99(97)
2	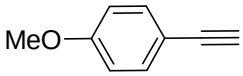	3	>99(85)
3	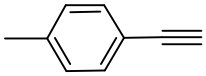	2	>99(83)
4	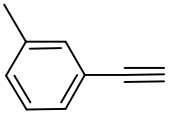	2	>99(91)
5	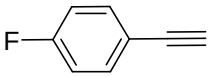	1	>99(98)
6	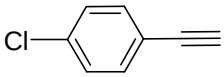	8	90(82)[d]
7	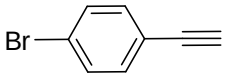	6	95(87)[e]
8	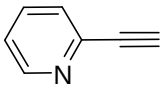	12	>99(85)
9	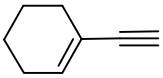	2	>99(91)
10	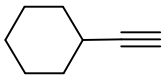	2	>99(82)
11	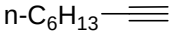	6	>99(87)
12	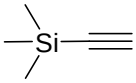	2	>99(93)
13	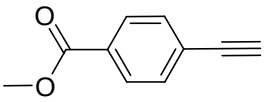	4	>99(96)

[a] Reaction conditions: alkynes (0.5 mmol), meso Cu/MnO_x (6 mol% Cu with respect to amount of alkyne), toluene (5 mL), 105°C, air balloon. [b] Conversion was determined by GC-MS based on the concentration of alkynes. Selectivity in all cases were 100% to diynes. Numbers in parenthesis refer to yields of isolated products. [c] TON (no. of moles of alkynes converted / moles of copper in catalyst) = 16.7. [d] TON = 15.0, [e] TON = 15.8.

5.5.2.2 Charecterization of diynes

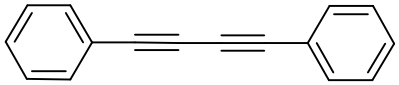

1,4-Diphenyl buta-1,3-diyne

^{1}H NMR (400 MHz, Chloroform-*d*): δ (ppm) = 7.60 – 7.50 (m, 4H), 7.37 (q, *J* = 5.5 Hz, 6H).
^{13}C NMR (101 MHz, Chloroform-*d*): δ (ppm) = 132.66, 129.36, 128.59, 121.96, 81.70, 74.06.

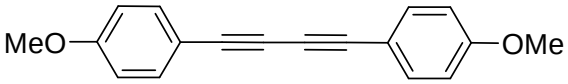

1,4-Bis(4-methoxylphenyl) buta-1,3-diyne

^{1}H NMR (400 MHz, Chloroform-*d*): δ (ppm) = 7.36 (d, *J* = 8.8 Hz, 4H), 6.75 (d, *J* = 8.8 Hz, 4H), 3.72 (s, 6H).
^{13}C NMR (101 MHz, Chloroform-*d*): δ (ppm) = 160.39, 134.18, 114.28, 114.10, 81.38, 73.10, 55.48.

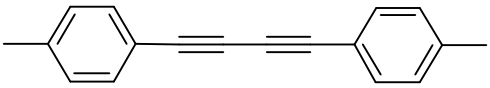

1,4-Bis(4-methylphenyl) buta-1,3-diyne

^{1}H NMR (400 MHz, Chloroform-*d*): δ (ppm) = 7.42 (d, *J* = 8.0 Hz, 4H), 7.14 (d, *J* = 7.9 Hz, 4H), 2.37 (s, 6H).
^{13}C NMR (101 MHz, Chloroform-*d*): δ (ppm) = 139.63, 132.53, 129.35, 118.95, 81.69, 73.61, 21.75.

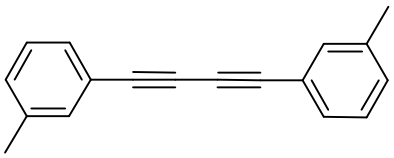

1,4-Bis(3-methylphenyl) buta-1,3-diyne

^{1}H NMR (400 MHz, Chloroform-*d*): δ (ppm) = 7.29 (d, *J* = 7.9 Hz, 4H), 7.16 (m, *J* = 15.3, 7.6 Hz, 4H), 2.29 (s, 6H).
^{13}C NMR (101 MHz, Chloroform-*d*): δ (ppm) = 138.30, 133.12, 130.25, 129.76, 128.46, 121.80, 81.76, 73.81, 21.34.

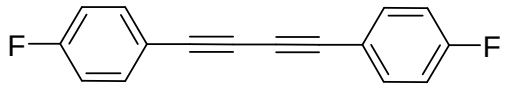

1,4-Bis(4-fluorophenyl) buta-1,3-diyne

^{1}H NMR (400 MHz, Chloroform-*d*): δ (ppm) = 7.51 (dd, *J* = 8.9, 5.4 Hz, 4H), 7.04 (t, *J* = 8.7 Hz, 4H).
^{13}C NMR (101 MHz, Chloroform-*d*): δ (ppm) = 164.47, 161.97, 134.73, 134.64, 118.00, 116.17, 115.95, 80.59, 73.70.

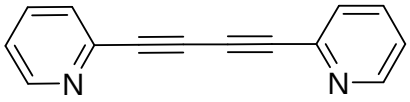

2-(4-(pyridin-2-yl)buta-1,3-diynyl)pyridine

^{1}H NMR (400 MHz, Chloroform-*d*) δ 8.77 (d, *J* = 2.1 Hz, 2H), 8.60 (dd, *J* = 5.0, 1.7 Hz, 2H), 7.81 (dt, *J* = 8.0, 2.0 Hz, 2H), 7.29 (dd, *J* = 7.9, 4.9 Hz, 2H).
^{13}C NMR (101 MHz, Chloroform-*d*): δ (ppm) = 153.15, 149.49, 139.41, 123.11, 118.88, 79.17.

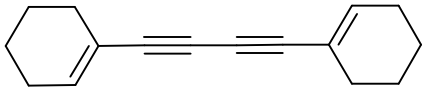

1,4-dicyclohexenylbuta-1,3-diyne

^{1}H NMR (400 MHz, Chloroform-*d*) δ 6.21 (s, 2H), 2.10 (d, *J* = 5.3 Hz, 8H), 1.70 – 1.49 (m, 8H).
^{13}C NMR (101 MHz, Chloroform-*d*): δ (ppm) = 138.17, 120.07, 82.78, 71.69, 28.80, 25.97, 22.24, 21.42.

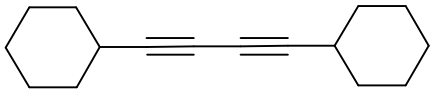

1,4-dicyclohexylbuta-1,3-diyne

^{1}H NMR (400 MHz, Chloroform-*d*) δ 2.43 (t, *J* = 8.8, 3.6 Hz, 2H), 1.82 – 1.75 (m, 4H), 1.73 – 1.66 (m, 4H), 1.52 – 1.40 (m, 6H), 1.30 (q, *J* = 6.8, 5.7 Hz, 6H).
^{13}C NMR (101 MHz, Chloroform-*d*): δ (ppm) = 82.17, 63.35, 32.53, 29.75, 26.00, 25.02.

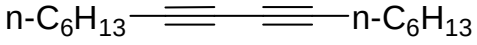

7,9-Hexadecadiyne

^{1}H NMR (400 MHz, Chloroform-d) δ 2.24 (t, J = 7.0 Hz, 4H), 1.51 (p, J = 6.9 Hz, 4H), 1.43 – 1.34 (m, 4H), 1.32 – 1.24 (m, 8H), 0.88 (t, J = 6.9 Hz, 6H).
^{13}C NMR (101 MHz, Chloroform-*d*): δ (ppm) = 65.19, 31.23, 28.46, 28.26, 22.14, 19.14, 13.95.

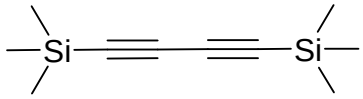

1,4-bis(trimethylsilyl)buta-1,3-diyne
^{1}H NMR (400 MHz, Chloroform-d) δ 0.07 (s, 18H).
^{13}C NMR (101 MHz, Chloroform-*d*): δ (ppm) = 70.84, -1.27.

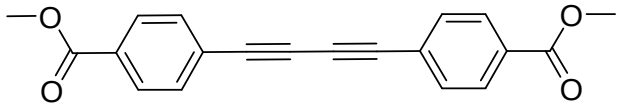

1,4-Bis(p-benzoic acid methyl ester)buta-1,3-diyne

^{1}H NMR (400 MHz, Chloroform-*d*) δ 8.02 (d, *J* = 8.5 Hz, 4H), 7.59 (d, *J* = 8.5 Hz, 4H), 3.93 (s, 6H).
^{13}C NMR (101 MHz, Chloroform-*d*): δ (ppm) = 153.15, 149.49, 139.41, 123.11, 118.88, 79.17, 29.70.

5.5.3 Oxidative cross-coupling of alkynes

We performed a conditional screening with a focus on the molar ratio of partner alkynes to get the maximum selectivity towards the asymmetric diynes. As illustrated in **table 5.6**, the catalyst was able to produce the desired asymmetrical diynes by selecting the optimized reaction condition with good to excellent selectivity. The catalyst exhibited cross-coupling between terminal alkynes of different types including aromatic and aromatic **[Entry 1, 2, 6 and 7, Table 5.6]**, aromatic and aliphatic **[Entry 3 - 5, Table 5.6]**, and aromatic and olefinic **[Entry 4, Table 5.6]**. The best selectivity to asymmetrical diyne was obtained by selecting an excess of the aliphatic alkynes over aromatic alkynes. On the other hand, selecting an equal molar amount of two aromatic alkynes produced the maximum selectivity to the asymmetric diyne.

Table 5.6 Aerobic oxidative cross coupling of terminal alkynes[a]

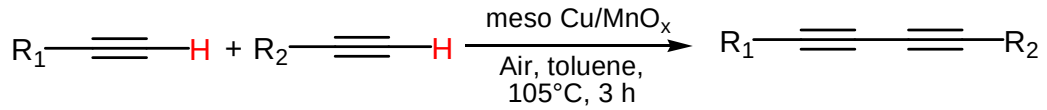

Entry	R_1	R_2	Rel. ratio	Conv[b] (%)	Coupled products selectivity[c] (%)		
					R_1-R_1	R_1-R_2	R_2-R_2
1	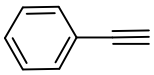	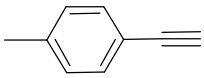	1/1	>99	17	52	23
2	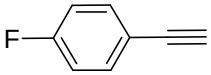	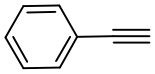	1/2	>99	38	50	12
3	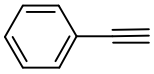	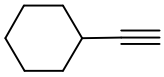	1/3	80	12	54	36
4	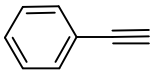	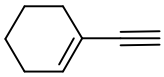	1/3	92	11	57	32
5	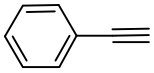	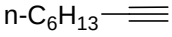	1/3	>99	20	62	18
6	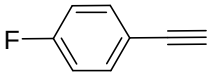	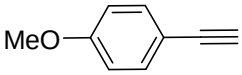	1/1	>99	20	45[d]	35
7	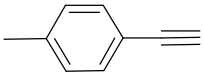	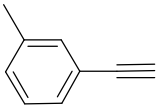	1/1	>99	20	55[e]	25

[a] Reaction conditions: alkynes total amount (0.5 mmol), meso Cu/MnO_x (6 mol% Cu with respect to total amount of alkynes), toluene (5 mL), 105°C, 3 h, air balloon. [b] Conversion was determined by GC-MS based on the concentration of limiting reagent. [c] Selectivity was calculated by GC-MS. [d] Isolated yield was 82% [e] Isolated yield was 87%.

5.5.4 Reusability and heterogeneity

Stable reusability and negligible leaching of active species are two important factors for an efficient heterogeneous catalytic system. We selected oxidative homo-coupling of phenylacetylene as the model reaction for a reusability study. After the reaction, the catalyst was retrieved by filtration and was washed with excess solvent and ethanol (>90% recovery). Prior to reuse the catalyst was reactivated at 250°C for 30 min to remove any adsorbed organic species. **Figure 5.6a** shows that the catalyst can retain activity and selectivity even after the 8th reuse. Moreover, no change in the PXRD pattern

after the 8th cycle was observed (**Figure 5.6b**), which confirms that the catalyst can retain the crystal structure even after multiple reuse cycles. To verify any possible leaching of active Cu species in the solution, the catalyst was filtered and the filtrate was analyzed by inductively coupled plasma optical emission spectrometry (ICP-OES). A trace amount of Cu (1.9 ppb) and Mn (7.0 ppb) were detected in the filtrate. All of these results signified the truly heterogeneous nature of our catalyst, which is active, stable, as well as recyclable.

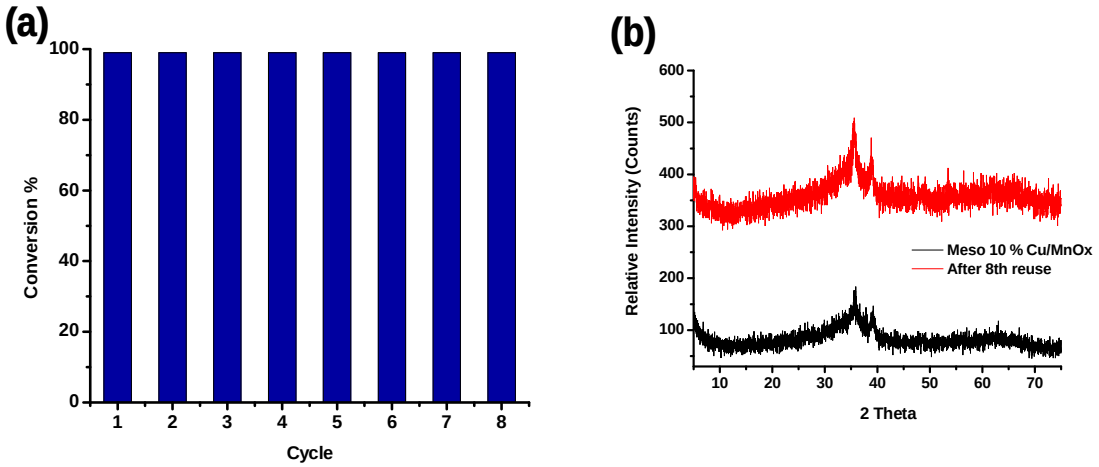

Figure 5.6 (a) The reusability experiment. Reaction Conditions: phenylacetylene (0.5 mmol), catalyst (6 mol% Cu with respect to phenylacetylene), toluene (5 mL), 105°C, 45 min, air balloon. (b) PXRD before and after 8th reuse.

5.5.5 Kinetic study

Kinetics of the reaction were then determined by conducting a time dependent study of the model reaction (oxidative coupling of phenylacetylene). Periodic sampling was undertaken at specific time intervals and conversion was determined by GC-MS. Kinetic experiments depicted a first order rate equation with respect to alkyne (**Figure 5.7**) having a rate constant of 0.093 min^{-1}. Kinetically relevant elementary steps in the reaction pathways were measured by changing the acetylenic H to D in phenylacetylene. The

obtained kinetic isotope effect (KIE) value was 0.9 (**Figure 5.8**), which signified that abstraction of the acetylenic proton of alkyne was very fast.

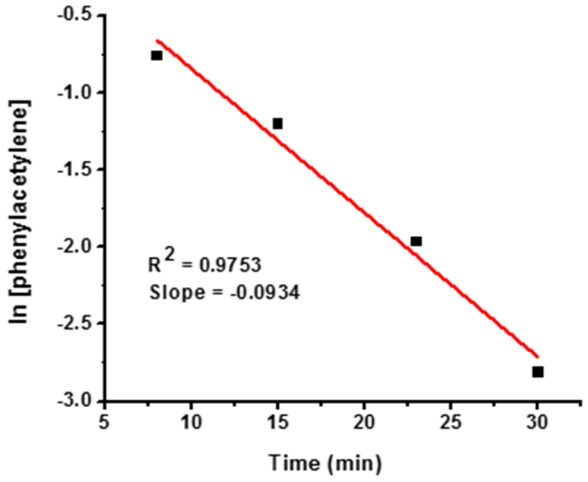

Figure 5.7 Kinetic experiment of homo-coupling of phenylacetylene by meso Cu/MnO_x. The reaction exhibited first order kinetics with respect to phenylacetylene concentration. Reaction condition: alkyne (0.5 mmol), meso Cu/MnO_x (6 mol % with respect to phenylacetylene), toluene (5 mL), 105°C, under air balloon.

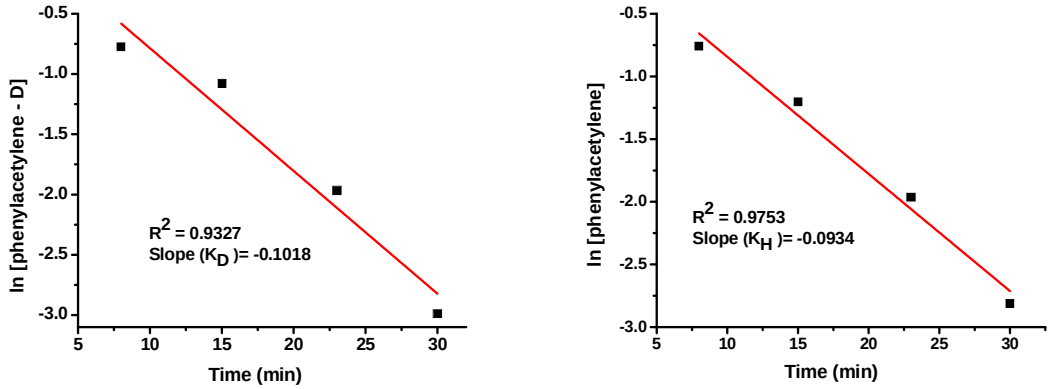

Figure 5.8 Kinetic plot of oxidation of phenylacetylene-D and phenylacetylene. The ratio of K_H/K_D = 0.9; which signified the abstraction of alkyne proton was not the rate determining step. Reaction condition: phenylacetylene (0.5 mmol), meso Cu/MnO_x (6 mol % with respect to phenylacetylene), toluene (5 mL), 105°C, air balloon.

5.5.6 Role of manganese oxide

A significant lower conversion (7% in air and 5% under nitrogen) was achieved when meso Cu/TiO_2 was selected instead of meso Cu/MnO_x (94% in air and 28% under nitrogen). We used XPS to probe the oxidation state of Cu and Mn in the unreacted catalysts and after reaction in air and nitrogen atmospheres (**Figure 5.9 and Table 5.7**). The oxidation state of Cu was estimated as 2+ in both of the untreated materials (pink and blue lines), as shown in **Figure 5.9**. The oxidation state of Cu persisted at 2+ (red and black lines) for meso Cu/MnO_x irrespective of the reaction environments (air or nitrogen). In contrast, reduction of Cu was observed (absence of satellite peaks), when the Cu/TiO_2 material was subjected to react under nitrogen (green line). These results confirmed the re-oxidation of reduced Cu species occurs in the presence of MnO_x even under nitrogen atmosphere. To further establish the re-oxidation of reduced Cu species, we tested the oxidation state of Mn in the meso Cu/MnO_x before and after reaction. As revealed from XPS, no change of oxidation state of Mn was detected when the coupling reaction was performed under air, whereas a lowering of Mn oxidation state was observed (**Table 5.7**), when the reaction was performed under nitrogen.

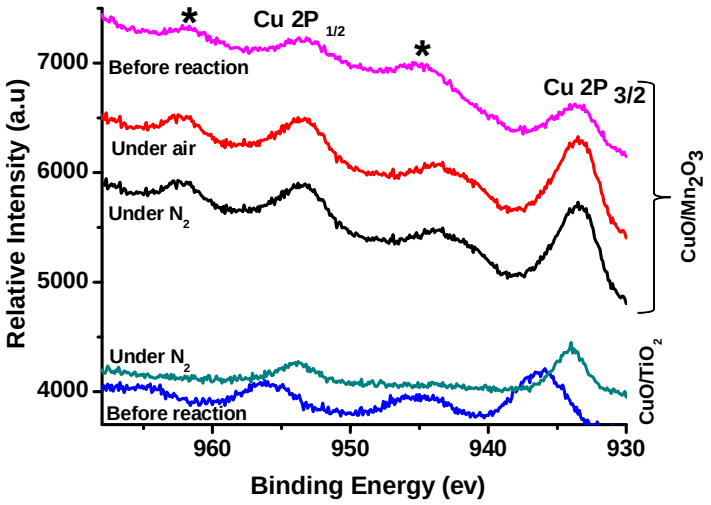

Figure 5.9 Comparison of Cu 2p XPS of meso Cu/MnO_x and meso Cu/TiO_2 after the reaction at different atmosphere (air and nitrogen).

Table 5.7 XPS data of meso Cu/MnO_x and Cu/TiO_2 before and after reaction with air and N_2

Catalyst	Mn (eV)		Cu (eV)	
	$2p_{3/2}$	$2p_{1/2}$	$2p_{3/2}$	$2p_{1/2}$
Meso Cu/MnO_x	641.5	653.2	933.3	953.3
Meso Cu/MnO_x (air)	641.6	653.6	933.5	953.0
Meso Cu/MnO_x (N_2)	641.2	653.4	933.5	953.1
Meso Cu/TiO_2	n/a	n/a	935.8	953.7
Meso Cu/TiO_2 (N_2)	n/a	n/a	933.9	956.2

n/a = not applicable.

5.5.7 Role of lattice oxygen

The homo-coupling reaction did not proceed with an internal alkyne (diphenylacetylene), suggesting that the copper species is likely binding to terminal alkyne to form the copper-acetylide species. Since in our study, no basic assistance is necessary,

the catalyst itself needs the ability to abstract the alkyne proton. As observed before, bare copper oxide was unable to produce any coupling product. We believe the labile lattice oxygen of the meso Cu/MnO_x played a role in the abstraction of acetylic proton. We therefore conducted the homo-coupling of phenylacetylene by meso Cu/MnO_x heated at different calcination temperature (250°C, 350°C, 450°C and 550°C), since calcination has a remarkable effect in crystallinity of UCT material. An increment of catalytic performance was observed with the heat treatment from 250°C to 450°C, whereas, the activity again decreased at 550°C (**Figure 5.10**). Temperature programmed desorption (TPD) experiments were performed in order to determine the nature of oxygen species of the material. As revealed from the **figure 5.11**, the material calcined at 250°C to 450°C showed a desorption peak around 500°C which can be ascribed as desorption of lattice oxygen. Therefore, the role of labile lattice oxygen of copper manganese oxide is probably the abstraction of alkyne hydrogen to from the alkynyl species.

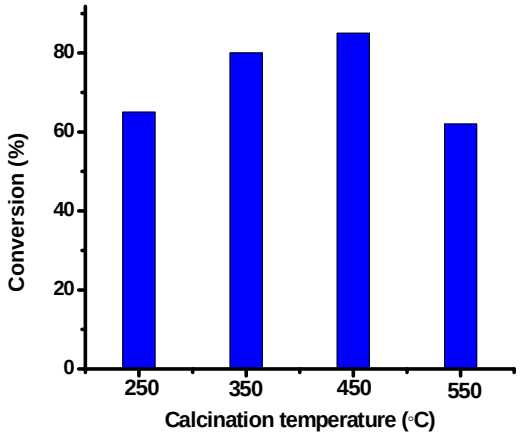

Figure 5.10 Effect of calcination temperature on catalytic activity. Reaction Conditions: Phenylacetylene (0.5 mmol), meso Cu/MnO_x (6 mol%), toluene (5 mL), 105°C, 30 min, air balloon.

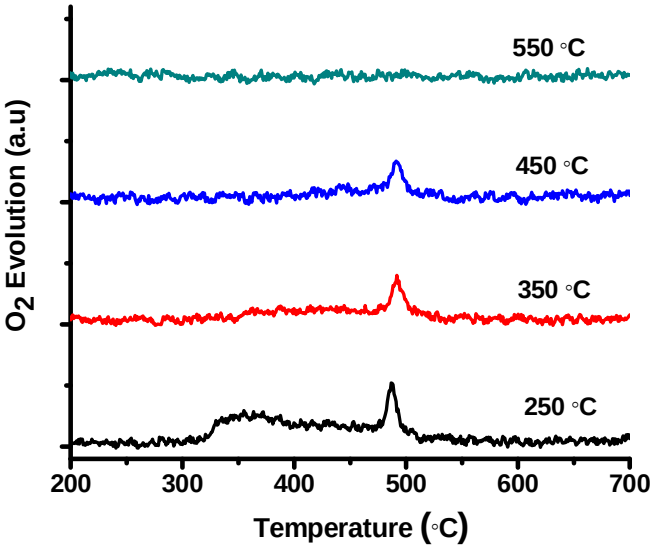

Figure 5.11 O_2-TPD of meso Cu/MnO_x at different calcination temperatures.

5.6 Theoritical results

5.6.1 Geometries and transition metal coordination

The H_2O molecule is favored as an inert framework ligand, because charge effects associated with ligands, such as OH^- or O^{2-}, can be avoided. The geometries of the H_2O donor ligands (O−H = 0.96Å, ∠H−O−H = 104°) are fixed and planar relative to the metal atoms. The hydrogen atoms of the H_2O molecule are maintained co-planar with the principal axis of the coordination complex. The distances for ligands acting as lattice sites bonded to a metal are always kept fixed: Cu−O, Mn−O = 2.00Å. The simplest reactive alkyne, acetylene (H−C≡C−H), is used in all calculations and discussions. Other reactive ligands, $H-C\equiv C:^-$, O_2, HO_2^-, and N_2 complete the coordination sphere, and form short-lived species. The Cu atoms are configured in a five-coordinate environment while the Mn atoms are bonded to six ligands yielding six-fold coordination. A suitable overall charge

on the complex is assigned, so that the formal oxidation states of the metal atoms approximately correspond to the experimental values. During the catalytic reaction, the spin states of the Mn and Cu change, and it becomes important to track the spin of the model complexes in order to obtain suitable estimates of the energies and geometries along the pathway.

5.6.2 Basis sets and density functional

Calculations were performed by utilizing the Gaussian[37], GAMESS[38], and NWChem[39] programs employing mostly the Def2TZVP basis[40] for the Mn and Cu atoms, and the 6-31G(d) basis[41] for all ligand atoms (H, C, N, O). The LANL2DZ basis[42] was also used for the metal atoms to initially perform tests on different complexes. Both wave function and density functional theories were utilized in the description of the model systems. For calculations utilizing density functional theory, the M06-L functional, known to provide good results for inorganic, transition metal, and organometallic complexes[43] was employed throughout. A dispersion correction[44] was attempted to improve the stability of an initial transient, which then dissociates along a reaction pathway, but this proved difficult because the separated species involved a charged transition metal complex lacking surface delocalization of charge.

5.6.3 Optimized geometries of transient intermediates

For all the calculations presented here, only a partial optimization of the proposed model transition complexes is performed, although this approach is fraught with uncertainty. However, because the active catalytic sites containing Mn and Cu atoms, together with their ligands, are constrained by bonds within the crystal lattice, this approach

seems reasonable. With this in mind, vibrational analysis of these complexes was carried out with a view of determining stationary points which are either minima or transition states. Since partial optimization is employed, the results from frequency calculations are ambiguous and cannot provide with certainty that a minimum or intermediate structure was reached. The negative frequencies obtained from a vibrational analysis usually pointed to vibrational motions of the ligands which always remain fixed for the ligands which are not optimized.

5.6.4 Cu sites on the meso Cu/MnO_x surface

Because acetylenes have two π orbitals, π−[L_4Cu(II)(H−C≡C−H)]$^{2+}$ complexes are capable of exhibiting enhanced stability. Tatsumi et al.[45] showed that the Dewar-Chatt-Duncanson model[46] can be applied to both double bonds, $\pi_\perp$,$\pi^*_\perp$ and $\pi_{||}$,$\pi^*_{||}$, which play an important role in bonding to mononuclear transition metal complexes. The π−[L_4Cu(II)(H−C≡C−H)]$^{2+}$ complex, as shown in **Figure 5.12a**, appears to be more stable than the corresponding Cu(I) complex, which is quite reasonable because the d_z^2 orbital is now only partially filled and can interact with the first π system, i.e. $\pi_{||}$,$\pi^*_{||}$. The $\pi_{||} - d_z^2$ is a three-electron stabilizing interaction, together with further stabilization from a favorable interaction with $\pi^*_{||}$. The $\pi^*_\perp$ orbital from the second π system stabilizes a matched filled Cu d_π orbital. This corresponds to the transformation of π−[L_4Cu(II)(H−C≡C−H)] when H^+ is abstracted to an π−[L_4Cu(II)($^-$C≡C−H)] complex, shown in **Figure 5.12b** which can then couple with a neighboring acetylide anion (H−C≡C:$^-$).

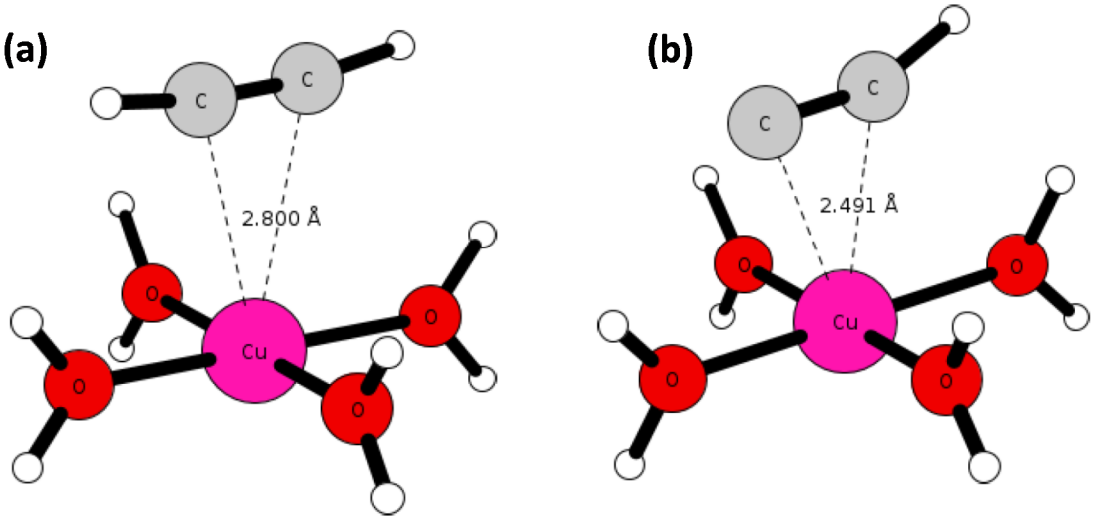

Figure 5.12 (a) $\pi-[L_4Cu(II)(H\text{-}C \equiv C\text{-}H)]^{2+}$, and (b) $\pi-[L_4Cu(II)(C \equiv C\text{-}H)]^{+}$complexes. The stability of the complex (a) relative to the separate components is 6.2 kcal mol^{-1}. The acetylide anion ($-C \equiv C\text{-}H$) in (b) was unstable with respect to a DFT calculation using a 6-31g* basis set, and prevented the determination of relative stability, but its value is larger than (3a). L stands for H_2O.

5.6.5 Mn sites on the meso Cu/MnO_x surface

Vacant Mn sites on the Cu/MnO_x surface play a complementary role with respect to the Cu sites, especially when they are adjacent to one another. The Mn sites absorb O_2, form stable L_nMnO_2 intermediates, and are capable of abstracting H^+ from neighboring Cu sites bonded to $H-C\equiv C-H$ molecules. In the case of Mn surface sites with L_nMnO_2 intermediate, it is important to keep track of the spin on the Mn atom. The $[L_nMn(II)(O_2)]$ (d^5 : S = 6) complex is not stable, whereas $[L_nMn(III)(O_2)]^+$ (d^4 : S = 5) forms a stable complex as shown in **Figure 5.13a.** The O_2 abstraction of H^+ by $[L_nMn(III)(O_2)]^+$, does not alter the electronic configuration of the Mn(III) in the complex. The complex $[L_nMn(III)(O_2H)]^{2+}$ (d^4: S = 5) remains stable as shown in **Figure 5.13b** below, eventually

releasing the OOH^- ion. The remaining $[L_nMn(III)]^{3+}$ site is eventually reduced to $[L_nMn(II)]^{2+}$.

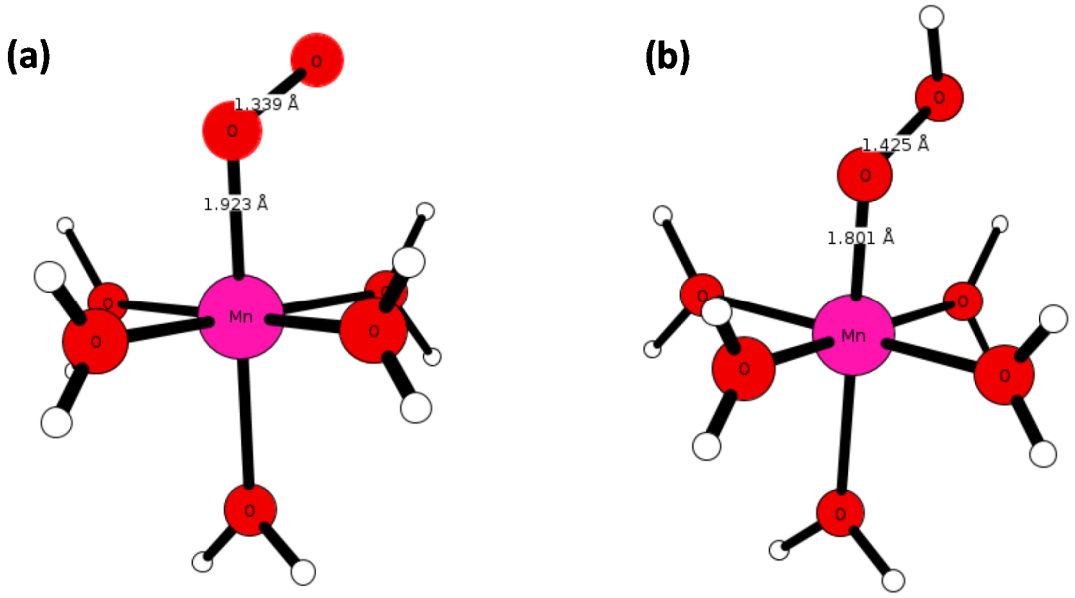

Figure 5.13 (a) $[L_nMn(III)(O_2)]^+$, and (b) $[L_nMn(III)(O_2H)]^{2+}$, complexes. The stability of the complex (a) relative to the separate components is 59.4 kcal mol^{-1}. The hydroperoxyl anion (O_2H^-) was unstable with respect to a DFT calculation using a 6-31g* basis set, and prevented the determination of relative stability, but its value is larger than (4a). L stands for H_2O.

5.6.6 Molecular analogues of reactive surface species

Several model systems can be used to illustrate the oxidative coupling of alkynes on the Cu/MnO_x surface, and three are shown in **Figure 5.14** For the models, it is assumed that nearby Mn sites are capable of interacting with catalytically active Cu sites, and have the capability of producing a coupled alkyne product. The model in **Figure 5.14a** is considered favorable because the Mn atom, squeezed between two active Cu atoms, and bonded to two acetylide anions, is capable of interacting with the approaching anionic fragments ($H{-}C{\equiv}C{:}^- \leftrightarrow {}^-{:}C{\equiv}C{-}H$), stabilizing the incipient repulsive interaction, and

subsequently absorbing the two discarded electrons, resulting from the oxidation of the acetylide anions, into an available Mn(d) orbital. An advantage of considering the model in **Figure 5.14b** is that the Cu sites are adjacent to each other (Mn sites are also presumed to be adjacent to each Cu site), allowing direct coupling of the acetylide anions and electron exchange with Mn atoms. Model **Figure 5.14b** is also analogous to an intermediate in the solution-phase Glaser-Hay reaction. Finally, the model in **Figure 5.14c** is similar to that in **Figure 5.14b**, but now includes O_2 as the bridging ligand between Cu atoms. O_2 is plentiful under the experimental conditions, when air and O_2 are available above the Cu/MnO_x surface. A dominant structure, supported by Cu atoms, may include the side-on μ-η^2:η^2-peroxo motif[47-49] shown in **Figure 5.14c** which provides some degree of confidence that this is a reasonably valid model.

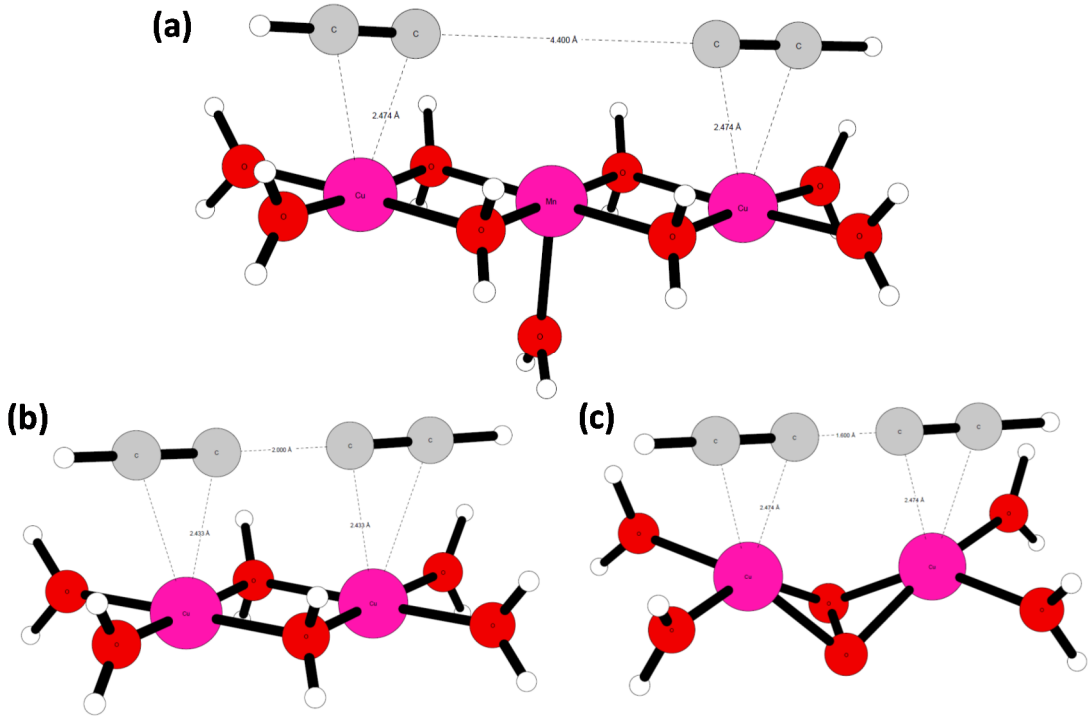

Figure 5.14 Model systems [(a) Mn atom, squeezed between two active Cu atoms, (b) Cu sites are adjacent to each other and (c) O_2 as the bridging ligand between Cu atoms] on the Cu/MnO_x surface capable of oxidative coupling of alkynes.

5.7 Discussion

This study features the design of mesoporous copper incorporated manganese oxide material as an efficient heterogeneous catalyst for aerobic oxidative coupling of alkynes to 1,3-diynes. The material was synthesized by an inverse micelle templated sol-gel synthesis procedure using copper nitrate as the copper source. In this process, a pluoronic surfactant (P123) along with the metal source (Mn and Cu) randomly packed in an acidic alcoholic solution (HNO_3 + butanol) to build the mesostructure. The nitrate ions pulled the positively charged manganese and copper oxo-clusters into the core of the inverse micelles. The formation of NO_x (by thermal decomposition of nitrates) controls the whole sol-gel process. Control of the dopant amount is crucial, since high amounts of dopants can destabilize the reaction gel and cause the surfactant to precipitate. We have successfully employed 1 -10 mol % incorporation of copper without disturbing the solution gel. The reaction system was then treated at 120°C for 3 h, followed by extracting the surfactant with ethanol to get the mesoporous material (meso Cu/MnO_x). Chemisorbed species (nitrates and carboxylates) were removed from the material by a heat treatment at 150°C for 12 h and 250°C for 3 h consecutively.

As illustrated in Table 3, our system indicates excellent substrate scope and functional group tolerability, giving the desired homo-coupling product in excellent yields. For aromatic alkynes, excellent activity was observed for both electron donation and electron withdrawing groups. Halogen substituted aromatic alkynes gave the desired product with excellent selectivity (>99%) without any dehalogenation, though dehalogenation and oxidative addition of halogen substituted aromatic compounds has been shown to occur in copper mediated systems[50]. The longer reaction time (15 h) to

achieve efficiency for a heteroatom containing substrate can be attributed to the poisoning of the active copper sites of the catalyst by coordination with N-heteroatoms[51]. Homo-coupling reactions with long chain aliphatic alkynes are known to be relatively difficult and higher copper loading or longer reaction times are essential, as mentioned in previous studies[15,20,52]. However, meso Cu/MnO_x exhibited excellent performance in the reaction with the long chain, inactive 1-octyne with no drop in turnover number versus aromatic alkynes. The easy diffusion and transportation of 1-octyne in the mesoporous network may be the reason behind the high activity. Excellent selectivity was also observed with a reaction of an enyne, though manganese oxides are known to oxidize the double bond in catalytic conditions[53]. The excellent selectivity was also demonstrated by the homo-coupling reaction of a silylated derivative without oxidation of the Si-H bond[54].

In cross-coupling of alkynes, discrimination of partner alkynes to metal acetylide formation has been considered the most important feature[28]. We hypothesized that proper choice of relative alkyne amounts might provide the discrimination effect toward different alkynes. There were no significant differences in the rate of the homo-coupling of aromatic alkynes. Therefore, by selecting an equal amount of aromatic alkynes, we observed the maximum selectivity towards the asymmetric diynes. As observed in previous studies, aliphatic alkynes reacted faster to form the metal acetylide species to provide the discrimination effect[36]. Similarly in our study, asymmetric diynes were synthesized with good to excellent selectivity when aliphatic alkynes were used in excess over aromatic alkynes.

In general, copper undergoes a one electron reduction and forms a Cu-acetylide species, which dimerizes to give the corresponding diyne [55]. As elucidated from DFT

calculations, a schematic diagram, showing how the energy decreases as the two separated acetylide anions for model **Figure 5.14b** readily couple to form a coupled acetylene product is given in **Figure 5.15**. The relative energy (-84.6 kcal mol^{-1}) of the final optimized coupled product is reasonable for the formation of the C-C bond in H−C≡C-C≡C−H, which is the bond joining the two acetylide fragments. However, no change in copper oxidation state of meso Cu/MnO_x was observed after the reaction by XPS. Therefore, re-oxidation of reduced copper species has been included in the present oxidative coupling. The re-oxidation is well supported by disappearance of the satellite peaks of Cu 2p in meso Cu/TiO_2, confirmed the reduction of Cu(II) to Cu(I) in the present homo-coupling reaction under nitrogen atmosphere. In contrast, the re-oxidation was efficiently promoted by MnO_x even under nitrogen atmosphere. A reduction of Mn oxidation state was also observed by XPS which complemented the re-oxidation of reduced Cu(I) species by Mn(III) species. On the other hand, under an aerobic atmosphere, the reduced Mn species can effectively reoxidize[56].

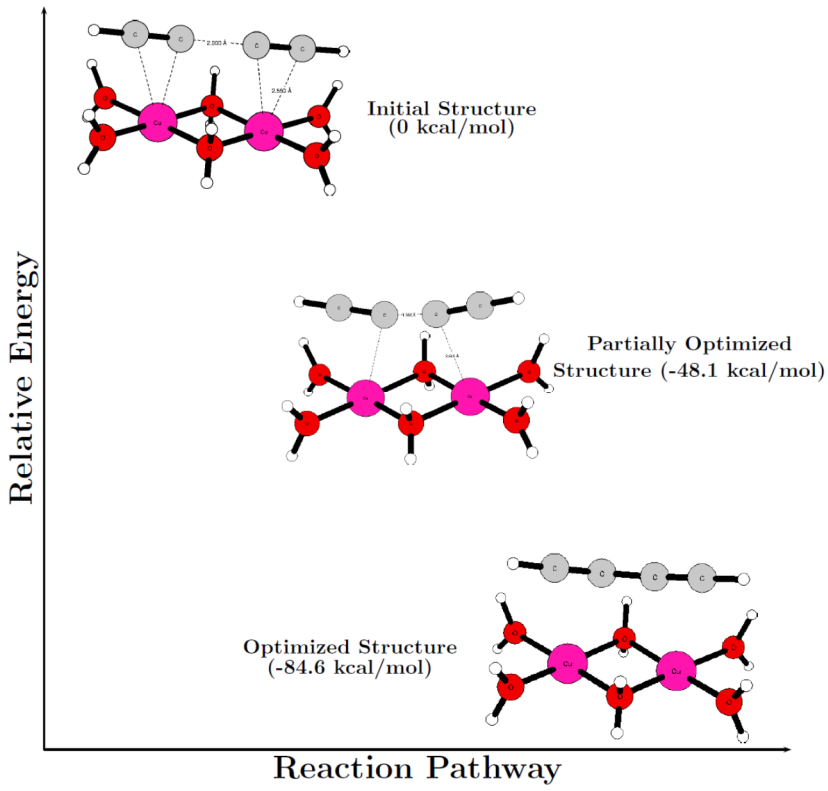

Figure 5.15 Relative energies for the coupling of two acetylide moieties along the optimization pathway for structure **Figure 5.14b**. Only the acetylide fragments are optimized, with H_2O ligands and metal atoms remaining fixed to simulate the infrastructure of a Cu/MnO_x surface.

Based on experimental findings, we propose a mechanism for oxidative coupling of alkynes by meso Cu/MnO_x (**Scheme 5.1**). First, the lattice oxygens of meso Cu/MnO_x abstract an alkyne proton to form the Cu(II) acetylide species (formed by weak π coordination between alkyne triple bond and copper center) , which dimerizes to give the corresponding diyne and generates Cu(I) species. The surface active Mn centers simultaneously involve a one electron reduction and re-oxidizes the Cu(I) species to Cu(II). Under catalytic turnover conditions, the reduction of active Mn species can lead to facile release of lattice oxygen[57]. The labile lattice oxygen re-oxidizes the Mn center back with production of H_2O_2, which could easily be decomposed over manganese oxide and form

water[57-59]. The supply of oxygen is crucial for the catalytic activity, as loss of lattice oxygen should be replenished by oxygen from the air. This also was supported by the observation that using a dinitrogen atmosphere instead of air diminished the reaction rate. A kinetic isotope effect was hardly observed in the homo-coupling of phenylacetylene (k_H/k_D = 0.9) indicating that the abstraction of the alkyne proton is not the rate determining step. Therefore, the re-oxidation of reduced copper species is probably the rate determining step in the present coupling reaction.

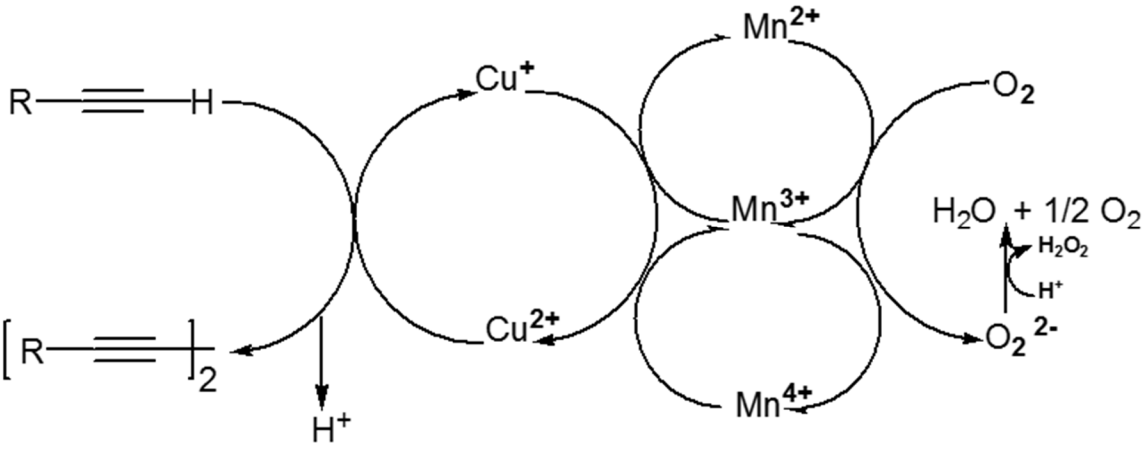

Scheme 5.1 Proposed mechanism of aerobic oxidative coupling of alkynes by meso Cu/MnO_x.

The coupling reaction mechanism was further elucidated with DFT calculations. The experimental results appear to involve at least two mechanisms for alkyne coupling, depending on the reaction conditions involving either aerobic and nitrogen rich environment. When either oxygen or air are used, more than one mechanism is probably operative for alkyne coupling. In the following, a reasonable mechanism for oxidative coupling of terminal alkynes on meso Cu/MnO_x will be explored. A basic assumption for

any credible mechanism presumes that Cu atoms are randomly distributed on the Cu/MnO_x surface and are intertwined with neighboring Mn atoms, forming bonds with O atoms.

Air environment

1. Initially, the neutral H−C≡C−H molecule forms a weakly bound π − $[L_4Cu(II)(C_2H_2)]^{2+}$ complex (L = H_2O).

2. Concomitantly, an adjacent $L_nMn(III)^{3+}$ species reacts with O_2 to form $[L_nMn(III)(O_2)]^+$. The $[L_nMn(III)(O_2)]^+$ intermediate is able to directly abstract an H^+ and yield a $[\pi{-}L_4Cu(II)(C{\equiv}CH)]^+$ and a $[L_nMn(III)(O_2H)]^{2+}$ complex. L_nMn sites exhibit a twofold role in enhancing catalysis, by both changing its oxidation state and by yielding an acetylide anion.

3. $[L_nMn(III)(O_2H)]^{2+}$ loses O_2H^- to form an $[L_nMn(III)]^{3+}$ complex.

4. In the final step, two acetylide anions from $[\pi{-}L_4Cu(II)(C{\equiv}CH)]^+$ species react to form a diyne molecule (e.g., H −C≡C−C≡C−H) and residual $L_4Cu(II)$ surface species.

The overall equations for the postulated mechanism are given below:

$$2\ [\pi{-}L_nCu(II)C_2H_2]^{2+} + 2\ [L_nMn(III)(O_2)]^+ \rightarrow 2\ [\pi{-}L_nCu(II)(C{\equiv}CH)]^+ + 2[L_nMn(III)(O_2H)]^{2+}$$

$$2\ [L_nMn(III)(O_2H)]^{2+} \rightarrow 2\ [L_nMn(III)]^{3+} + 2\ OOH^-$$

$$2\ OOH^- \rightarrow H_2O + 1/2O_2 + 2e^-$$

$$2\ [\pi{-}L_nCu(II)(C{\equiv}CH)]^+ \rightarrow 2\ [L_nCu(I)]^+ + H{-}C{\equiv}C{-}C{\equiv}C{-}H$$

Nitrogen environment

Surface sites containing reactive species such as $[L_nMn(III){=}O]+$, are assumed to always be available on the Cu/MnO_x surface under nitrogen environments.

1. $[L_nMn(III)=O]^+$ reactive species abstracts an H^+ from $[\pi-L_nCu(II)(C_2H_2)]^{2+}$ to form $[\pi-L_nCu(II)(C\equiv CH)]^+$ and $[L_nMn(III)(OH)]^{2+}$.

2. $[L_nMn(III)(OH)]^{2+}$ decomposes to $[L_nMn(III)]^{3+} + OH^-$.

3. Two acetylide anions from $[\pi-L_4Cu(II)(C\equiv CH)]^+$ species react to form the coupled product ($H-C\equiv C-C\equiv C-H$).

The yield of coupled alkyne product is reduced, when the Cu/MnO_x surface is exposed to nitrogen environments, and may be related to the formation of a weak $[L_nCu(II)(N_2)]^{2+}$ complex which inhibits the formation of the neutral $[\pi-L_nCu(II)(C_2H_2)]^{2+}$ complex. Complex formation with nitrogen competes with $H-C\equiv C-H$ for Cu(II) sites and decreases catalytic activity. Similar to the $L_nCu(II)$ sites, the $L_nMn(III)$ sites can also form weakly bound complexes with N_2 which may hinder catalytic reaction of alkynes under nitrogen atmosphere.

5.7 Conclusion

In summary, we report the fabrication of thermally stable and reusable mesoporous copper supported manganese oxide materials (meso Cu/MnO_x) for aerobic oxidative coupling of alkynes. The material was composed by aggregation of rounded nanoparticles with high surface area (as high as 270 m^2g^{-1}) and uniform mesoporous size (3.0 – 3.4 nm) distribution. Physicochemical properties (surface area, pore size, crystallinity) of the material can be easily tuned by simple heat treatment. The alignment of copper over the manganese oxide was proven by XRD refinement showing a copper (II) oxide (CuO) phase at higher copper doping. Elemental mapping analysis by TEM-EDX confirmed a uniform distribution of copper oxide over the manganese oxide. Broad substrate scope and excellent functional group tolerability were demonstrated for the oxidative homo and cross-coupling

of terminal alkynes. While unravelling the mechanistic details, a synergistic effect between copper and manganese has been established along with the contribution of labile lattice oxygen. The high catalytic activity can be attributed to an electron transfer pathway between dioxygen and alkyne through manganese and copper oxide. In addition, we performed DFT calculations to provide a reasonably qualitative description of the catalytic pathway by building model compounds in four/five or six - fold coordination to manganese and copper atoms, together with their ligands and constrained by bonds in the lattice. In the case of copper active sites, a π coordination between alkyne triple bond and copper enhancing the acidity of alkyne proton has been shown, resembling the classical Bohlmann mechanism. The proton was abstracted by the complex formed between manganese active sites and dioxygen, which can be correlated with the experiments, where an exchange mechanism between labile lattice oxygen and aerial oxygen was proved to be the factor behind the deprotonation. After deprotonation, the copper (I) acetylide species was dimerized to produce the diyne products as observed by the relative energies of the coupling of two acetylide moieties. Therefore, the designing of copper and manganese active sites along with the validity of the coupling reaction mechanism was strengthened from both experimental and theoretical perspectives. Finally, using air as the terminal oxidant, avoidance of additives, no pretreatment of catalysts, high turnover numbers along with superior reusability (no performance loss up to eight cycles) and excellent selectivity to both homo and cross-coupling of alkynes, make our catalytic protocol competitive to the existing heterogeneous copper based catalytic systems. The combined experimental and theoretical study can serve as a benchmark for the oxidative coupling reactions and opens

up a new avenue to design and identify supported copper based heterogeneous catalysts for potential applications in other complex oxidative coupling reactions.

5.8 References

(1) Shi Shun, A. L.; Tykwinski, R. R. *Angew. Chem., Int. Ed.* **2006**, *45*, 1034-1057.

(2) Liu, J.; Lam, J. W.; Tang, B. Z. *Chem. Rev.* **2009**, *109*, 5799-5867.

(3) Hirsch, A.; Wiley Online Library: 2005.

(4) Glaser, C. *Ber. Dtsch. Chem. Ges.* **1869**, *2*, 422-424.

(5) Siemsen, P.; Livingston, R. C.; Diederich, F. *Angew. Chem., Int. Ed.* **2000**, *39*, 2632-2657.

(6) Tasker, S. Z.; Standley, E. A.; Jamison, T. F. *Nature* **2014**, *509*, 299-309.

(7) Zhu, Y.; Shi, Y. *Org. Biomol. Chem.* **2013**, *11*, 7451-7454.

(8) Li, J.-H.; Liang, Y.; Zhang, X.-D. *Tetrahedron* **2005**, *61*, 1903-1907.

(9) Sheldon, R.; Downing, R. *Appl. Catal., A: Gen.* **1999**, *189*, 163-183.

(10) Sheldon, R. A.; Van Bekkum, H. *Fine chemicals through heterogeneous catalysis*; John Wiley & Sons, 2008.

(11) Alonso, F.; Yus, M. *ACS Catal.* **2012**, *2*, 1441-1451.

(12) Chinchilla, R.; Najera, C. *Chem. Rev.* **2013**, *114*, 1783-1826.

(13) Li, H.; Yang, M.; Pu, Q. *Microporous Mesoporous Mater.* **2012**, *148*, 166-173.

(14) Bandini, M.; Luque, R.; Budarin, V.; Macquarrie, D. J. *Tetrahedron* **2005**, *61*, 9860-9868.

(15) Oishi, T.; Yamaguchi, K.; Mizuno, N. *ACS Catal.* **2011**, *1*, 1351-1354.

(16) Kamata, K.; Yamaguchi, S.; Kotani, M.; Yamaguchi, K.; Mizuno, N. *Angew. Chem.* **2008**, *120*, 2441-2444.

(17) van Gelderen, L.; Rothenberg, G.; Calderone, V. R.; Wilson, K.; Shiju, N. R. *Appl. Organomet. Chem.* **2013**, *27*, 23-27.

(18) He, Y.; Cai, C. *Catal. Sci. Technol.* **2012**, *2*, 1126-1129.

(19) Oishi, T.; Katayama, T.; Yamaguchi, K.; Mizuno, N. *Chem.- Eur. J.* **2009**, *15*, 7539-7542.

(20) Nador, F.; Volpe, M. A.; Alonso, F.; Feldhoff, A.; Kirschning, A.; Radivoy, G. *Appl. Catal., A: Gen.* **2013**, *455*, 39-45.

(21) Jia, X.; Yin, K.; Li, C.; Li, J.; Bian, H. *Green Chem.* **2011**, *13*, 2175-2178.

(22) Dar, B. A.; Vyas, D.; Shrivastava, V.; Farooq, S.; Sharma, A.; Sharma, S.; Sharma, P. R.; Sharma, M.; Singh, B. *C. R. Chim.* **2014**, *17*, 316-323.

(23) Kuhn, P.; Alix, A.; Kumarraja, M.; Louis, B.; Pale, P.; Sommer, J. *Eur. J. Org. Chem.* **2009**, *2009*, 423-429.

(24) Wang, D.; Li, J.; Li, N.; Gao, T.; Hou, S.; Chen, B. *Green Chem.* **2010**, *12*, 45-48.

(25) Zhu, B. C.; Jiang, X. Z. *Appl. Organomet. Chem.* **2007**, *21*, 345-349.

(26) Alonso, F.; Melkonian, T.; Moglie, Y.; Yus, M. *Eur. J. Org. Chem.* **2011**, *2011*, 2524-2530.

(27) Shao, Z.; Peng, F. *Angew. Chem., Int. Ed.* **2010**, *49*, 9566-9568.

(28) Peng, H.; Xi, Y.; Ronaghi, N.; Dong, B.; Akhmedov, N. G.; Shi, X. *J. Am. Chem. Soc.* **2014**, *136*, 13174-13177.

(29) Bohlmann, F.; Schönowsky, H.; Inhoffen, E.; Grau, G. *Chem. Ber.* **1964**, *97*, 794-800.

(30) Jover, J.; Spuhler, P.; Zhao, L.; McArdle, C.; Maseras, F. *Catal. Sci. Technol* **2014**, *4*, 4200-4209.

(31) Jover, J. *J. Chem.* **2015**, *2015*.

(32) Fomina, L.; Vazquez, B.; Tkatchouk, E.; Fomine, S. *Tetrahedron* **2002**, *58*, 6741-6747.

(33) Park, J.; Hong, S. *Chem. Soc. Rev.* **2012**, *41*, 6931-6943.

(34) Lee, J. M.; Na, Y.; Han, H.; Chang, S. *Chem. Soc. Rev.* **2004**, *33*, 302-312.

(35) Poyraz, A. S.; Kuo, C.-H.; Biswas, S.; King'ondu, C. K.; Suib, S. L. *Nat. Commun.* **2013**, *4*, 2952.

(36) Biswas, S.; Dutta, B.; Mullick, K.; Kuo, C.-H.; Poyraz, A. S.; Suib, S. L. *ACS Catal.* **2015**, *5*, 4394-4403.

(37) Gaussian, F. *Wallingford, CT* **2009**.

(38) Schmidt, M. W.; Baldridge, K. K.; Boatz, J. A.; Elbert, S. T.; Gordon, M. S.; Jensen, J. H.; Koseki, S.; Matsunaga, N.; Nguyen, K. A.; Su, S. *J. Comput. Chem* **1993**, *14*, 1347-1363.

(39) Valiev, M.; Bylaska, E. J.; Govind, N.; Kowalski, K.; Straatsma, T. P.; Van Dam, H. J.; Wang, D.; Nieplocha, J.; Apra, E.; Windus, T. L. *Comput. Phys. Commun.* **2010**, *181*, 1477-1489.

(40) Weigend, F.; Ahlrichs, R. *Phys. Chem. Chem. Phys.* **2005**, *7*, 3297-3305.

(41) Ditchfield, R.; Hehre, W. J.; Pople, J. A. *J. Chem. Phys.* **1971**, *54*, 724-728.

(42) Hay, P. J.; Wadt, W. R. *J. Chem. Phys.* **1985**, *82*, 270-283.

(43) Zhao, Y.; Truhlar, D. G. *J. Chem. Phys.* **2006**, *125*, 194101.

(44) Grimme, S.; Antony, J.; Ehrlich, S.; Krieg, H. *J. Chem. Phys.* **2010**, *132*, 154104.

(45) Tatsumi, K.; Hoffmann, R.; Templeton, J. L. *Inorg. Chem.* **1982**, *21*, 466-468.

(46) Chatt, J.; Duncanson, L. *J. Chem. Soc. (Resumed)* **1953**, 2939-2947.

(47) Cramer, C. J.; Tolman, W. B. *Acc. Chem. Res.* **2007**, *40*, 601-608.

(48) Gherman, B. F.; Cramer, C. J. *Coord. Chem. Rev.* **2009**, *253*, 723-753.

(49) Woertink, J. S.; Smeets, P. J.; Groothaert, M. H.; Vance, M. A.; Sels, B. F.; Schoonheydt, R. A.; Solomon, E. I. *Proc. Natl. Acad. Sci. U.S.A.* **2009**, *106*, 18908-18913.

(50) Magné, V.; Garnier, T.; Danel, M.; Pale, P.; Chassaing, S. *Org. Lett.* **2015**, *17*, 4494-4497.

(51) Karimi, B.; Biglari, A.; Clark, J. H.; Budarin, V. *Angew. Chem., Int. Ed.* **2007**, *46*, 7210-7213.

(52) Li, H.; Yang, M.; Zhang, X.; Yan, L.; Li, J.; Qi, Y. *New J. Chem.* **2013**, *37*, 1343-1349.

(53) Saisaha, P.; de Boer, J. W.; Browne, W. R. *Chem. Soc. Rev.* **2013**, *42*, 2059-2074.

(54) Yamaguchi, K.; Wang, Y.; Oishi, T.; Kuroda, Y.; Mizuno, N. *Angew. Chem., Int. Ed.* **2013**, *52*, 5627-5630.

(55) Maaten, B.; Moussa, J.; Desmarets, C.; Gredin, P.; Beaunier, P.; Kanger, T.; Tõnsuaadu, K.; Villemin, D.; Gruselle, M. . *Mol. Catal. A: Chem.* **2014**, *393*, 112-116.

(56) Suib, S. L. *Acc. Chem. Res.* **2008**, *41*, 479-487.

(57) Makwana, V. D.; Son, Y.-C.; Howell, A. R.; Suib, S. L. *J. Catal.* **2002**, *210*, 46-52.

(58) Sithambaram, S.; Kumar, R.; Son, Y.-C.; Suib, S. L. *J. Catal.* **2008**, *253*, 269-277.

(59) Zhou, H.; Shen, Y.; Wang, J.; Chen, X.; O'Young, C.-L.; Suib, S. L. *J. Catal.* **1998**, *176*, 321-328.

CHAPTER 6. Future Perspective

The catalytic oxidation methodologies described here maintain ‘source reduction’, the fundamental goal of ‘green chemistry’. The invented mesoporous manganese oxide materials were are able to produce fine chemicals from raw materials using heterogeneous catalytic pathways. Proper reusability, less waste generation (mostly water), air as oxidant and atmospheric conditions are the key parameters of the research protocol. As a future perspective, the developed materials can be (1) further tuned and optimized to improve the physicochemical properties (surface area, crystallinity, pore size) responsible for catalytic activity, (2) made more generic (design more active metal supported mesoporous catalysts) and (3) utilized for complex catalytic oxidation and other heterogeneous reactions.

Although a green oxidant, air, is very inert towards strong C-H bond activation due to the typical ground state of oxygen. Another obstacle associated with the inertness of C-H bond is failure of scale up procedures. Catalytic oxidation of inactive C-H bond by ambient air as the ultimate oxidant represents one of the demanding challenges in chemical industry. Most of the efficient heterogeneous systems for catalytic oxidation of C-H bonds involve use of precious metals (Au, Pd), additives and high pressure. Our cesium promoted mesoporous manganese oxide displayed superior activity in diverse catalytic oxidation reactions. Therefore, this material might be a good candidate as a potential catalyst for C-H activation. Reaction parameters can be tuned to increase surface area as well as incorporated cesium amount can also be increased. Also, the oxidation activity of the catalyst in gas phase can be determined, since manganese oxide showed much promise in gas phase oxidation reactions. For long term perspective, developing catalytic

methodologies for solar fuel production is highly desirable to meet the exponentially rising rate of energy storage and consumption. Therefore, these manganese oxide materials can be utilized in water oxidation reaction, considered as the bottleneck in artificial photosynthesis aiming to produce hydrogen and oxygen.

In summary, this work highlights material aspects of catalysis research by introducing structure-activity relationship of robust, inexpensive, thermally stable, and reusable materials in oxidation reactions. Furthermore, versatile nature of these materials open up a new avenue in search for accessible environmentally benign catalysts for alternative energy utilization.

APPENDIX

List of publications, book chapters and presentations

1. Journal Articles

- **Biswas, S.**; Mullick, K.; Chen, S.-Y.; Kriz, D. A.; Shakil, M. D; Angeles-Boza, A. M.; Rossi, A. R; Suib, S. L. 'Mesoporous Copper/Manganese Oxide Catalyzed Coupling of Alkynes: Evidence for Synergistic Cooperative Catalysis' *ACS Catal.* **2016**, *6*, 5069.

- **Biswas, S**.*; Dutta, B.*; Sharma, V.; Savage, N. O.; Pamir Alpay, S.; Suib, S. L. 'Mesoporous Manganese Oxide Catalyzed Aerobic Oxidative Coupling of Anilines to Aromatic Azo Compounds'. *Angew. Chem.* **2016**, *128*, 2211.

- **Biswas, S.***; Mosa, I. M.*; El-Sawy, A. M.; Botu, V.; Guild, C.; Song, W.; Ramprasad, R.; Rusling, J. F.; Suib, S. L. 'Tunable Mesoporous Manganese Oxide for High Performance Oxygen Reduction and Evolution Reactions' *J. Mater. Chem. A.* **2016**, *4*, 620.

- Song, W.; Ren, Z.; Chen, S.-Y.; **Biswas, S.**; Nandi, P.; Elsen, H.A.; Gao, P.-X.; Suib, S. L.; 'Ni and Mn-Promoted Mesoporous Co_3O_4: a Stable Bifunctional Catalyst with Surface Structure Dependent Activity for Oxygen Reduction Reaction and Oxygen Evolution Reaction'. *ACS Appl. Mater. Interfaces*. **2016**, *8(32)*, 20802.

- He, J.; Liu, Y.; Meng, Y.; Sun, X.; **Biswas, S.**; Shen, M.; Luo, Z.; Miao, R.; Zhang, L.; Mustain, W. E.; Suib, S. L.; 'High-rate Long-life of Li-ion Batteries Using Reduced Graphene Oxide/Co_3O_4 as Anode Materials'. *RSC Adv*. **2016**, *6*, 24320.

- Chen, S.-Y.; Song, W.; Lin, H.-J.; Wang, S.; **Biswas, S.**; Mollahosseini, M.; Kuo, C.-H.; Gao, P.-X.; Suib, S. L.; 'Manganese Oxide Nano-Array Based Monolithic Catalysts: Tunable Morphology and High Efficiency for CO Oxidation'. *ACS Appl. Mater. Interfaces*. **2016**, *8(12)*, 7834.

- **Biswas, S.**; Dutta, B.; Mullick, K.; Kuo, C.-H.; Poyraz, A. S.; Suib, S. L. 'Aerobic Oxidation of Amines to Imines by Cesium Promoted Mesoporous Manganese Oxide'. *ACS Catal.* **2015**, *5*, 4394.

- **Biswas, S.**; Poyraz, A. S.; Meng, Y.; Kuo, C.-H.; Guild, C.; Tripp, H.; Suib, S. 'Ion Induced Promotion of Activity Enhancement of Mesoporous Manganese Oxides for Aerobic Oxidation Reactions'. *Appl. Catal.,B:Environ.* **2015**, *165*, 731.

- Liu, B.; Kuo, C.-H.; Chen, J.; Luo, Z.; Thannaaru, S.; Li, W.; Song, W.; **Biswas, S.**; Suib, S. L.; He, J. 'Ligand-Assisted Co-Assembly Approach toward Mesoporous Hybrid Catalysts of Transition-Metal Oxides and Noble Metals: Photochemical Water Splitting'. *Angew. Chem. Int. Ed.* **2015**, *127*, 9189.

- Kuo, C.-H.; Mosa, I. M.; Poyraz, A. S.; **Biswas, S.**; El-Sawy, A. M.; Song, W.; Luo, Z.; Chen, S.-Y.; Rusling, J. F.; He, J.; Suib, S. L. 'Robust Mesoporous Manganese Oxide Catalysts for Water Oxidation'. *ACS Catal*. **2015**, *5*, 1693.

- Kuo, C.-H.; Mosa, I. M.; Thannaaru, S.; Sharma, V.; **Biswas, S.**; Aindow, M.; Pamir Alpay, S.; Rusling, J. F.; Suib, S. L.; He, J. 'Facet-Dependent Catalytic Activity of MnO Electrocatalysts for Oxygen Reduction and Oxygen Evolution Reactions'. *Chem. Commun.* **2015**, *51*, 5951.

- Wasalathanthri, N. D.; Poyraz, A. S.; **Biswas, S.**; Meng, Y.; Kuo, C.-H.; Kriz, D. A.; Suib, S. L. 'High-Performance Catalytic CH_4 Oxidation at Low Temperatures: Inverse Micelle Synthesis of Amorphous Mesoporous Manganese Oxides and Mild Transformation to $K_{2-x}Mn_8O_{16}$ and ϵ-MnO_2'. *J. Phys. Chem. C.* **2015**, *119*, 1473.

- Guild, C.; **Biswas, S.**; Meng, Y.; Jafari, T.; Gaffney, A. M; Suib, S. L. 'Perspectives of Spray Pyrolysis for Facile Synthesis of Catalysts and Thin Films: An Introduction and Summary of Recent Directions'. *Catal Today*. **2014**, *238*, 87.

- Poyraz, A. S.; Kuo, C.-H.; **Biswas, S.**; King'ondu, C. K.; Suib, S. L. 'A General Approach to Crystalline and Monomodal Pore Size Mesoporous Materials'. *Nat. Commun*. **2013**, *4*, 2952.

- Poyraz, A. S.; **Biswas, S.**; Genuino, H. C.; Dharmarathna, S.; Kuo, C. H.; Suib, S. L. 'Bimodification of Mesoporous Silicon Oxide by Coupled "In Situ Oxidation at the Interface and Ion Exchange" and its Catalytic Activity in the Gas-Phase Toluene Oxidation'. *ChemCatChem.* **2013**, *5*, 920.

  * Co-first author

2. Book Chapters

- Poyraz, A. S.; **Biswas, S.**; Kim, E.; Meng, Y.; Suib, S. L. (Chapter) 'Mesoporous TM Oxide Materials by Surfactant-Assisted Soft Templating'. Perovskite and mixed oxides / WILEY-VCH. **2016**, ch 31.

- Poyraz, A. S.; **Biswas, S.**; Kim, E.; Meng, Y.; Suib, S. L. (Chapter) 'Mesoporous Multivalent Transition Metal Oxides (V, Cr, Mn, Fe, and Co) in Catalysis'. *Comprehensive Guide for Mesoporous Materials, Volume 3: Properties and Development/ Nova Science Publishers, Inc.*

3. Presentations

- **Biswas, S.** and Suib, S. L. "Aerobic oxidation of organic molecules by heterogeneous mesoporous manganese oxide catalysts". *ACS Meeting,* San Diego, 3/2016.
- **Biswas, S**., Cloud, J. C.; and Suib, S. L. "Porous solid electrolytes for advanced lithium ion batteries". *ACS Meeting,* San Diego, 3/2016.
- **Biswas, S**., Rossi, A. R.; and Suib, S. L. "Cooperative catalysis of Cu and Mn in aerobic oxidative coupling of terminal alkynes". *Pacifichem*, Honolulu, Hawaii, 12/2015 (*Best Poster Award*).
- **Biswas, S.** and Suib, S. L. "Tunable mesoporous manganese oxide as an efficient heterogeneous catalyst for solvent free aerobic oxidation of hydrocarbons". *ACS National Meeting*, Boston, 8/2015 (*Merit Award*).

- **Biswas, S**. and Suib, S. L. “Ion induced activity enhancement of mesoporous manganese oxide in oxidation reactions”. *MRS Fall Meeting and Exhibit*, Boston, 12/2014 (*Best Poster Award*).
- **Biswas, S**. Poyraz, A. S.; and Suib, S. L. A new approach to mesoporous manganese oxide and catalytic applications. *Chemistry Graduate Student Symposium*, University at Buffalo, 5/2014.